

NUMERICAL AND EXPERIMENTAL INVESTIGATION OF
ACOUSTOPHORETIC MICROFLUIDIC DEVICES

A THESIS SUBMITTED TO
THE GRADUATE SCHOOL OF NATURAL AND APPLIED SCIENCES
OF
MIDDLE EAST TECHNICAL UNIVERSITY

BY

MEHMET AKİF ŞAHİN

IN PARTIAL FULFILLMENT OF THE REQUIREMENTS
FOR
THE DEGREE OF MASTER OF SCIENCE
IN
MECHANICAL ENGINEERING

DECEMBER 2020

Approval of the thesis:

**NUMERICAL AND EXPERIMENTAL INVESTIGATION OF
ACOSTOPHORETIC MICROFLUIDIC DEVICES**

submitted by **MEHMET AKİF ŞAHİN** in partial fulfillment of the requirements
for the degree of **Master of Science in Mechanical Engineering, Middle East
Technical University** by,

Prof. Dr. Halil Kalıpçılar
Dean, Graduate School of **Natural and Applied Sciences** _____

Prof. Dr. Mehmet Ali Sahir Arıkan
Head of the Department, **Mechanical Engineering** _____

Assoc. Prof. Dr. Mehmet Bülent Özer
Supervisor, **Mechanical Engineering, METU** _____

Examining Committee Members:

Assoc. Dr. Ergin Tönük
Mechanical Engineering, METU _____

Assoc. Prof. Dr. Mehmet Bülent Özer
Mechanical Engineering, METU _____

Assoc. Prof. Dr. Barbaros Çetin
Mechanical Engineering, Bilkent University _____

Assoc. Dr. Ender Yıldırım
Mechanical Engineering., METU _____

Assoc. Prof. Dr. Yiğit Yazıcıoğlu
Mechanical Engineering, METU _____

Date: 28.12.2020

I hereby declare that all information in this document has been obtained and presented in accordance with academic rules and ethical conduct. I also declare that, as required by these rules and conduct, I have fully cited and referenced all material and results that are not original to this work.

Name, Last name : Mehmet Akif Şahin

Signature :

ABSTRACT

NUMERICAL AND EXPERIMENTAL INVESTIGATION OF ACOUSTOPHORETIC MICROFLUIDIC DEVICES

Şahin, Mehmet Akif
Master of Science, Mechanical Engineering
Supervisor : Assoc.Prof. Dr. Mehmet Bülent Özer

December 2020, 89 pages

Acoustophoresis is one of the techniques to manipulate suspended particles to intended positions in continuous flow. In this study, a numerical simulation methodology that couples electro-mechanic, solid, and acoustic domains in 3D has been developed for acoustofluidic chips. Numerical investigation of design and operation parameters' effects were performed in terms of performance metrics. The simulation model was used for further analysis to understand the effects of manufacturing and assembly errors on acoustophoretic performance. The combined effect of chip dimensions on particle separation was investigated using the Monte Carlo approach. Acoustophoretic chips made of silicon, glass, and acrylic were fabricated and compared in terms of microparticle focusing performance. Even though the acrylic chip is more tolerant to the dimensional and manufacturing variations, silicon and glass based chips were able to focus the microparticles better than the acrylic chip.

Keywords: Acoustophoresis, Particle Manipulation, Numerical Modelling, Monte Carlo, Sensitivity Analysis

ÖZ

AKUSTOFORETİK MİKROAKIŞKAN CİHAZLARIN SAYISAL VE DENEYSEL İNÇLENMESİ

Şahin, Mehmet Akif
Yüksek Lisans, Makina Mühendisliği
Tez Yöneticisi: Doç. Dr. Mehmet Bülent Özer

Aralık 2020, 89 sayfa

Akustoforez, akış içerisinde hedeflenen parçacıkların istenilen pozisyonlara hareket etmesini sağlayan tekniklerden bir tanesidir. Bu çalışmada, 3 boyutta elektromekanik, katı ve akustik bölgelerin birbiriyle bağlantılı çalıştığı sayısal benzetme metodolojisi geliştirilmiştir. Tasarım ve operasyon parametrelerinin etkileri performans metrikleri ile sayısal incelenmesi gerçekleştirildi. Sayısal model daha ileri analizler olan üretim ve montaj hatalarının akustoforetik performansa etkisinin anlaşılması için kullanıldı. Parçacıkların ayırımında yonga geometrik ölçü değişimlerinin birleşmiş etkisi Monte Carlo yaklaşımıyla incelendi. Silisyum, cam ve akrilik malzemelerden akustoforetik yongalar üretildi ve mikroparçacıkları odaklama performansı açısından karşılaştırıldı. Akrilik malzemedен yapılmış yonga boyut ve üretim hatalarını daha iyi tolere etse de silikon ve cam yongalar mikro parçacıkları akrilik yongadan daha iyi odaklamıştır.

Anahtar Kelimeler: Akustoforez, Parçacık Manipülasyonu, Sayısal Modelleme, Monte Carlo, Hassasiyet analizi

To my parents, Hacer and Kemal Şahin

ACKNOWLEDGMENTS

I would like to express my deep appreciation to my supervisor, Assoc. Prof. Dr. Mehmet Bülent Özer, who has the substance of wisdom: he convincingly guided and encouraged me to do the right thing even when the road got tough. Without his continuous support, I would not have enough motivation for completion.

I would like to express my gratitude to Assoc. Prof. Dr. Barbaros Çetin who opened the doors of the BilkentUniversity' facilities and to his students, Atakan Atay and Büşra Sarıarslan, who manufactured silicon chips and helped me in my experiments.

It will not be enough to thank my one and only wife, who always supported me, who was with me in my good and bad moments, who encouraged me and shared *the life*. Without her, not a word of this thesis would have been written.

I wish to thank my parents, my beloved sister, Nimet Selcen, her dear husband Recep, my nephews, Ali and Ömer, and my handsome brother, Ahmet Eren for all kinds of endless support. Without them, I would not have imagined myself walking the academy path.

I would like to express my happiness and peace of sharing the same working environment with Yunus Uslan and having his companionship. To '*der Steppenwolf*' inside us.

I wish to thank my dear friends, Hande Açıkgöz, and Muharrem Akkaya. I never forget the motivations and supports of them. Also, the technical assistance of my dear friend Ömer Çaylan and his students at TOBB University of Economics and Technology for etching the glass is gratefully acknowledged.

This work is partially funded by the Scientific and Technological Research Council of Turkey under grant number TÜBİTAK 115M684. Also, silicon-based chip production, microparticles, and fluorescence microscope imaging are funded by TÜBİTAK 118E023..

TABLE OF CONTENTS

ABSTRACT.....	v
ÖZ.....	vi
ACKNOWLEDGMENTS	viii
TABLE OF CONTENTS.....	ix
LIST OF TABLES	xii
LIST OF FIGURES	xiii
LIST OF ABBREVIATIONS	xvi
LIST OF SYMBOLS	xviii
CHAPTERS	
1 INTRODUCTION	1
1.1 Historical Background	2
1.2 Particle Separation Under Ultrasonic Wave	3
1.3 Literature Review.....	5
2 NUMERICAL MODEL.....	9
2.1 Modeling of the Acoustophoretic chip	10
2.2 Investigated Case Studies	11
2.3 Mathematical Model of Numerical Simulation	14
2.4 Determining the baseline separation scenario.....	21
3 INVESTIGATION OF EFFECT OF DESIGN AND OPERATING PARAMETERS	23
3.1 Performance Metrics	24

3.2	Case Studies for Investigation of Design and Operation Parameters on Acoustophoresis Performance	27
3.2.1	Case 1: Introductory Case, Separation in 1mm channel width.....	29
3.2.2	Case 2: Separation on different channel widths at corresponding frequencies.....	30
3.2.3	Case 3: Separation on different channel widths at the same frequency....	32
3.2.4	Case 4: Separation on different channel heights.....	35
3.2.5	Case 5: Separation at different main/side flow ratios	37
3.2.6	Case 6: Separation of closer size particles.....	38
3.2.7	Case 7: The effect of particle release location and size distribution	40
3.3	Discussion of Results	43
4	UNDERSTANDING THE EFFECTS OF MANUFACTURING AND ASSEMBLY ERRORS ON ACOUSTOPHORETIC PERFORMANCE	45
4.1	Dimensional Variations	49
4.1.1	Monte Carlo Approach on Combined Dimensional Deviations.....	51
4.2	Effect of Assembly Error.....	58
4.3	Variations in the Piezoelectric Actuator Placement	60
4.4	Discussion of Results	63
5	EXPERIMENTAL STUDIES	65
5.1.1	Fabrication of Chips.....	65
5.1.2	Frequency Response Function (FRF) Measurements of the Chips	68
5.1.3	Experimental Procedure.....	69
5.2	Results	72
5.3	Discussion of Results	73
6	CONCLUSIONS	75

REFERENCES	79
------------------	----

LIST OF TABLES

TABLES

Table 2.1 Case Parameters	11
Table 3.1 Simulation parameters.....	28
Table 3.2 Main (Q_A) and Side (Q_B) flow ratios and corresponding voltage value to achieve separation	37
Table 4.1 Parameters geometry, operation conditions, and material properties	48
Table 4.2 Tolerances for geometric dimensions.....	52

LIST OF FIGURES

FIGURES

Figure 1.1 Chaladni Plate and Kundt's tube experiment [29], [30].....	2
Figure 1.2 Half-wave Layered Resonator Type.....	4
Figure 1.3 Transverse Resonator Type	4
Figure 2.1 Flow chart of numerical simulation methodology.....	9
Figure 2.2 Trifurcated inlet and outlet design.....	10
Figure 2.3 The Acoustophoretic chip geometric sections.....	10
Figure 2.4 The Acoustophoretic chip geometry parameters	12
Figure 2.5 The Acoustophoretic chip assembly error parameters	12
Figure 2.6 Actuator placement configurations.....	13
Figure 2.7 Normalized pressures for frequency sweep.....	22
Figure 3.1 Geometric model of the chip and chip parameters	23
Figure 3.2 Separation metric representation examples	26
Figure 3.3 Separation and performance metrics in 1.0 mm channel with 700 kHz resonance: (A) separation of 5 μm and 15 μm particles, (B) purity and yield, (C) % stuck and force, (D) separation metric and residence time	30
Figure 3.4 Performance metrics and separation at different resonance frequencies: (A) Purity and yield, (B) % stuck, (C) average acoustophoretic force, (D) separation metric and residence time, (E) separation of 5 μm and 15 μm particles	32
Figure 3.5 Performance metrics and separation at fixed resonance frequencies: (A) Purity and yield, (B) % stuck, (C) average acoustophoretic force, (D) separation metric and residence time	34
Figure 3.6 Acoustic pressure gradients for channel widths excited at 0.4 MHz.....	35
Figure 3.7 Performance metrics and separation at different channel heights: (A) Purity and yield, (B) % stuck, (C) average acoustophoretic force, (D) separation metric and residence time, (E) separations in heights of 250 μm and 950 μm	36

Figure 3.8 Performance metrics at different main/side flow ratios: (A) Purity and yield, (B) % stuck, (C) average acoustophoretic force, (D) separation metric and residence time	38
Figure 3.9 Performance metrics for closer particles: (A) Purity and yield, (B) % stuck, (C) average acoustophoretic force, (D) separation metric and residence time	39
Figure 3.10 Particle release positions: (A) Baseline, (B) Quarter width, (C) Quarter Depth, (D) Quarter Depth/Width.....	40
Figure 3.11 Performance metrics for similar particles at different focusing configurations: (A) Purity and yield (without size distribution), (B) purity and yield (with size distribution), (C) separation metric and residence time with and without size distribution	42
Figure 3.12 Particle size distributions and release location configurations	43
Figure 4.1 Broadband frequency responses of chips and pressure gradients for peak values.....	46
Figure 4.2 An example of sensitivity study on channel width of the acrylic chip ..	47
Figure 4.3 Effect of channel dimensions on separation	49
Figure 4.4 Effect of chip dimensions on separation	50
Figure 4.5 Effect of PZT dimensions on separation.....	51
Figure 4.6 Glass-Acrylic Hybrid Chip	53
Figure 4.7 Approximation of pi values using randomly generated numbers	54
Figure 4.8 Normal distribution example for acrylic channel width case	55
Figure 4.9 Results according to the number of experiments	56
Figure 4.10 True tolerance results for silicon and glass chips	57
Figure 4.11 Mean acoustic radiation force and sensitivity results for three material	58
Figure 4.12 Lid-Substrate assembly errors.....	59
Figure 4.13 PZT-Substrate assembly errors	60
Figure 4.14 Symmetric assembly configuration of PZT	61
Figure 4.15 Asymmetric assembly configuration of PZT	62

Figure 4.16 Out of phase excitation of two PZTs	63
Figure 5.1 CNC Machining of acrylic chip and assembly parts	65
Figure 5.2 Acrylic mask for wet etching and its application	66
Figure 5.3 Flow of DRIE technique's steps	67
Figure 5.4 Acoustofluidic chips made of silicon, glass, and acrylic.....	67
Figure 5.5 Vibration measurement setup	68
Figure 5.6 Frequency response of three chips	69
Figure 5.7 Experimental setup for particle focusing.....	70
Figure 5.8 Inverted Microscope and fluorescein lights for (A) red and (B) green-dyed particles	71
Figure 5.9 Flow design of focusing experiment (S.P. = Syringe Pump)	71
Figure 5.10 12 μm particle focusing results for three chips	72
Figure 5.11 2 μm particle focusing results for two chips	73

LIST OF ABBREVIATIONS

ABBREVIATIONS

LOC	Lab-on-a-chip
ARF	Acoustic Radiation Force
SAW	Surface Acoustic Wave
BAW	Bulk Acoustic Wave
RBC	Red Blood Cell
PBPC	Peripheral Blood Progenitor Cell
PBMC	Peripheral Blood Mononuclear Cell
CTC	Circulating Tumor Cell
PDMS	Polydimethylsiloxane
PZT	Pb(ZrTi) – Lead Zirconate Titanate
SM	Separation Metric
CNC	Computer Numerical Control
CAD	Computer-Aided Design
CAM	Computer-Aided Manufacturing
UV	Ultraviolet

HF	Hydrofluoric Acid
DRIE	Deep Reactive Ion Etching
FRF	Frequency Response Function
FFT	Fast Fourier Transform

LIST OF SYMBOLS

SYMBOLS

ω	Actuation frequency (Hz)
ρ	Material Density
λ_L	Lame's First Parameter
μ_L	Lame's Second Parameter
ν	Poisson's Ratio
E	Young Modulus
G	Shear Modulus
η_s	Structural Loss Factor
\mathbf{e}	Piezoelectric Coupling Matrices
$\boldsymbol{\varepsilon}$	Dielectric Matrices
$\eta_{\varepsilon s}$	Dielectric Loss Factor
η	Viscosity
β	Viscosity Ratio
c_a	Speed of Sound in Liquid
k	Wavenumber

γ	Viscous Damping
δ	Viscous Boundary Layer
a	Particle Diameter
λ	Acoustic Wavelength
ρ_p	Particle Density
c_p	Speed of Sound in Particle
m_p	Particle Mass

CHAPTER 1

INTRODUCTION

Development in science and technology starts with a problem definition, continues to pursue a solution, and aims to discover the new creative enhancements on the existing solutions. Similar improvements are aimed for problems related to medicine and health using science and engineering principles. For example, the need for simple and fast applications of diagnosis and treatment of illnesses requires automated, cheap, and accurate solutions. Lab-on-a-chip (LOC) is a term used for the devices that can integrate multiple laboratory tests, plastic/silicon chip which can have dimensions ranging from micrometers to millimeters. They have a promising future to take the place of large, expensive, complicated testing equipment used in the fields of biology and medicine.

Ultrasonic sound wave applications in biomedical research are rapidly increasing in the past years, especially after implementing the ultrasonic effects into the lab-on-a-chip systems[1]–[4]. Acoustophoresis is one of the phenomena used in different lab-on-a-chip systems. The ability to manipulate suspended particles or cells under the effect of acoustic radiation force (ARF) creates a new viewpoint for laboratory devices (i.e., cytometer, centrifuge, cell washer, cell trapper, automated cell culture). Acoustophoresis may lead to the possibility of inexpensive, label-free, biocompatible, and ease-to-use devices[5]–[18]. In literature, different kinds of ultrasonic manipulation have been successfully implemented, i.e., focusing/enrichment/washing, size-based separation, medium density-based separation, particle trapping, and patterning[2], [11], [14], [19]–[28].

1.1 Historical Background

Several historical figures were interested in the vibration/acoustic topics from the Greek philosophers Pythagoras (6th century BC) and Aristotle (4th century BC) to fathers of acoustics, Hermann von Helmholtz (1821-1894) and Lord Rayleigh (1842-1919). However, the history of the moving particle under the vibration and sound wave's effect could extend to Chladni's works. Ernst Chladni (1756-1827) was a physicist, musician, and musical instrument maker who invented the Chladni plates to visualize the intricate pattern of a standing wave. Later, August Kundt (1839-1894) create a setup to measure the speed of sound in a medium. The setup consists of a tube with a vibration source at one side, an adjustable lid for tube length arrangement at the other side, and sprinkled powder inside. When the tube length is arranged to the multiples of the medium's wavelength and vibrated at a known frequency at one side, sprinkled powders tend to move through the zero-displacement point, called a nodal point. Acoustofluidic particle manipulation is quite similar to Kundt's tube in terms of the working principle. Figure 1.1 shows the Chladni Plate and Kundt's tube experiments.

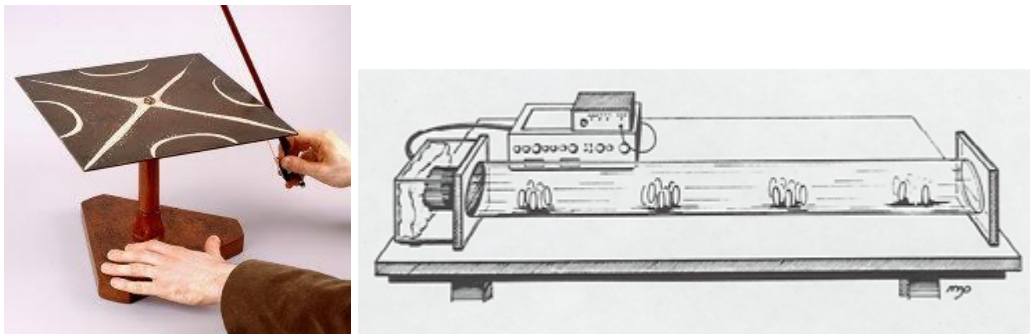


Figure 1.1 Chaladni Plate and Kundt's tube experiment [29], [30]

The first attempt to derive an analytical formulation of acoustic radiation force was made by King (1934) [31]. The results that he found from analytical relations, for the case of hard materials (such as metal spheres), are in good agreement with the experiments. However, King noted that the formula could extend to refine the acoustic pressures, including compressible sphere and viscous medium; after that, Yosioka and Kawasima (1955) [32] published the derivation of ARF on a

compressible sphere and reported matching results of experiments on bubbles [33]. Settner and Bruss (2012) recently calculated the ARF on compressible, spherical particles suspended in a viscous medium [34].

1.2 Particle Separation Under Ultrasonic Wave

Acoustic wave in a medium creates acoustic pressure, consisting of node and anti-node points along the propagation direction. Any solid particles under acoustic pressure tend to move the nearest node point, called a zero-displacement point, as the same phenomena occurred in Kundt's tube experiment. Combination of acoustics and microfluidics in order to manipulate particles accomplished in two primary design types, surface acoustic wave (SAW) [35]–[37] resonator and bulk acoustic wave resonator (BAW) [38]–[40]. Even though the SAW resonator has better selectivity and low power application, they could not reach high flow rates limiting them in real-life applications. On the other hand, BAW resonators were shown to achieve that reached more than one mL/min flow rate in red blood cells (RBCs) focusing [8], [41].

There are also two different designs for BAW resonators, which differentiate from each other by standing wave direction. Longitudinal waves are used in layered resonators in which the channel width can arrange for quarter/half/multiple wavelengths according to different separation purposes. Materials with a high acoustic impedance are used as a reflector at the opposite wall of the actuation side to create a standing wave in the medium, as shown in Figure 1.2.

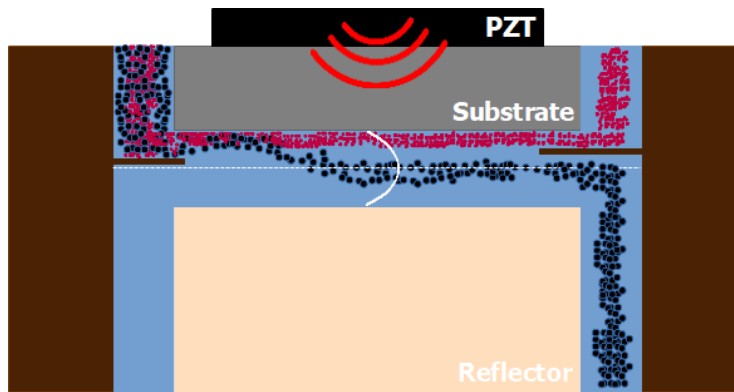


Figure 1.2 Half-wave Layered Resonator Type

However, transverse BAW resonators are based on the shear waves (orthogonal to the actuation direction), which vibrate the microchannel sidewalls when the actuator is placed at the top or bottom of the chip. When walls of the microchannel vibrate out-of-phase, standing waves occur inside. Mostly microchannel of layered resonators is adjusted according to fit half-wave inside the medium and has a trifurcated inlet and outlet design to push particle suspension towards the sidewall near the inlet and to separate targeted particles at the outlet, as shown in Figure 1.3.

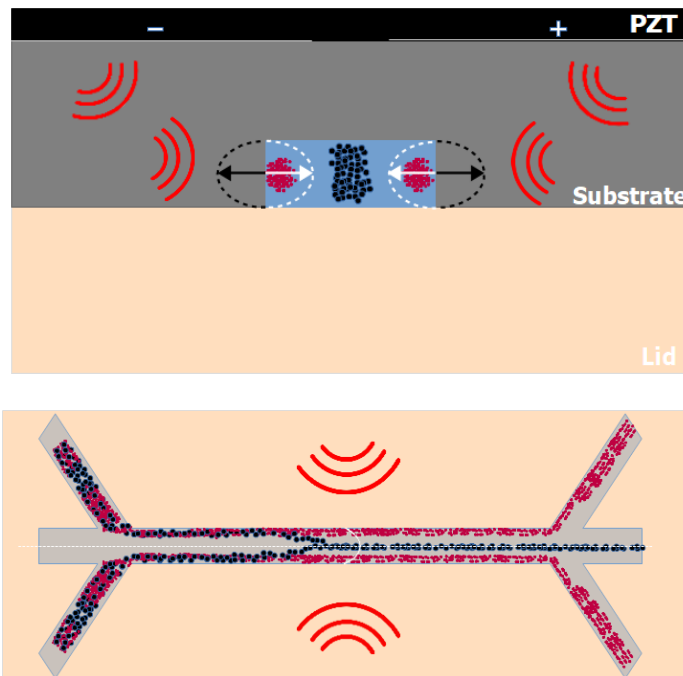


Figure 1.3 Transverse Resonator Type

1.3 Literature Review

Initial applications of ultrasonic particle manipulations started with Dyson et al.'s proposal [42] and which was later realized in Baker's work [43] in 1971 and 1972, respectively. Dyson et al. stated that RBCs in chick embryo's vein aggregated under the ultrasound, and the blood stopped to flow caused by primarily Bernoulli forces between the cells. Then, Baker refuted the explanation by showing that RBCs' sedimentation time was decreased with decreasing the RBC density. If Bernoulli forces were responsible for the aggregation, the sedimentation time would be increased when the RBCs density was reduced.

Other initial studies of acoustophoresis in biomedical and chemical engineering applications have started with layered/multi-layered resonator bioreactors washing the yeast cells from the fluorescein buffer[2], experimentally separating a mixture of different sized particles from the buffer on the trifurcated outlet design, the theoretical background of acoustic contrast factor-based separation[39], and focusing 5 μm latex particles [44]. Later, the layered resonator technique was recently used to improve the throughput of acoustophoretic devices [8], [41], and water quality analysis[45]. Nilsson et al. suggested etched silicon chips design[3] used the piezoelectric transducer as a transversal resonator. Possessing a high speed of sound and acoustic impedance values make the silicon chips more popular in acoustophoresis literature. Recent studies prove the popularity of silicon chip, including removing lipid cells from the shed blood during cardiac surgeries[46], separating different-sized particles from each other, acoustic contrast factor-based separation, isolating CD4+, CD8+ lymphocytes from peripheral blood progenitor cells (PBPC), and separation of blood proteins and platelets[5], [23], [47], [48], diagnosis of prostate-specific antigen with acoustic whole blood plasmapheresis chip[49], [50], quality control of raw milk with protein and lipid content[10], label-free separation viable and non-viable mammalian cells[51], prostate cancer cell, breast cancer cell or different kind of circulating tumor cells (CTCs) enrichment from peripheral blood mononuclear cells (PBMC) or PBPC[13], [15], [28], [52],

harvesting of microalgae[20], sensitive low-concentration oil detection and trapping[26], screening ssDNA aptamer[7], bacteria separation for sepsis diagnosis[53]. Besides the popularity of acoustophoresis devices made from silicon, plastic-based microfluidic devices started to be used as an alternative to the acoustophoretic device with silicon chips[54]. Fiering et al. showed that their plastic chip could achieve to separate lymphocytes from the plasma and rapid detection of bacteria[11], [17], [55], and Çetin et al. [19] designed a polydimethylsiloxane(PDMS)-based chip to integrate the acoustophoresis and the dielectrophoresis. Moreover, glass is also used as a chip material to produce the acoustophoretic device, and researchers showed that glass material has certain benefits in separation and focusing of suspended particles[56], [57].

Although there are several critical applications of acoustophoresis in particle manipulation problems, almost all of these applications are experiments with laboratory prototypes, and there are no mass-produced acoustophoretic devices on the market, except the 2020 Attune NxT Flow Cytometer (Thermo Fischer), which is using the acoustic assisted hydrodynamic focusing. The main reasons for being stuck at the lab prototype level are expensive chip material for silicon-based chips and stable device production problems. The production of stable devices requires each single-use acoustophoretic chips to be manufactured with time-independent constant resonant frequency/impedance values that enable the device to work with the electrical hardware coherently, and devices should be tolerant to the manufacturer deviations in geometry and assembly errors.

Both the polymer and the glass are either suitable to mold or easy to machine and does not require the cleanroom laboratories. Therefore, the high manufacturing cost of the silicon-based chip, which requires a cleanroom environment for etching of the microchannel, shifts the center of interest for the acoustophoretic device material to the glass-made or polymer-based chips[54], [56]. If the acoustophoretic systems are mass-produced, chips should be made of polymer or glass material where molding and machining can be easily used; preferably, no manufacturing process should require a cleanroom environment for production. Manufacturing processes generally

consist of raw material machining or molding of the system's components and ending with the assembly of these components. If the acoustophoretic systems are to be mass-produced, chips should be tolerant to the variations of the materials provided by suppliers; machining, or molding tolerances of the components, and their assembly errors.

The stable device problem in mass production includes optimizing design parameters, determining the optimal working conditions of acoustophoretic systems, and understanding its sensitivities toward manufacturing and assembly tolerances. Optimization of design parameters, i.e., dimensions of a chip, lid, microchannel, and piezoelectric material, fluid flow properties, assembly configurations, need to be considered initially with numerical or analytical methods because large sets of parametric experimental studies are expensive and time-consuming. Many researchers focused on the numerical methods to identify acoustophoretic chip system; some studies interested in the motion of the particle under the acoustic radiation force[58], acoustic streaming effects in a microchannel[59], and also thermoviscous effect in acoustic streaming[60], modeling microparticle population separation with statistical dynamics[61], or maximization of separation with optimized launch position[62]. Besides, performance studies on different lid material of silicon-based chips[63] and investigation of all-polymer acoustofluidics devices [64] are reported in 2D numerical simulations. Furthermore, J.Dual et al. [4], [65] modeled and characterized the chips in terms of acoustic pressure and developed the first numerical genetic algorithm to optimize the acoustofluidics device parameters in 1D & 3D. Performed studies lack at least one of the modeling parameters, such as using a solid domain (for the chip material), piezoelectric transducer domain, fluid flow, 3D, and the particle tracing calculations. Büyükkoçak et al. [66] reported that the first numerical analysis of particle manipulation under the ultrasonic effect, which has all sections mentioned, and the results of the study compared with the experimental studies in the literature. Recently, Şahin et al. [67] investigated the acoustophoretic chip parameters for particle separation with 3D level simulations

and developed performance metrics to evaluate different chip configurations, which is one of the chapters of this thesis.

On the other hand, to identify the chips' optimal working conditions, some researchers suggested to use of the electrical impedance/admittance measurements and calculations[22], [27], [44], [63], [68]; however, there are papers that concluded the electrical impedance measurement would not give an apparent result, especially in complicated systems[69], [70]. Later, Vitali et al. [71] showed that the differential impedance analysis of different liquid-filled chips could give the best optimal working frequency, and they conducted experiments on chips with different materials and configurations. Although different alternatives for measuring resonant frequencies in the literature[69], the easiest and cheapest way to get the information on the working frequency range is to measure the electrical properties of the acoustophoretic device.

In this thesis, it is aimed to:

- Perform a numerical study to understand the parameter which affects the acoustophoretic separation process such as channel width and height, having similar particle diameters, different flow rate ratios at the device inlets and release locations of particles (Chapter 3)
- Identify geometry, assembly, and working condition sensitivities of different materials (Chapter 4)
- Predict a sensitivity to the combined manufacturing errors using a Monte Carlo approach (Chapter 4)
- Experimentally comparing different material chips in terms of their performance for focusing particles to the center of a microchannel in (Chapter 5)

CHAPTER 2

NUMERICAL MODEL

A numerical simulation model that includes multiphysics domains is explained in this part of the thesis. Electro-mechanic equations, elastodynamic equations, and the Helmholtz equation are coupled for simulations. Once pressures and flow field calculations are obtained, particle trajectories are determined. A simple flow chart demonstrates the flow of the numerical simulation.

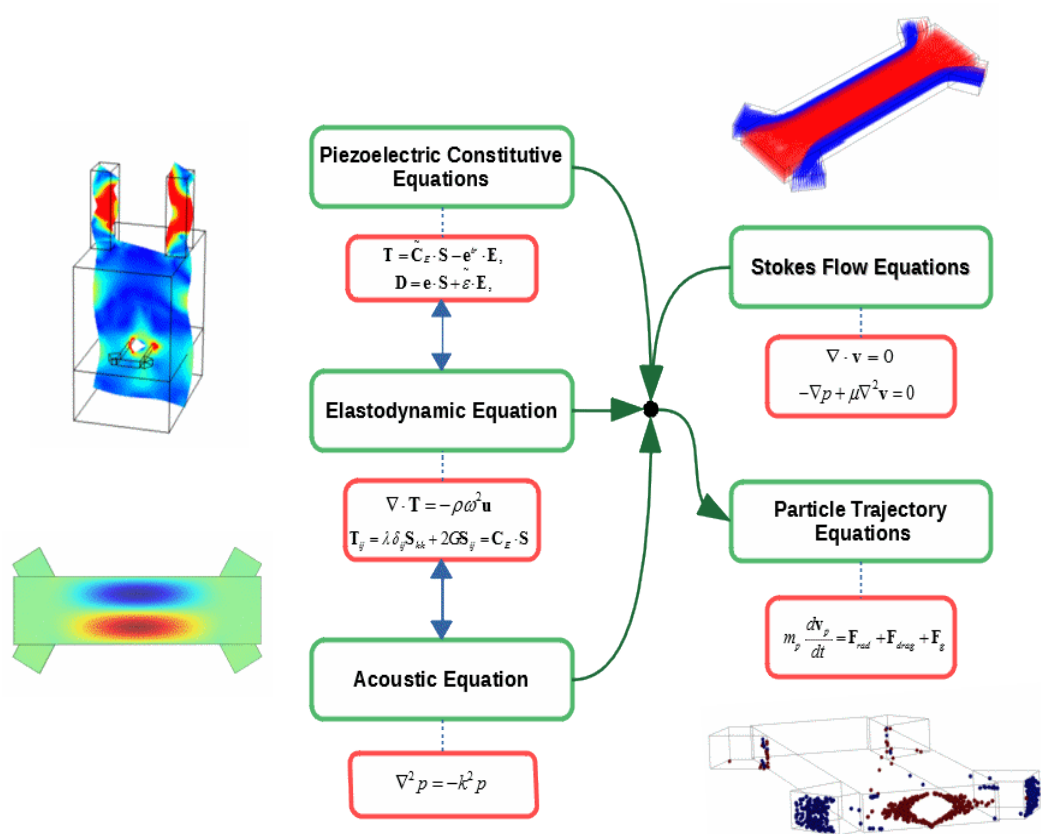


Figure 2.1 Flow chart of numerical simulation methodology

2.1 Modeling of the Acoustophoretic chip

The acoustophoretic chip analyzed in this study is a transversal resonator type that consists of four different subdomains, which are analyzed as solid mechanics, pressure-acoustics, fluid flow, and piezoelectric material domains. Piezoelectric material actuation generates a transversal displacement on the channel sidewalls; thus, the out-of-phase motion of the sidewalls creates a pressure field such that the pressure node is at the center while the antinodes are along the sidewalls of the channel width.

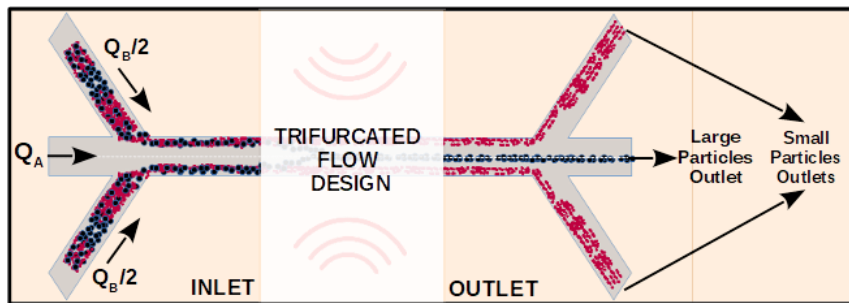


Figure 2.2 Trifurcated inlet and outlet design

Trifurcated inlet and outlet design, as shown in Figure 2.2, operate the buffer and particle suspension to push particles towards channel walls and separate them at the outlet. A glass lid restrains the microchannel at the bottom for any leakages. The assembled microchip and separated geometric sections are shown in Figure 2.3.

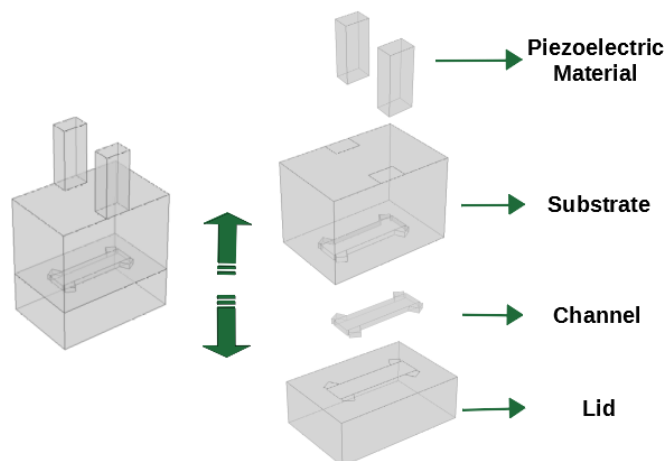


Figure 2.3 The Acoustophoretic chip geometric sections

2.2 Investigated Case Studies

Numerical studies of this thesis consist of seven different cases, which will be examined for the separation performance, the sensitivity of design/assembly errors, and actuation type. Additionally, the Monte Carlo strategy is employed in order to identify which geometric dimension is more sensitive to the real-life manufacturing tolerances.

Seven cases were designed to evaluate the effect of channel width/height, consistency between actuation frequency and channel width, main/side stream flow rate ratio, particle size difference, particles' release location on separation performance as shown in Table 2.1 with detailed information.

Table 2.1 Case Parameters

Case 1 (Baseline)	Particle Diameters = 5 & 15 μm ; Channel Width = 1mm; Actuation Frequency = $\sim 700\text{kHz}$, $Q_{A/B} = 3$ (Flow rate ratio, Total: 80 $\mu\text{L}/\text{min}$)
Case 2	330 μm - 2MHz; 660 μm - 1Mhz; 1000 μm - 700kHz; 1650 μm - 400kHz
Case 3	330 μm - 400 kHz; 660 μm - 400 kHz; 1000 μm - 400 kHz; 1650 μm - 4 00 kHz
Case 4	Channel Height = 50, 150, 250, 500, 750, 950 μm
Case 5	$Q_{A/B} = 1, 2, 3, 5, 10$
Case 6	Particle Diameters = 5 & 8 μm
Case 7	Particle Release Positions: Quarter Width/Full Depth; Full Width/Quarter Depth; Quarter Width/Quarter Depth

Another objective of this study is to determine the sensitivities of the geometric parameters of the chip components shown in Figure 2.4 that are the piezoelectric actuator (such as Pb(ZrTi) – Lead Zirconate Titanate, PZT), substrate hosting the microchannel, microchannel itself, and the glass lid. Variations (5-10%) are applied

to each geometric parameter respectively, and then the average acoustic radiation force acting on each particle is plotted to demonstrate the sensitivity of the parameter to variations.

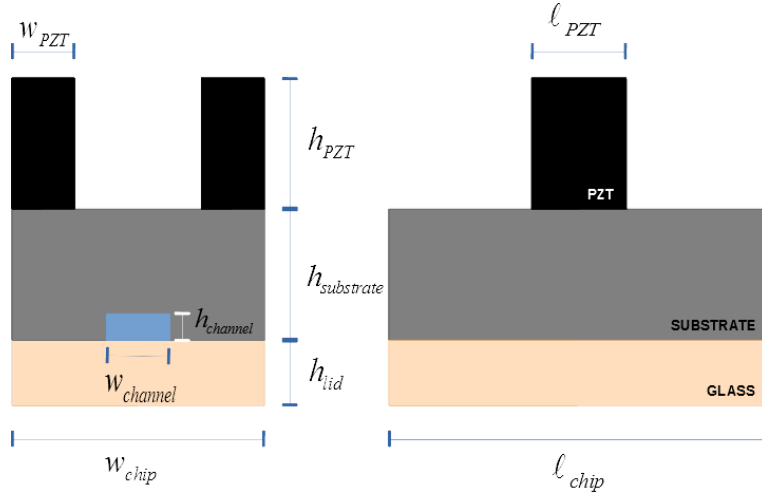


Figure 2.4 The Acoustophoretic chip geometry parameters

Positioning, aligning the PZTs, and bonding the glass lid to the substrate are the required assembly processes that have the possibility of causing misalignment and positioning errors. Possible assembly errors are shown in Figure 2.5, and the sensitivities of the assembly errors on the separation of microparticles are analyzed numerically.

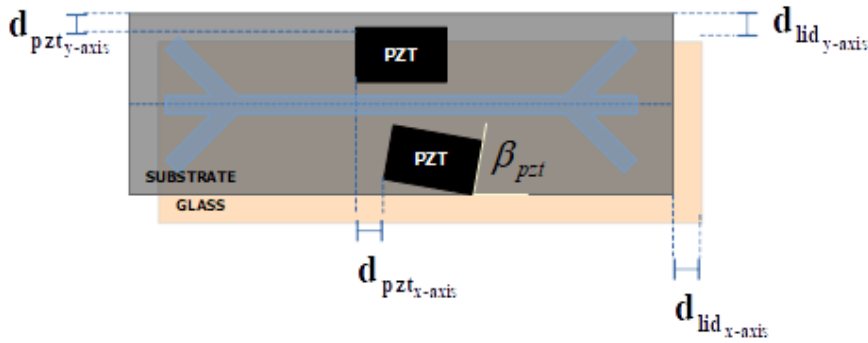


Figure 2.5 The Acoustophoretic chip assembly error parameters

Almost always, piezoelectric materials are used to actuate the acoustofluidics chips in literature [1], [35], [57]. Even though most of the studies in literature use asymmetrically placed the PZT actuator at the bottom of the chip, Çetin B. et al. preferred two different piezo bonded on sidewalls to ensure the two wall vibrations

are out of phase [19]. Gautam G.P. et al. bonded a PZT actuator on one side of the chip in parallel to the microchannel after experimenting with the different placements, such as bonding on the bottom and top surface symmetrically [72]. Therefore, three different placements in Figure 2.6, including symmetrically placed PZT (left), asymmetrically placed PZT (middle), and opposite phase actuation of two separate PZTs (right), are run in the numerical model to identify their ability to manipulate particles.

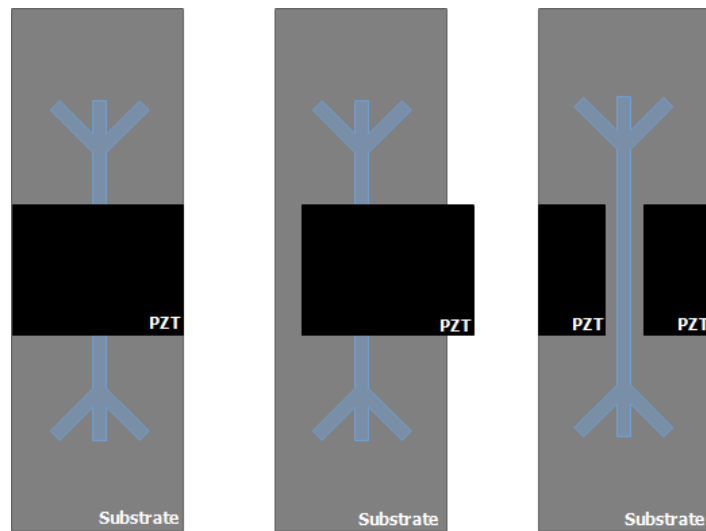


Figure 2.6 Actuator placement configurations

In the physics of acoustofluidics, wavelengths in chip/lid material, fluid, or actuator may vary from hundreds of micrometers to nearly ten millimeters. Though high precision equipment can be used to manufacture components of chips, the cumulative impact of all geometric dimensions' manufacturing error can affect the chip's ability to manipulate the particle to the desired location. The Monte Carlo approach is used to investigate the combined effect of these geometric errors on a chip's performance using real-life variations that may occur during manufacturing and assembly.

2.3 Mathematical Model of Numerical Simulation

The acoustofluidic systems have a substrate on which the microchannel is etched, a glass lid to cover the open side of the microchannel, and one/two different PZT actuators for the generation of acoustic waves. The nature of the system requires solving elastodynamic equations for solid parts, which are substrate, glass, and PZT actuators, together with the electromechanical coupling at the PZT actuators and coupling interfaces between solid and fluid domain. The dynamic equilibrium of the stress field and displacement field in the solid can be written in general form and reduced form for harmonic motion, respectively as

$$\mathbf{u}(\mathbf{x}, t) = \mathbf{u}(\mathbf{x})e^{-j\omega t}, \quad (2.1a)$$

$$\nabla \cdot \mathbf{T} + \mathbf{F} = \rho \frac{\partial^2 \mathbf{u}}{\partial t^2}, \quad (2.1b)$$

$$\nabla \cdot \mathbf{T} = -\rho\omega^2 \mathbf{u}, \quad (2.1c)$$

where \mathbf{T} is denoted as stress field and ρ is the material density. Hooke's law defines the relationship between stress and strain as

$$\mathbf{T}_{ij} = -\lambda_L \delta_{ij} \mathbf{S}_{kk} + 2\mu_L \mathbf{S}_{ij} = \mathbf{C}_E \cdot \mathbf{S}, \quad (2.2)$$

where \mathbf{S} is the strain field, λ_L and μ_L are the Lamé's first and second parameters, respectively, \mathbf{C}_E is the elasticity matrix. Lamé's parameters are a function of Poisson's ratio and Young's modulus as

$$\lambda_L = \frac{E\nu}{(1+\nu)(1-2\nu)}, \quad \mu_L = G = \frac{E}{2(1+\nu)}, \quad (2.3)$$

where E is Young's modulus, ν is Poisson's ratio, and G is the shear modulus. The relationship between the strain and displacement fields reads as

$$\mathbf{S} = \frac{1}{2} [(\nabla \mathbf{u})^T + \nabla \mathbf{u}]. \quad (2.4)$$

Piezoelectric materials generate an electric field when they are under a stress field, and it can also happen in the reverse direction. Electromechanical coupling, which relates the stress and electric fields, should be modeled for the PZT actuator. Constitutive relations of piezoelectric materials can be defined as

$$\mathbf{T} = [\mathbf{C}_E(1 - j\eta_s)] \cdot \mathbf{S} - \mathbf{e}^T \cdot \mathbf{E}, \quad (2.5)$$

$$\mathbf{D} = \mathbf{e} \cdot \mathbf{S} + [\boldsymbol{\varepsilon}(1 - j\eta_{\varepsilon S})] \cdot \mathbf{E}, \quad (2.6)$$

where η_s is the isotropic structural loss coefficient, \mathbf{e} is the piezoelectric coupling matrix, \mathbf{E} is the electric field, \mathbf{D} is the electric displacement field, $\boldsymbol{\varepsilon}$ is the dielectric matrix, and $\eta_{\varepsilon S}$ is the dielectric loss factor.

Calculations for the solid domain determine the displacement or the velocity vectors on the microchannel wall. Indeed, the acoustofluidics formulation is based on the calculation of the pressures inside the fluid and the calculation of the acoustic radiation force acting on a particle inside the fluid. The derivation begins with stating the set of three equations (2.7) for fluid, which are pressure stated as a function of density, continuity equation in fluid dynamics and Navier-Stokes equation,

$$p = p(\rho), \quad (2.7a)$$

$$\partial_t \rho = -\nabla \cdot (\rho \mathbf{v}), \quad (2.7b)$$

$$\rho \partial_t \mathbf{v} = -\nabla p - \rho(\mathbf{v} \cdot \nabla) \mathbf{v} + \eta \nabla^2 \mathbf{v} + \beta \eta \nabla(\nabla \cdot \mathbf{v}), \quad (2.7c)$$

where p , ρ and \mathbf{v} are pressure, density, and velocity fields of the fluid, respectively, η is the viscosity and β is the viscosity ratio. The solution of the set of equations

(2.7) is excessively intricate to attain analytically. Nevertheless, perturbation theory can be used on them. Fields defined for the fluid may extend together with tiny perturbations,

$$\rho = \rho_0 + \rho_1 + \dots + \rho_i, \quad (2.8a)$$

$$p = p_0 + p_1 + \dots + p_i, \quad (2.8b)$$

$$\mathbf{v} = \mathbf{v}_0 + \mathbf{v}_1 + \dots + \mathbf{v}_i, \quad (2.8c)$$

where i denotes the order of the perturbation, and zeroth indices of any variable express the constant value of that variable. So, the first-order perturbation can be written as

$$\rho = \rho_0 + \rho_1, \quad (2.9a)$$

$$p = p_0 + p_1 = p_0 + c_a^2 \rho_1, \quad (2.9b)$$

$$\mathbf{v} = \mathbf{v}_0 + \mathbf{v}_1 = \mathbf{v}_1. \quad (2.9c)$$

In acoustofluidic applications, the constant velocity \mathbf{v}_0 is generally much lower than 0.1 m/s, and it can be neglecting when summing with the higher value \mathbf{v}_1 . Moreover, c_a is the speed of sound in the liquid and equality $p_1 = c_a^2 \rho_1$ can be easily found in the literature as the regular derivation of the speed of sound. Placing the first-order expansion of state variables into the set of equations (2.7) and neglecting the products of the first-order terms results in,

$$\partial_t \rho_1 = -\rho_0 \nabla \cdot \mathbf{v}_1, \quad (2.10a)$$

$$\rho_0 \partial_t \mathbf{v}_1 = -c_a^2 \nabla \rho_1 + \eta \nabla^2 \mathbf{v}_1 + \beta \eta \nabla (\nabla \cdot \mathbf{v}_1). \quad (2.10b)$$

Combining equations (2.10a) and (2.10b) is achieved by taking the gradient of the (2.10b) and inserting it into the time derivative of (2.10a). Application steps are shown below,

$$\partial_t^2 \rho_1 = -\rho_0 \nabla \cdot (\partial_t \mathbf{v}_1),$$

$$\rho_0 \nabla \cdot (\partial_t \mathbf{v}_1) = -c_a^2 \nabla^2 \rho_1 + \eta \nabla^2 (\nabla \cdot \mathbf{v}_1) + \beta \eta \nabla^2 (\nabla \cdot \mathbf{v}_1),$$

↓

$$\partial_t^2 \rho_1 = c_a^2 \nabla^2 \rho_1 - (1 + \beta) \eta \nabla^2 (\nabla \cdot \mathbf{v}_1) \quad \leftrightarrow \quad \nabla \cdot \mathbf{v}_1 = -\frac{1}{\rho_0} \partial_t \rho_1,$$

↓

$$\partial_t^2 \rho_1 = c_a^2 \left[1 + \frac{(1 + \beta) \eta}{\rho_0 c_a^2} \partial_t \right] \nabla^2 \rho_1. \quad (2.11)$$

Now, state variables can be introduced as in time-harmonic fields. A solution for a second-order partial differential equation like (2.11) may hold time-harmonic fields for their state variable, which makes it easier to process. Time-harmonic fields at a frequency of ω can be written as,

$$\mathbf{v}_1(\mathbf{x}, t) = \mathbf{v}_1(\mathbf{x}) e^{-j\omega t}, \quad \rho_1(\mathbf{x}, t) = \rho_1(\mathbf{x}) e^{-j\omega t},$$

$$p_1(\mathbf{x}, t) = p_1(\mathbf{x}) e^{-j\omega t} = c_f^2 \rho_1(\mathbf{x}) e^{-j\omega t}. \quad (2.12)$$

Therefore, rewriting equation (2.11) together with the time-harmonic fields in (2.12) results in Helmholtz Equation for acoustic wave as,

$$\nabla^2 p_1 = -k^2 p_1, \quad (2.13)$$

where p_1 is the first-order pressure field and k is the wavenumber, which can be defined as the number of cycles per unit distance. The formulation of the wavenumber is as

$$k = (1 + j\gamma) \frac{\omega}{c_a}, \quad \gamma = \frac{(1 + \beta)\eta\omega}{2\rho_0 c_a^2}. \quad (2.14)$$

Even though the wavenumber is complex-valued because of the viscous damping, γ is very small, 10^{-6} , for water which is at room temperature together with a frequency in the order of MHz, and it can be neglected. Furthermore, under inviscid and harmonic fields assumptions, $\eta = 0$ and $(\partial_t[*]e^{-i\omega t}) = -i\omega[*]e^{-i\omega t}$, the equation (2.10b) gives the first-order velocity fields as a function of the first-order pressure/density,

$$\mathbf{v}_1 = \frac{c_a^2}{i\omega\rho_0} \nabla p_1 = \frac{1}{i\omega\rho_0} \nabla p_1 = \nabla \phi_1, \quad (2.15)$$

where ϕ_1 is the acoustic velocity potential. The first order fields can be determined by solving (2.13) and (2.15) according to the boundary conditions. Therefore, the second-order perturbed fields may be placed into the equation set of (2.7) in order to calculate second-order effects of pressure p_2 and velocity \mathbf{v}_2 , which p_2 is highly responsible for acoustic radiation force and \mathbf{v}_2 is also known as acoustic streaming. A way of determining acoustic radiation force is not averaging any time scales corresponding to MHz applications; however, it can be calculated with time averaging over a full oscillation period. Time-average is denoted as $\langle X \rangle$ and read as

$$\langle X \rangle = \frac{1}{\tau} \int_0^\tau dt X(t). \quad (2.16)$$

Time-averaged notation gives a consequence that any harmonic motion does not contribute to second-order effect due to $\langle \cos(\omega t) \rangle = 0$; however, the products of the first-order terms have $\cos^2(\omega t)$, which is non-zero under time averaging. Neglecting the product of second-order terms, the product of more than two perturbed terms; continuity and Navier-Stokes equations in (2.7) can be written as

$$\partial_t \rho_2 = -\rho_0 \nabla \cdot \mathbf{v}_2 - \rho_1 \nabla \cdot \mathbf{v}_1, \quad (2.17a)$$

$$\rho_0 \partial_t \mathbf{v}_2 = \nabla p_2 + \eta \nabla^2 \mathbf{v}_2 + \beta \eta \nabla (\nabla \cdot \mathbf{v}_2) - \rho_1 \partial_t \mathbf{v}_1 - \rho_0 (\mathbf{v}_1 \cdot \nabla) \mathbf{v}_1. \quad (2.17b)$$

Assuming harmonic dependence of second-order perturbation terms, the time average of (2.17) becomes

$$\rho_0 \nabla \cdot \langle \mathbf{v}_2 \rangle = -\rho_1 \nabla \cdot \langle \mathbf{v}_1 \rangle, \quad (2.18a)$$

$$\nabla \langle p_2 \rangle = \eta \nabla^2 \langle \mathbf{v}_2 \rangle + \beta \eta \nabla (\nabla \cdot \langle \mathbf{v}_2 \rangle) - \langle \rho_1 \partial_t \mathbf{v}_1 \rangle - \rho_0 \langle (\mathbf{v}_1 \cdot \nabla) \mathbf{v}_1 \rangle, \quad (2.18b)$$

$$\nabla \langle p_2 \rangle = -\langle \rho_1 \partial_t \mathbf{v}_1 \rangle - \rho_0 \langle (\mathbf{v}_1 \cdot \nabla) \mathbf{v}_1 \rangle, \quad \text{for inviscid flow } (\eta=0). \quad (2.18c)$$

Furthermore, time-averaged second-order pressure term may become alone at the left-hand side with the use of first-order inviscid Navier Stokes equation

$\rho_0 \partial_t \mathbf{v}_1 = -c_a^2 \nabla \rho_1$ and $\langle (\mathbf{v}_1 \cdot \nabla) \mathbf{v}_1 \rangle = \frac{1}{2} \nabla \cdot \langle \mathbf{v}_1^2 \rangle$. Thus, p_2 can be written as a function of p_1 and \mathbf{v}_1 ,

$$\langle p_2 \rangle = \frac{1}{2\rho_0 c_a^2} \langle p_1^2 \rangle - \rho_0 \frac{1}{2} \langle \mathbf{v}_1^2 \rangle. \quad (2.19)$$

Therefore, the acoustic radiation force, \mathbf{F}^{rad} , can be defined for a fixed surface enclosing the particle, S_0 , as a surface integral of time-averaged second-order pressure and momentum flux tensor $\rho_0 \langle \mathbf{v}_1 \mathbf{v}_1 \rangle$,

$$\mathbf{F}^{\text{rad}} = -\int_{S_0} da \left\{ \langle p_2 \rangle \mathbf{n} + \rho_0 \langle (\mathbf{n} \cdot \mathbf{v}_1) \mathbf{v}_1 \rangle \right\}. \quad (2.20)$$

Equation (2.20) is a general form of \mathbf{F}^{rad} . However, in this thesis, we are interested in an inviscid flow, which applicable when the viscous boundary layer, $\delta = \sqrt{2\eta / \rho_0 \omega}$, is much smaller than the particle diameter, a [73]. While considering the size of the particle and channel that is used and flow rates applied, second-order effect acoustic streaming created by an acoustic wave is not included to prevent high computational load. Thus, if particle sizes are small compared to the microchannel dimension; then, particle-particle and particle-channel wall interactions can be ignored as mentioned in the literature [74]. Acoustic radiation force can be treated by first-order scattering theory when acoustic wavelength, λ , is much larger than the particle size, $a \ll \lambda$. Inserting (2.19) into (2.20), \mathbf{F}^{rad} yields a function based on the first-order terms,

$$\mathbf{F}^{\text{rad}} = -\int_{S_0} da \left\{ \left[\frac{1}{2\rho_0 c_a^2} \langle p_1^2 \rangle - \rho_0 \frac{1}{2} \langle \mathbf{v}_1^2 \rangle \right] \mathbf{n} + \rho_0 \langle (\mathbf{n} \cdot \mathbf{v}_1) \mathbf{v}_1 \rangle \right\}. \quad (2.21)$$

The first-order fields consist of two components, which are incident and scattered field components according to the sufficiently weak scattered wave assumption, $a \ll \lambda$. Thus, the first-order fields can be written as the sum of these components. However, in this thesis, details of scattering theory and detailed derivation of acoustic radiation force will not be given. For further reading, the references are appropriate [40], [73]–[79]. In conclusion, manipulations on equation (2.20) result in a generalized form by Gorkov [80]

$$\mathbf{F}^{\text{rad}} = -\nabla U_{\text{rad}}, \quad (2.22)$$

$$U_{rad} = \frac{4\pi}{3} a^3 \left[f_1 \frac{1}{2\rho_0 c_a^2} \langle p_{in}^2 \rangle - f_2 \frac{3}{4} \rho_0 \langle \mathbf{v}_{in}^2 \rangle \right],$$

$$f_1 = 1 - \frac{\rho_0 c_a^2}{\rho_p c_p^2}, \quad f_2 = \frac{2(\rho_p - \rho_0)}{2\rho_p + \rho_0},$$

where U_{rad} is radiation potential, p_{in} and \mathbf{v}_{in} are the incident component of the first-order term, f_1 and f_2 are monopole and dipole coefficients and ρ_p , c_p are particle density and speed of sound, respectively. In this thesis, particles are polystyrene particles that have relative density value to the water, which means that the viscous correction is not needed, as stated in the literature[34]. Once the acoustic radiation force calculated from the pressure and velocity fields by the solution of Helmholtz equation on coupled modules in COMSOL Multiphysics, equation of motion for a particle gives the particle trajectories,

$$m_p \frac{d\mathbf{v}_p}{dt} = \mathbf{F}_{rad} + \mathbf{F}_{drag} + \mathbf{F}_g, \quad (2.23)$$

where m_p is particle mass, \mathbf{v}_p is particle velocity, \mathbf{F}_{drag} is the drag force and \mathbf{F}_g is gravity force. Acoustofluidics nature gives an opportunity to model flow inside the microchannel with the Stokes equation (Low Reynolds number). Thus, Creeping Flow Module embedded on COMSOL Multiphysics is used to calculate \mathbf{F}_{drag} .

2.4 Determining the baseline separation scenario

Although an acoustofluidics chip has many different parameters that affect its performance, determining the operating frequency is the first parameter that should be determined for simulation models. Operating (resonance) frequency calculated from 1D simplified models is no longer valid for 3D and coupled system analysis. In order to find the efficient working frequency for each chip design, firstly, simulation models run for a wide frequency range of 100 kHz to capture the pressure maxima generated inside the channel. The final value of frequency is determined by

a narrower frequency range of 4-10 kHz around the peak pressure values. Figure 2.7 is shown as an example of silicon simulation frequency evaluation.

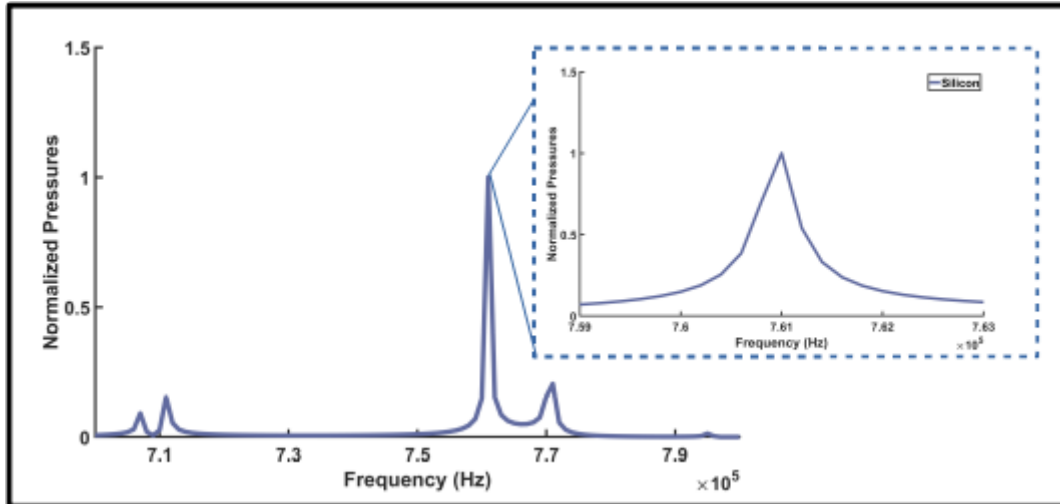


Figure 2.7 Normalized pressures for frequency sweep

Once the frequency is obtained, the voltage level is adjusted for the possible best separation of different sized particles from each other and the performance metrics recorded. MATLAB is used to post-process the data coming from the simulation. In this thesis, COMSOL Multiphysics is used for all simulations, and MATLAB is used for post-process. Final arrangements on graphs are adapted in LibreOffice Draw.

CHAPTER 3

INVESTIGATION OF EFFECT OF DESIGN AND OPERATING PARAMETERS

In this chapter, using the simulation model in Chapter 2, different cases are evaluated according to the created performance metrics such as purity, yield, stuck, average force on particles, residence time, and separation metric. The geometric model consists of a piezoelectric actuator, silicon chip, microfluidic channel, and glass lid, as shown in Figure 3.1A. Many parameters should be considered in the design process, as shown in Figure 3.1.

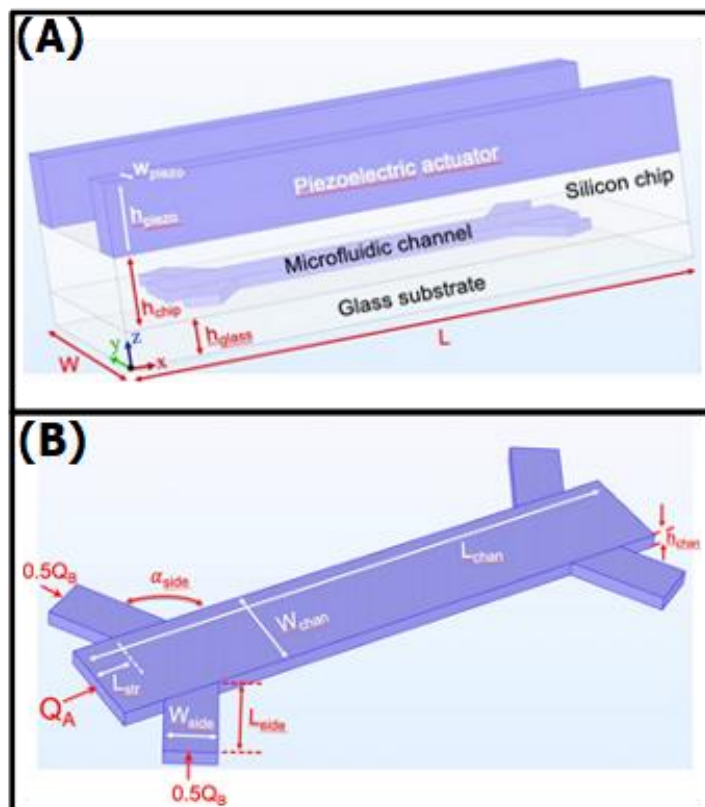


Figure 3.1 Geometric model of the chip and chip parameters

Simulations performed in this section include different channel widths, frequencies, microchannel depths, and flow rates; results are compared in terms of performance

metrics. Domains are meshed such that maximum element size is at most one-tenth of the acoustic wavelength or less and the time step for particle motion is decided to be 0.1s to obtain satisfactory resolution for the given flow rates. In addition, in COMSOL, predefined wall corrections that consider hydrodynamic particle–wall interactions for calculating the drag forces are also included in some case studies and observed no meaningful change. The simulations for each case in this chapter typically take about 15-20 minutes on a 6-cores i7-8750h processor at 2.20 GHz and with 32 GB of RAM.

3.1 Performance Metrics

The simulation uses 660 particles (small and large particles in half-shares), which are released 11 times from randomly distributed locations of the inlet side branch, 60 particles at a time. Particle sizes may vary according to the case's intention; however, 5 μm , 8 μm , and 15 μm sized particles are used in simulations. Nomenclature is determined as $P_{Size}^{Location}$ denotes the number of particles according to their sizes (either small or large) and locations (either main, side, or stuck) and $\mu_{Size}^{Location}$, $\sigma_{Size}^{Location}$ are mean value and standard deviation of particles locations in the y-direction.

The ratio of the number of particles at the intended exit to all particles at that exit gives **purity** metric, and it can be calculated for main and side exits,

$$\mathbf{Purity}_{\text{main}} = \frac{P_{large}^{main}}{P_{large}^{main} + P_{small}^{main}}, \quad (3.1a)$$

$$\mathbf{Purity}_{\text{side}} = \frac{P_{small}^{side}}{P_{large}^{side} + P_{small}^{side}}. \quad (3.1b)$$

Yield metric can be defined as the number of particles that exit through the right exit to the total number of that particle. Yield metric can be assessed for large and small particles such as

$$\mathbf{Yield}_{\text{large}} = \frac{P_{\text{large}}^{\text{main}}}{P_{\text{large}}^{\text{total}}}, \quad (3.2a)$$

$$\mathbf{Yield}_{\text{small}} = \frac{P_{\text{small}}^{\text{side}}}{P_{\text{small}}^{\text{total}}}. \quad (3.2b)$$

Particles can stick to the microchannel walls during particle motion due to the vertical component of the acoustic radiation force, which generally happens when the channel height is comparable to the wavelength. Additionally, particles may be stuck at the entrance region if there is a pressure gradient inside inlet branches. The relative values of drag force and acoustic force inside the channel lead to some of the particles having very slow velocity inside the channel and could not reach the exit channels. They are also counted as stuck particles. Thus, the **stuck** metric defines the percentage of the total number of stuck particles on the channel,

$$\mathbf{Stuck}_{\text{large}} = \frac{P_{\text{large}}^{\text{stuck}}}{P_{\text{large}}^{\text{total}}}, \quad (3.3a)$$

$$\mathbf{Stuck}_{\text{small}} = \frac{P_{\text{small}}^{\text{stuck}}}{P_{\text{small}}^{\text{total}}}. \quad (3.3b)$$

Time-dependent average force, **Force**_{size}, for each different sized particle during flow until the particle leaves the chip or gets stuck. Even if the particle size ratio is an exact number, for instance, 3 (15 μm / 5 μm), the time-averaged force ratio during the flow may not be 27, unlike the ideal theory. Design parameters affect the acoustophoretic force distribution inside the medium. Depending on the starting location, each particle experiences a different level of acoustophoretic force changing with the trajectory they follow inside the channel. Therefore, the time-dependent average force may vary according to the chip design, even for the particles with the same size.

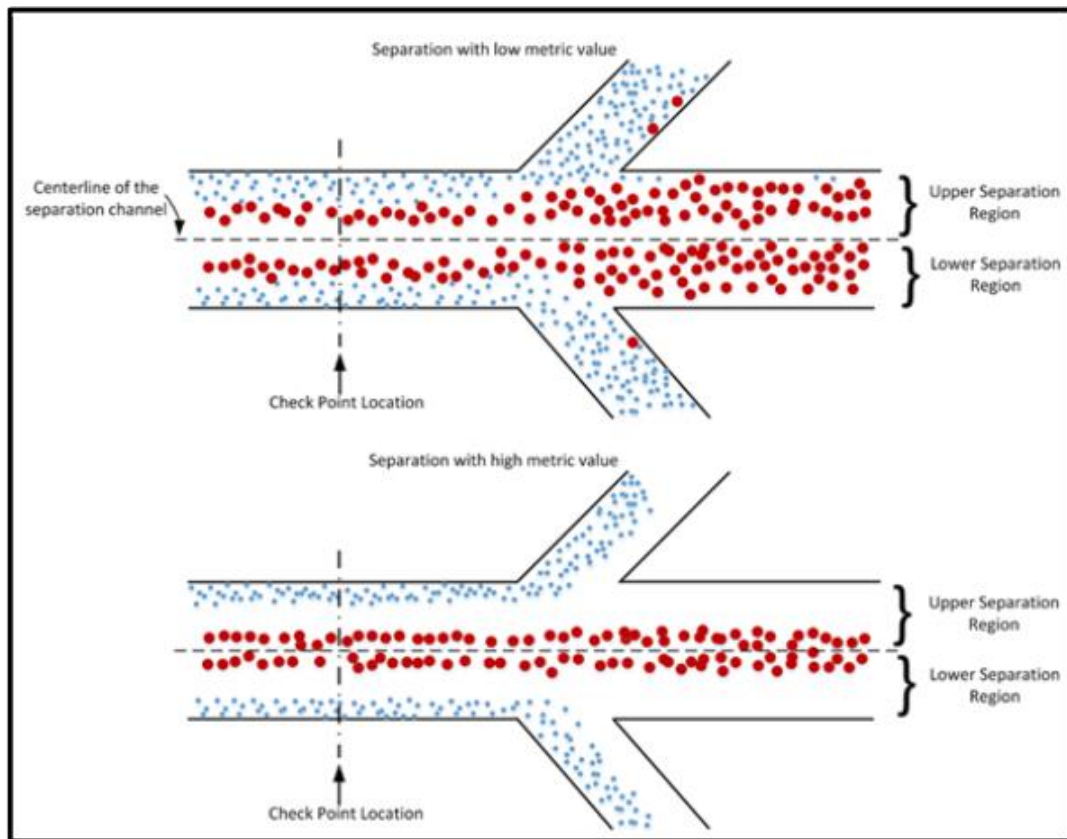


Figure 3.2 Separation metric representation examples

The need for comparison of simulations that have similar purity, yield and stuck particles give an important reason to constitute the separation metric. For instance, two chips with different parameters, shown in Figure 3.2, can separate particles with close purity, yield, and stuck values; however, the first chip has a narrower width of focused particle, and the distance between smaller and larger particle is greater than the other chip. Thus, separation metric has a meaning in terms of separation quality and is expressed for upper and lower separation region along the y-axis (orthogonal axis to the flow direction). The chip designs with higher separation metric results in a process more robust to variations chip design parameters. Particles' y-axis locations stored at a specific checkpoint location (shown in Figure 3.2), which is selected close to the exit, and mean values and standard deviations of the location of particles at the checkpoint determine the **separation metric (SM)** as shown below:

$$\mathbf{SM}_{upper} = \frac{\mu_{large}^{upper} - \mu_{small}^{upper}}{(\sigma_{large}^{upper} - \sigma_{small}^{upper}) / 2}, \quad (3.4a)$$

$$\mathbf{SM}_{lower} = \frac{\mu_{large}^{lower} - \mu_{small}^{lower}}{(\sigma_{large}^{lower} - \sigma_{small}^{lower}) / 2}, \quad (3.4b)$$

$$\mathbf{SM} = \frac{(\mathbf{SM})_{upper} + (\mathbf{SM})_{lower}}{2}. \quad (3.4c)$$

The amount of time for a particle that can successfully exit through one of the branches is also recorded between the inlet and outlet. Averaging of all successful particle travel time is called **mean residence time**.

3.2 Case Studies for Investigation of Design and Operation Parameters on Acoustophoresis Performance

Geometry, operational, and particle related parameters used in numerical analysis are given in Table 3.1. Unless flow rate is a parameter under investigation, side stream flow rates are fixed at 10 $\mu\text{L}/\text{min}$, and the mainstream flow rate is fixed at 60 $\mu\text{L}/\text{min}$; in total, the solution flows inside the channel with a flow rate of 80 $\mu\text{L}/\text{min}$.

Table 3.1 Simulation parameters.
The material properties are taken from COMSOL Material Library
at $T = 20^\circ$ unless otherwise stated

Geometric Parameters			
Length of chip	L	8.0	[mm]
Width of chip	W	4.0	[mm]
Thickness of glass substrate	h_{glass}	0.5	[mm]
Thickness of chip	h_{chip}	1.0	[mm]
Thickness of PZT actuator	h_{piezo}	1.0, 2.0, 3.0, 5.0	[mm]
Width of PZT actuator	W_{piezo}	$W/6$	
Length of channel	L_{chan}	6.0	[mm]
Height of channel	h_{chan}	0.15, 0.25	[mm]
Width of the main channel	W_{chan}	0.33, 0.66, 1.0, 1.65	[mm]
Width of side-channel	W_{side}	$W_{\text{chan}}/2$	[mm]
Angle for side-channel	α_{side}	120°	[$^\circ$]
Diameter of particles	d_p	5.0, 8.0, 15	[μm]
Operating Parameters			
Flow rate at main channel	Q_A	10, 20, 30, 60	[$\mu\text{L}/\text{min}$]
Flow rate at side channels	Q_B	10	[$\mu\text{L}/\text{min}$]
Frequency of applied voltage	f	0.4, 0.7, 1.0, 2.0	[MHz]
Polystyrene			
Density	ρ_p	1050	[kg/m^3]
Speed of sound	c_p	2300	[m/s]
Silicon			
Isotropic structural loss coefficient	η_s	1×10^{-4}	-
Glass			
Isotropic structural loss coefficient	η_s	1×10^{-3}	-

3.2.1 Case 1: Introductory Case, Separation in 1mm channel width

Case 1 is aimed as a baseline and introductory case to understand the typical values for the performance measurement metrics. 5 and 15 μm particle solution entered the 1mm width-channel from the inlet's side branches and separated at the exit part of the trifurcated zone, as seen in Figure 3.3A. The corresponding frequency value of the width should be around 700 kHz; after the frequency sweep is run, as stated in Chapter 2.4, the resonance frequency for acoustophoretic force is found as 722 kHz. In Figure 3.3B, the purity levels for 5 and 15 μm particles are shown to be high, meaning that particles are not getting mixed at the end of the channel and goes out from the intended exits. The reason for which yield values are lower than the purity values is due to stuck particles inside the channel. The ratio of the average acoustic force acting on large and small particles during the flow is nearly 30; the ratio is expectedly somewhat different than the 1D approximation prediction which is 27. The separation metric is calculated as 4.2, but separation metric values are meaningful when compared to a different case study for understanding the effect of that parameter on separation performance. Lastly, the mean residence time is calculated as 1.3s.

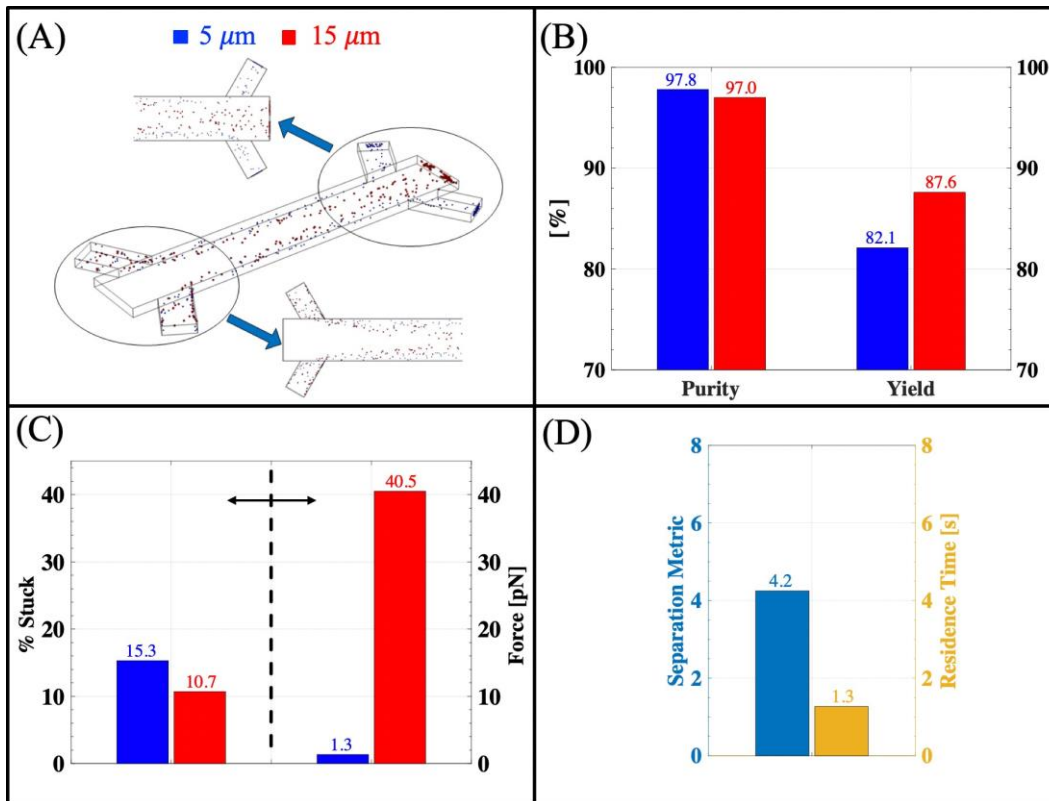


Figure 3.3 Separation and performance metrics in 1.0 mm channel with 700 kHz resonance: (A) separation of 5 μm and 15 μm particles, (B) purity and yield, (C) % stuck and force, (D) separation metric and residence time

3.2.2 Case 2: Separation on different channel widths at corresponding frequencies

Case 2 compares the acoustophoretic performance of different channel widths, where the corresponding resonance frequencies are input as the excitation frequency for each different channel width. The most used channel width and frequency values in literature are around 330 μm with a corresponding resonance frequency of 2 MHz [3], [25], [81]; thus, channel widths are selected, starting from 330 μm to 1.65 mm, which have estimated resonance frequency values that correspond to piezoelectric thicknesses of 1mm (~2MHz), 2mm (~1MHz), 3mm (~0.7 MHz), and 5mm (~0.4 MHz).

5 μm and 15 μm particles are used for case 2; purity and yield values, shown in Figure 3.4A, are high and similar for 2 MHz, 1 MHz, and 0.7 MHz. On the other hand, the yield value of 0.4 MHz is dramatically decreased, and smaller particles are observed to escape to the main exit, resulting in lower purity levels. Particles that are stuck inside the channel are one of the reasons for low yield values in 0.4 MHz-chip. In general, it is observed that the number of stuck particles in the channel increases when the resonance frequency is smaller (or when the channel width is larger), which can be observed from Figure 3.4B. The chip vibrated at 2 MHz frequency has a channel width of 0.33 mm, while the 0.4 MHz-chip has a channel width of 1.65 mm, and all share the same channel height. This fact results in higher flow velocities in channels with a smaller width and slower velocities in the wider channels. Therefore, particles have more time to move through the channel's top or bottom side, and the stuck value increases while the channel width increases. Besides, higher flow velocities are the reason for the required force for separation to increase when the channel width decreases, as shown in Figure 3.4C. Moreover, a lower resonance frequency chip has a higher residence time. The separation metric indicates that a chip has a 1 MHz resonance frequency gives a better separation metric. In contrast, expectedly the 0.4 MHz chip has a significantly low value of separation, as shown in Figure 3.4D. Finally, the inlet and outlet images in Figure 3.4E gathered from 1 MHz and 0.4 MHz chips show a bad and a good case of the separation metric.

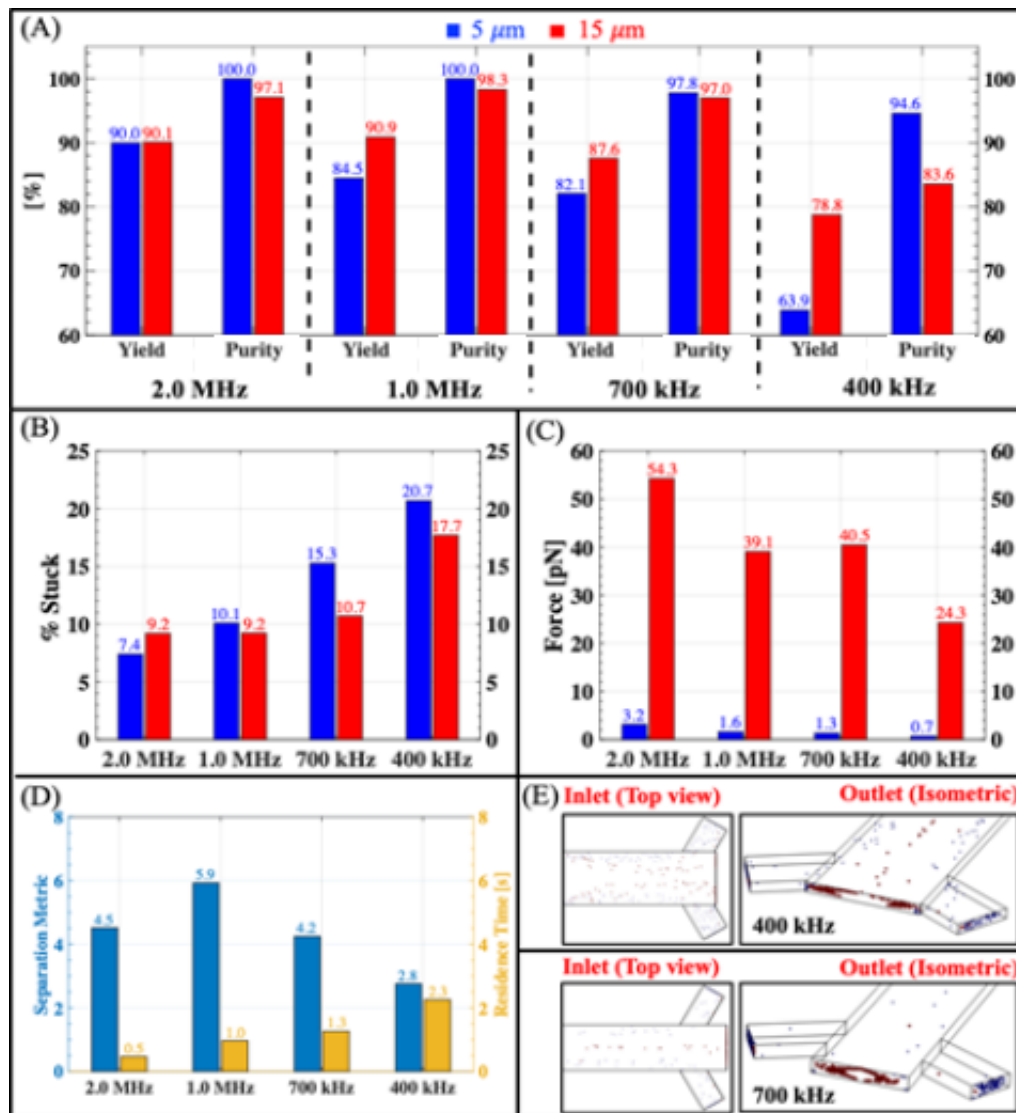


Figure 3.4 Performance metrics and separation at different resonance frequencies: (A) Purity and yield, (B) % stuck, (C) average acoustophoretic force, (D) separation metric and residence time, (E) separation of 5 μm and 15 μm particles

3.2.3 Case 3: Separation on different channel widths at the same frequency

Case 3 is evaluated to investigate the case where the transducer's actuation frequency does not result in a wave that is half the wavelength of the acoustic wave inside the channel. This case study aims to answer if the chip can be used for the separation of particles, even if the half-wavelength condition is not satisfied. Thus, channel widths

and all of the parameters in case 2 are maintained. However, the piezoelectric material of 5 mm thick corresponding to 0.4 MHz is used for every chip. Figure 3.5A shows that all chips achieve particle separation with high purity levels; yet, yield values are not as good as the purity. In Figure 3.5B, Stuck values can explain the weak values of yield; the lowest value of stuck particles occurs for the chip on which the excitation frequency and the channel width are matched. In contrast, a high value of stuck occurs for the 1mm channel width and results in the lowest yield values. Separation metrics in Figure 3.5E indicates that separation quality is better in 660 μm and 1mm channel width since separation metric does not account for the stuck values. Figure 3.6 shows the acoustic pressure gradients inside the different channels at 0.4 MHz and corresponding voltage levels shared in the caption. Although similar values of acoustic pressures are developed for all channel widths, the required voltages vary. As expected, the 1.65 mm channel width consistent with the actuation frequency requires lower voltage than the others. It can be said by comparing case 2 and case 3 that the chip's voltage requirement with unmatched excitation frequency highly increases. For instance, the 1 mm chip requires 3 V at 722 kHz to separate particles in Figure 3.3. However, if the actuator geometry is changed to the 5mm thickness actuator with resonant frequency 400 kHz, the voltage requirement of 1 mm channel width increases to 120 V. Those high voltage values will practically cause the heating problems in the chip.

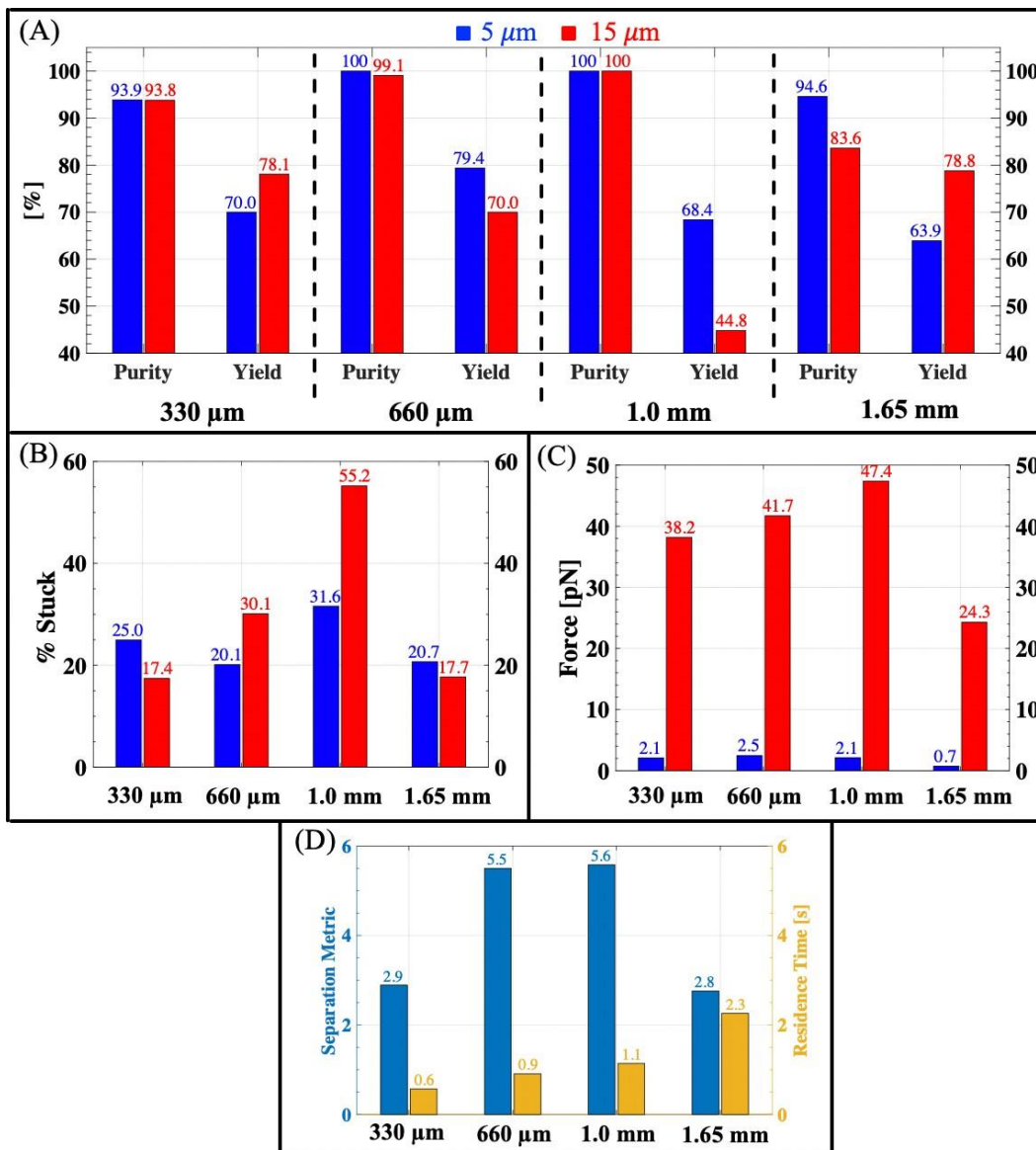


Figure 3.5 Performance metrics and separation at fixed resonance frequencies: (A) Purity and yield, (B) % stuck, (C) average acoustophoretic force, (D) separation metric and residence time

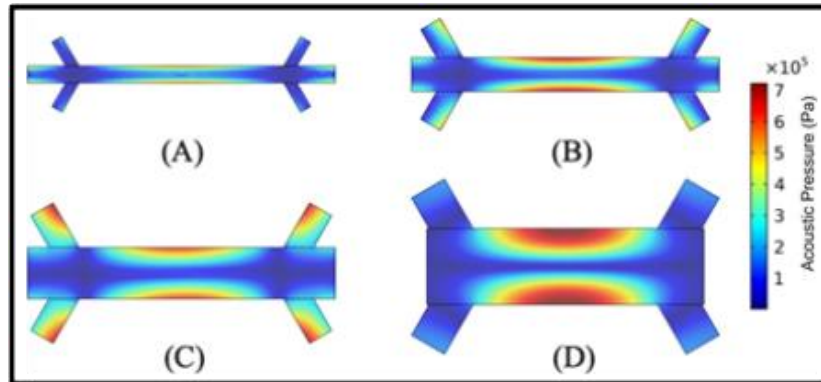


Figure 3.6 Acoustic pressure gradients for channel widths excited at 0.4 MHz

- (A) Channel Width = 330 μm , Voltage = 90 V;
- (B) Channel Width = 660 μm , Voltage = 250 V;
- (C) Channel Width = 1 mm, Voltage = 120 V;
- (D) Channel Width = 1.65 mm, Voltage = 16 V;

3.2.4 Case 4: Separation on different channel heights

In case 4, simulations are focused on evaluating channel heights, which are arranged as heights of 50 μm , 150 μm , 250 μm , 500 μm , 750 μm , and 950 μm . The other parameters are taken to be the same as in Case 1. So, 0.7 kHz resonance frequency excitation in a chip with 1 mm channel width is used for separation of 5 μm and 15 μm particles with a total flow rate of 80 $\mu\text{L}/\text{min}$. Figure 3.7A shows the purity and yield values corresponding to different channel heights, indicating that the 250 μm channel height gives better results than the others. Values of the purity and yield decrease while the channel height increases; however, this same pattern is not valid for the stuck values, as shown in Figure 3.7B. Weaker acoustic forces that occurred in higher channel heights might be a reason for the low yield, purity, and stuck values at the same time. Separation metrics in Figure 3.7D also points out that 250 μm channel height is favorable. In the same figure, residence time increases while depth increases since the fixed flow rate results in higher velocities in smaller channel depths. The velocity profile developed inside the deeper channel leads particles to have a broader range of velocities. Thus, the smaller particles with slower velocities tend to exit through the central channel (unintended channel) while the voltage

increases. In contrast, the low voltage causes large particles having higher velocities to exit through side channels. Therefore, setting an excitation level that ensures efficient separation is more challenging for chips with higher channel depths, and separation performances decrease while the depth gets higher. Figure 3.7E is an excellent example of that situation; slower 5 μm particles (red ones) exit at the main channel while faster 15 μm particles (blue ones) tend to go out at the side channel.

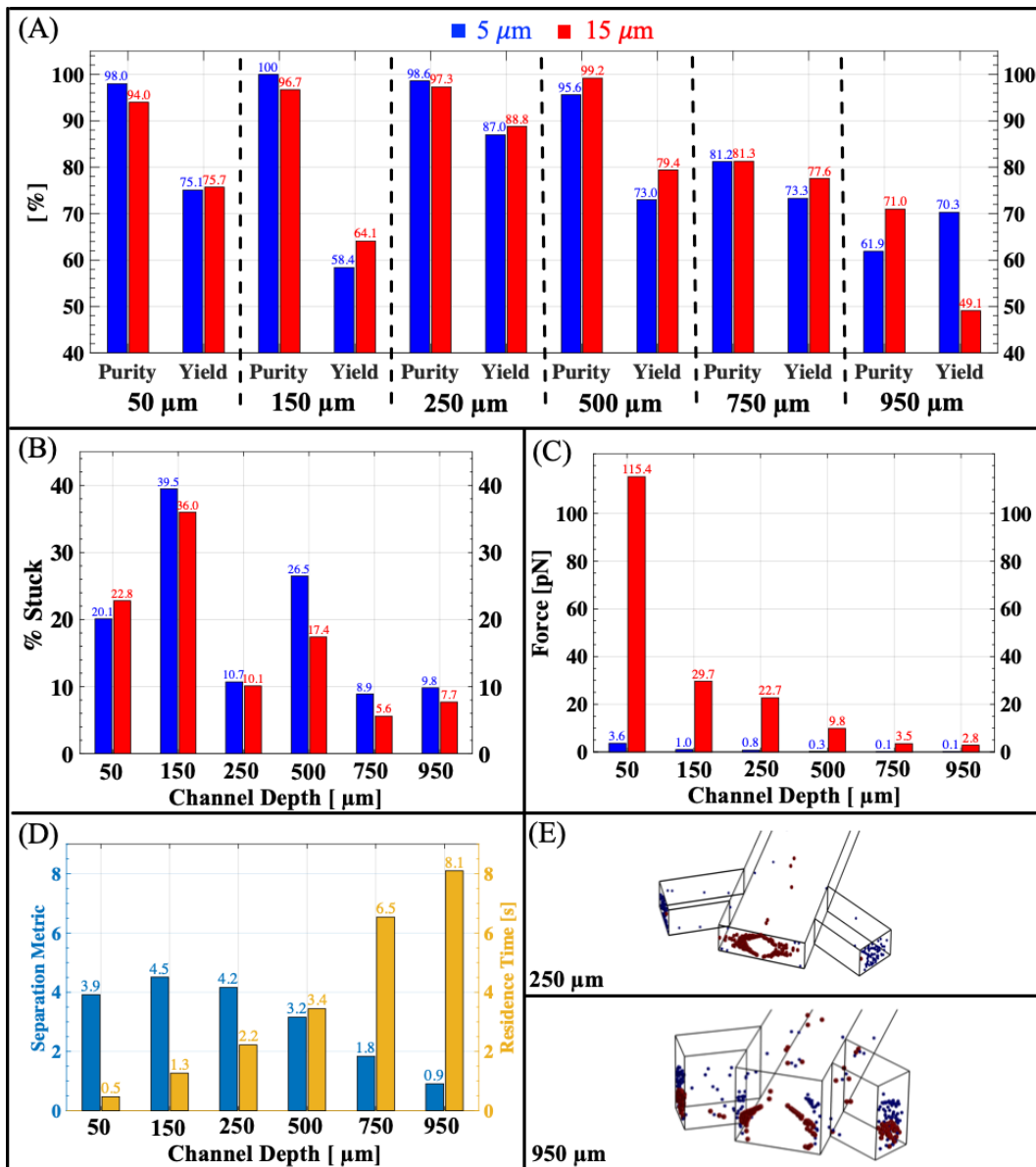


Figure 3.7 Performance metrics and separation at different channel heights: (A) Purity and yield, (B) % stuck, (C) average acoustophoretic force, (D) separation metric and residence time, (E) separations in heights of 250 μm and 950 μm

3.2.5 Case 5: Separation at different main/side flow ratios

The trifurcated design provides particles to move toward the channel sidewalls caused by the main channel inlet flow (buffer flow). Hence, the main inlet flow rate determines the particle positions for a fixed side flow rate. In case 5, different ratios of main flow to side flow are evaluated in terms of performance metrics; the side flow, Q_B , is fixed at 20 $\mu\text{L}/\text{min}$ while the main flow Q_A is used to change the flow ratios to 1, 2, 3, 5, and 10. 0.7 MHz chip corresponding to 1mm channel width is used for flow ratio simulations. Table 3.2 shows the values of Q_A , Q_B , and voltage.

Table 3.2 Main (Q_A) and Side (Q_B) flow ratios and corresponding voltage value to achieve separation

Q_A/Q_B	Q_A [$\mu\text{L}/\text{min}$]	Q_B [$\mu\text{L}/\text{min}$]	Voltage [V]
1.0	20	20	6
2.0	40	20	9
3.0	60	20	11
5.0	100	20	14
10	200	20	20

Purities of outlet channels increase with increasing flow ratio, as shown in Figure 3.8A. Although the stuck value of flow rate ratio 5 is slightly higher than the flow rate ratio of 3 as shown in Figure 3.8B, the flow rate ratio of 5 results in higher values of purity and yield. Besides, Figure 3.8C depicts that the force required for a flow rate ratio of 5 is significantly lower than the cases with similar value flow rate ratios. Because of the increased flow rate, the flow rate ratio of 10 results in a high force value which is around 80 pN. Separation metric increases for increasing flow rate ratio; in contrast, the residence time decreases with increasing flow ratios in Figure 3.8D. It can be referred from Table 3.2 that the voltage requirements increase almost linearly with the flow rate ratio.

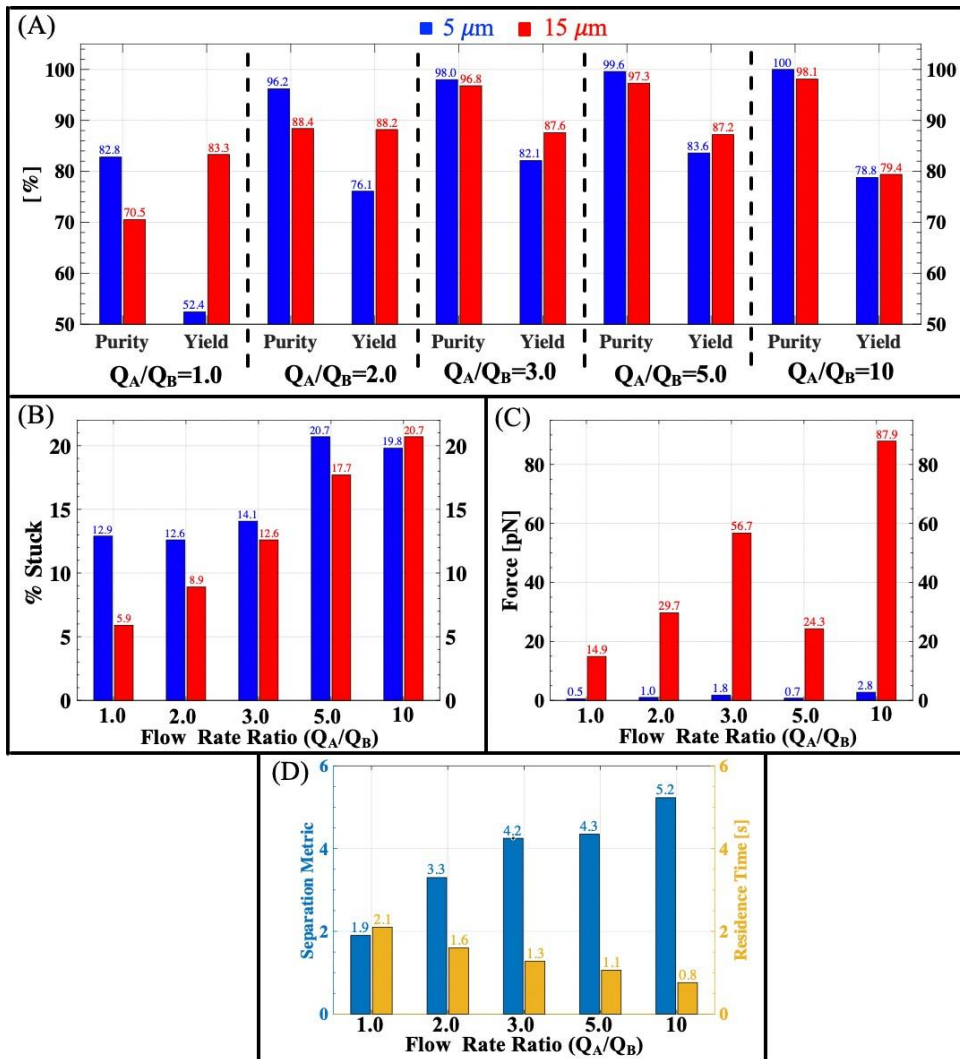


Figure 3.8 Performance metrics at different main/side flow ratios: (A) Purity and yield, (B) % stuck, (C) average acoustophoretic force, (D) separation metric and residence time

3.2.6 Case 6: Separation of closer size particles

Case 6 demonstrates how the difference in particle diameter values affect the chip's separation performance. Until Case 6, 5 μm and 15 μm particles are used in separation simulations. In this case, closer size particles are used, such as particles with 5 μm and 8 μm diameters. Simulations for separating similar particles are set to be the same as in [Case 2](#), which has different channel widths corresponding to

different excitation frequencies. Although the purity and yield values are significantly dropped in comparison to Case 2, a similar pattern is displayed in Figure 3.9. Purity and yield values decrease with increasing channel widths as shown in Figure 3.9A. Also, stuck values increase while decreasing frequency values in Figure 3.9B. As in Case 2, 1 MHz and 2 MHz chips give better results than 0.7 MHz and 0.4 MHz chips. Figure 3.9C shows the average forces, and Figure 3.9D represents separation metric and mean residence time values. 1 MHz chip has the highest separation metric value as in Case 2.

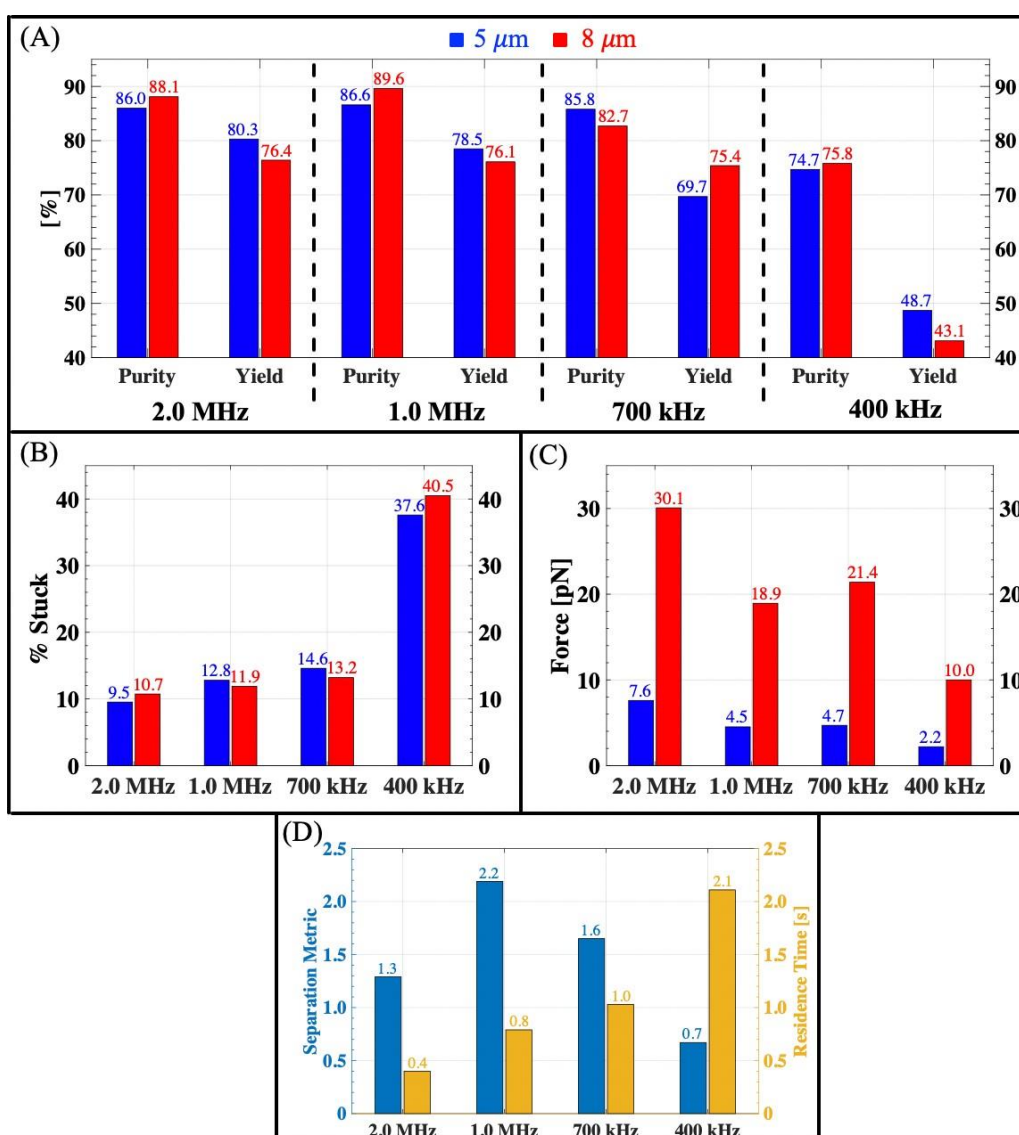


Figure 3.9 Performance metrics for closer particles: (A) Purity and yield, (B) % stuck, (C) average acoustophoretic force, (D) separation metric and residence time

3.2.7 Case 7: The effect of particle release location and size distribution

Case 6 shows that the separation performance metrics have significantly dropped when particle diameters get closer to each other. An improvement for that case can be implemented by releasing particles from a focused region on the side channel cross-sectional area. In the previous cases, each of the 660 particles starts at a random position in the regular case, but in this case study, they will be released from confined regions of the side channel cross-sections. Case 7 is designed to analyze the effect of starting position on separation metrics. The chip with 0.7 MHz corresponds to 1 mm channel width is used for simulation. The depth of the channel is chosen to be 250 μm . Figure 3.10 illustrates the different starting positions from the baseline case to the quarter depth and quarter width case. The first subplot shows the baseline in which particles enter the channel over the entire cross-section. The second subplot shows that particle starting positions are confined to the quarter width of the channel cross-section while particles enter the microchannel through the quarter height of the channel cross-section in the third subplot. The last subplot shows the combination of second and third cases where particles are released from a focused region, which is a quarter of the width and a quarter of the depth of the side channel cross-section.

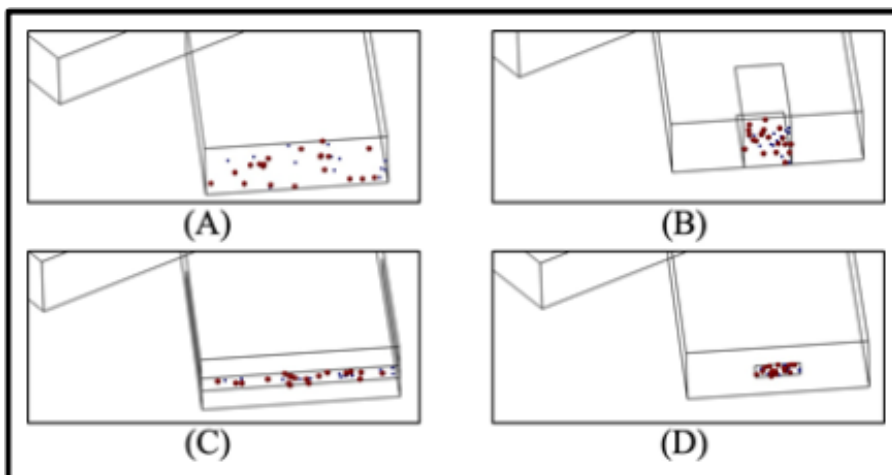


Figure 3.10 Particle release positions: (A) Baseline, (B) Quarter width, (C) Quarter Depth, (D) Quarter Depth/Width

Figure 3.11A shows that the confined starting region provides significant improvements. Focused starting locations help to improve purity and yield values compared to the baseline. In particular, the purity and yield reach the value of a hundred percent when the quarter width-quarter depth configuration is applied.

In reality, particles (or living cells) may have a statistical distribution for their diameter values, which will make the separation process more challenging. Figure 3.12 shows the normal distributions of 5 μm and 8 μm particles in which the largest value of 5 μm particles is 5.8 μm while the smallest member of 8 μm group is 6.8 μm . These two values are sufficiently close to each other to make acoustophoretic separation challenging. Figure 3.11B shows the purity and yield values for particles with size distribution. Baselines have similar values in both cases; however, confined configurations of quarter-width and quarter-depth is affected by the size distribution. On the other hand, the quarter width-quarter depth configuration remains to separate particles with a hundred percent success, meaning that the acoustophoretic chip selectivity can be considerably high with the confined release location configuration. Figure 3.11C shows the separation metric values of configurations with and without size distribution; even though the particle separation is succeeded perfectly, the separation metric reduces a considerable amount with size distribution. Another remark deduced from Figure 3.11A-B is confined release locations along the depth direction gives a better result than confined release locations along the width direction. Images taken from the outlet region for different configuration with size distribution is shown in Figure 3.12B.

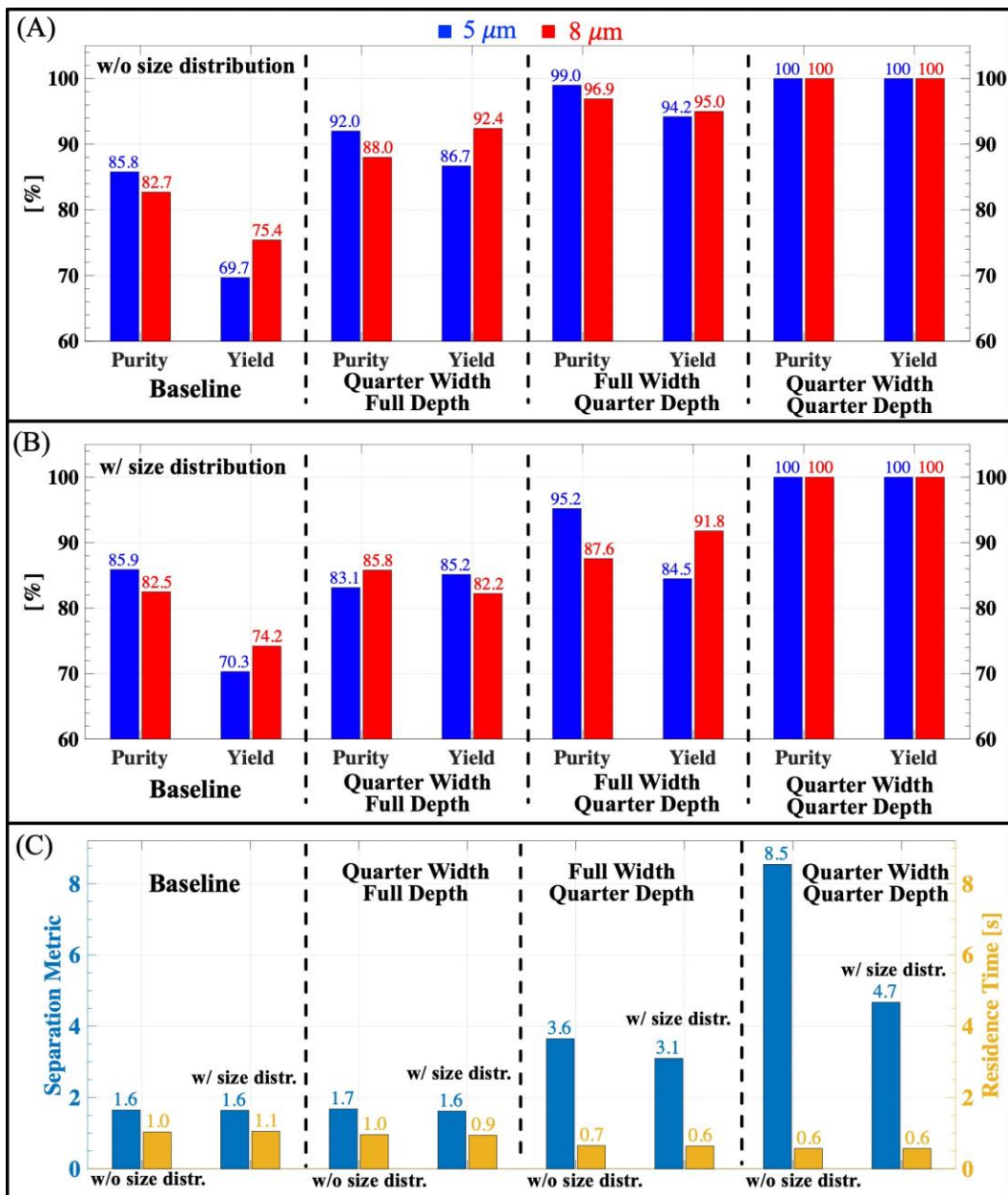


Figure 3.11 Performance metrics for similar particles at different focusing configurations: (A) Purity and yield (without size distribution), (B) purity and yield (with size distribution), (C) separation metric and residence time with and without size distribution

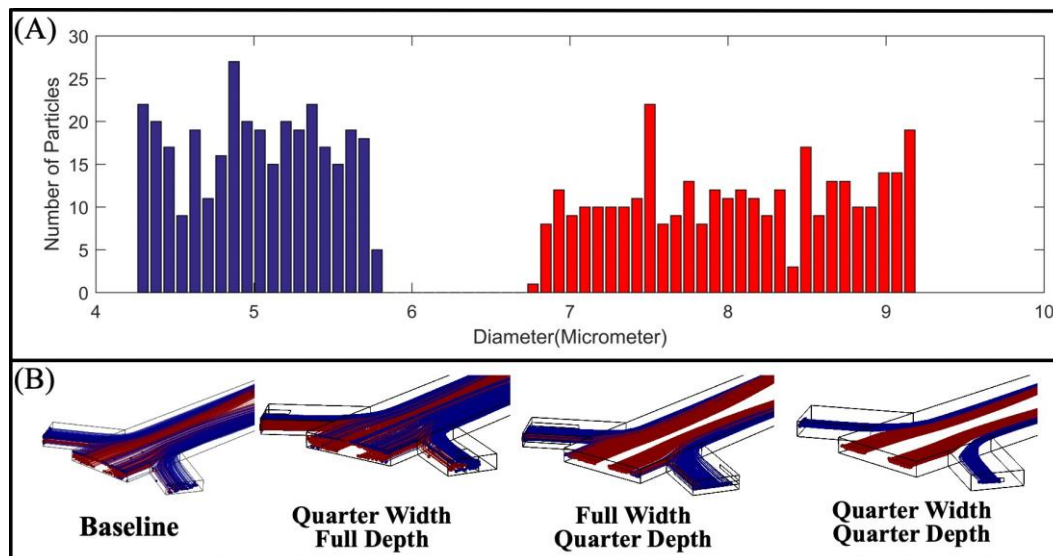


Figure 3.12 Particle size distributions and release location configurations

3.3 Discussion of Results

High-frequency acoustofluidic chips have better performance metric values than the lower ones. Even though the actuation frequency of the chip is not adjusted to fit half-wavelength inside the channel width, it is possible to separate particles. However, as the difference between channel width and half-wavelength increases, the voltage requirement increases, which may not be possible in real-life applications. The gradient of acoustic radiation force and velocity field increases while the channel width increases, resulting in weaker separation. A low flow rate ratio that causes particles to move close to the center of the channel cannot achieve high-performance separation; in contrast, a high flow rate ratio causes particles to move close to the channel sidewalls, requiring higher voltages to separate particles. Performance metrics decrease while particle sizes become closer to each other. However, narrowing the region of release for particles can improve the separation.

CHAPTER 4

UNDERSTANDING THE EFFECTS OF MANUFACTURING AND ASSEMBLY ERRORS ON ACOUSTOPHORETIC PERFORMANCE

In this part of the thesis, the introduced simulation method focuses on the sensitivities toward errors by manufacturing and assembly. As stated in Chapter 1, mass-produced acoustofluidics chips should be manufactured such that manufactured chips have resonance frequencies close to each other within a range of 3-5 kHz. Structural changes affect the whole-body resonance frequency; thus, the tolerances from manufacturing processes should be checked whether they significantly affect the acoustophoretic performance. The simulation tool explained in the earlier chapter is used to identify dependency on each geometric parameter of the chip, which may be produced from three different materials, acrylic, glass, and silicon. Parameters for geometry, operation, and materials are shared in Table 4.1. After examining geometric parameters individually, the Monte Carlo approach is applied to analyze these parameters' compound effects gathered from practical manufacturing tolerances. Additionally, this chapter will be concluded with the investigation of the effects of piezoelectric material positioning errors on the acoustophoretic force magnitudes.

Working frequencies of three chips are swept on a wide range; frequency response and the pressure gradient inside the channel for peak points are shown in Figure 4.1; interestingly, even if the channel width is chosen as 1 mm, which corresponds to ~700 kHz according to theory, frequency sweep for acrylic chip gives around ~500 kHz as a working frequency that creates acoustic force through orthogonal direction to the flow. However, silicon and glass chips give a slightly more than 750 kHz, close to the expected resonance frequency if the medium is chosen to be water with the speed of sound 1500 m/s.

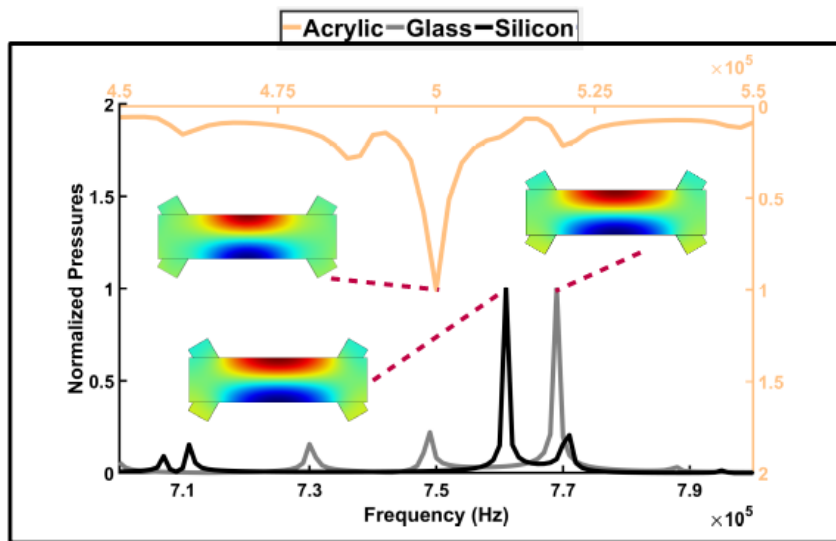


Figure 4.1 Broadband frequency responses of chips and pressure gradients for peak values

Simulations start with creating a baseline case, which is a configuration that results in efficient separation of particles via manual adjustments of the voltage value of the PZT. Starting from this successful configuration, a selected geometric dimension is slightly changed (see Table 4.1, for interval values), and particle positions and acoustic forces on them are calculated after the application of the variation. All intervals are divided into 19 points, including the 'zero-change' (baseline) case, where finer divisions are placed around the baseline case. For clarification, an example case for sensitivity on the channel width of the acrylic chip is shown in Figure 4.2. Variations from baseline values are taken to be $\pm 0.1, 0.3, 0.5, 0.7, 1, 3, 5, 7,$ and 10% ; there are 19 simulation runs for channel width, and for each of them, mean acoustic radiation forces are evaluated. Figure 4.2 shows the mean acoustic force values against the percent change of channel width. Data gathered from COMSOL are symmetrized, and a curve is fitted on them for better visualization of figures in MATLAB. The blue dashed line in Figure 4.2 represents the threshold region for separation which is determined by inspection for all baseline cases. Through experience, it can be said that the threshold value was always around 7 pN. Image of the chip outlet for the base case and the upper/lower side of the threshold are also shared with red dashed line boxes in Figure 4.2.

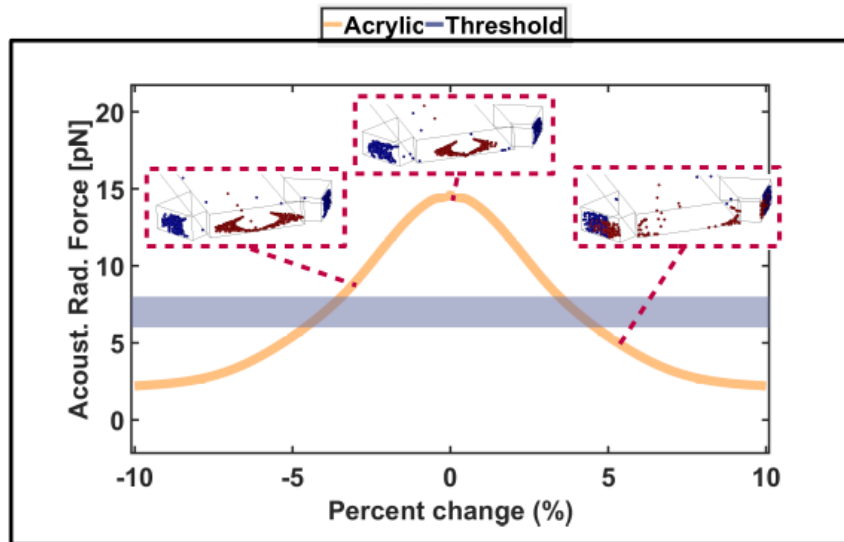


Figure 4.2 An example of sensitivity study on channel width of the acrylic chip

A similar procedure is followed to evaluate the effect of assembly errors on separation. The error values given into the simulation are selected as micrometer value, starting from 50 μm to 500 μm with 50 μm step size; hence, 11 different simulations are run for each assembly error, which is the bonding of PZT and lid to the substrate (see Figure 2.5). Moreover, variations of the PZT placement locations are examined according to changes that they induce on the acoustophoretic force. The simulations for each case typically take about 10-15 minutes on a 4-cores Intel Xeon E3-1245 v6 processors at 3.70 GHz and with 16 GB of RAM.

Table 4.1 Parameters geometry, operation conditions, and material properties

Geometric Parameters				% Changes		
				(Acrylic)	(Glass)	(Silicon)
Chip Height	h_{chip}	$\lambda_{\text{chip}} / 2$	[mm]	±5	±5	±5
Lid Height	h_{lid}	2.0	[mm]	±10	±10	±10
Chip Length	L	~6.0	[mm]	±20	±10	±10
Chip Width	W	~4.0	[mm]	±10	±10	±10
PZT Height	h_{pzt}	3.0	[mm]	±10	±5	±5
PZT Length	L_{pzt}	$\lambda_{\text{pzt}} / 4$	[mm]	±20	±10	±10
PZT Width	W_{pzt}	$\lambda_{\text{pzt}} / 6$	[mm]	±20	±10	±10
Channel Height	h_{chan}	0.25	[mm]	±20	±10	±10
Channel Length	L_{chan}	4.0	[mm]	-	-	-
Channel Width	W_{chan}	1.0	[mm]	±10	±5	±5
Diameter of particles	d_p	5.0, 15	[μm]	-	-	-
Operating Parameters						
Flow rate at main channel	Q_A	60	[μL/min]			
Flow rate at side channels	Q_B	20	[μL/min]			
Frequency of applied voltage	f	~0.7	[MHz]			
Polystyrene Particle						
Density	ρ_p	1050	[kg/m ³]			
Speed of sound	c_p	2300	[m/s]			
Material						
Isotropic structural loss coefficient	η_s	1×10^{-4}		1×10^{-3}		1×10^{-2}

4.1 Dimensional Variations

In this section, results for the effect of geometric dimension variation on the separation are presented. Figure 4.3 shows that channel dimensions except for the length are evaluated for acrylic, glass, and silicon chips. While the silicon and the glass chips have a similar pattern for channel height and width variations, the acrylic chip has a broader peak than the others. Especially, silicon and glass chips are highly vulnerable against variation on channel width in Figure 4.3B; however, the acrylic chip can tolerate slightly less than 5% variations on channel width. It shows low sensitivity to channel height deviations shown in Figure 4.3A.

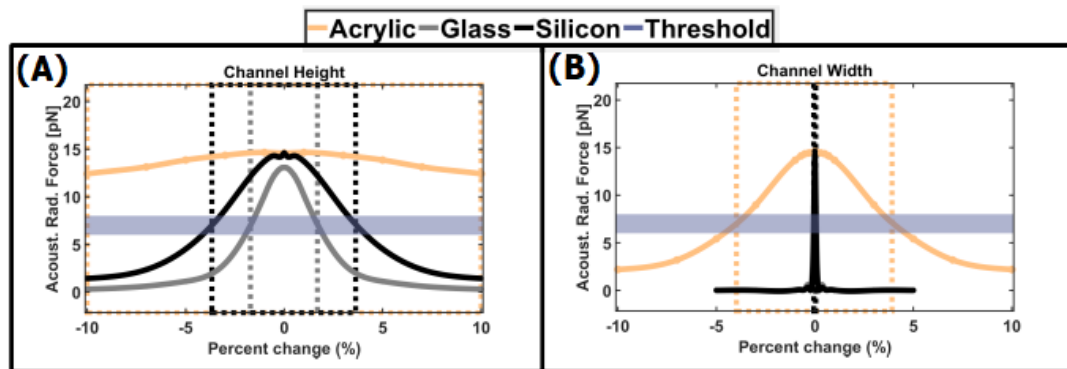


Figure 4.3 Effect of channel dimensions on separation

Chip height refers to only the height of the substrate of the chip; because the lid height may be another important dimension for the transverse resonator, while the chip length and chip width refer to both substrate and lid parts. Percent changes of chip dimensions correspond to a larger absolute value than the others due to being the longest dimensions. Figure 4.4 demonstrates the graphs of chip dimension alterations. Chip height is the bulk part that carries the acoustics waves and transfers them into microchannel with the effect of Poisson's ratio. Thus, a dramatic variation of mean acoustic radiation is expected as in Figure 4.4A; silicon and glass chips are more sensitive than acrylic against the deviations. Glass made chip is relatively more dependent to chip dimension than others are. While silicon made chip gives a similar respond for lid height changes as glass, the acrylic chip is not affected by lid height, probably due to being a much softer material than the glass lid. Figure 4.4C shows

that silicon and glass are more sensitive to chip length than acrylic is. Moreover, it can be seen that the acrylic gives varying changes in force values, which nevertheless stay on the upper side of the threshold region. Chip width might be another expected important parameter that carries the shear waves that creates a standing wave inside the channel. As in Figure 4.4D, glass and silicon are more sensitive to variations of the chip width compared to acrylic.

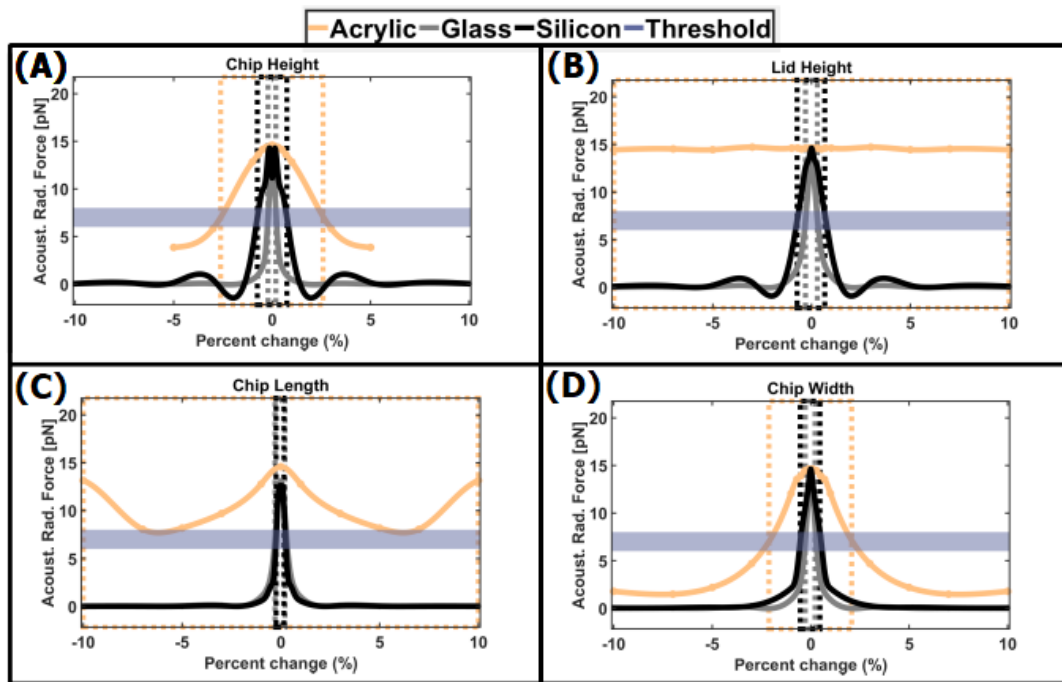


Figure 4.4 Effect of chip dimensions on separation

Piezoelectric material dimensions determine the resonant frequency. In our case, the resonant frequency is determined by PZT height; hence, the height dimension is one of the expected sensitive parameters, as in Figure 4.5A. Until this simulation, silicon and glass chips share a similar pattern against variation; however, acrylic and silicon are more sensitive than glass against PZT height variation. On the other hand, PZT length and PZT width do not excessively affect the separation; in Figure 4.5B, while silicon chip can tolerate around 5% variation on PZT length, only a slight reduction of acoustophoretic force is observed for acrylic and glass chips. Lastly, a variation on PZT width is tolerable for all three materials, as shown in Figure 4.5C.

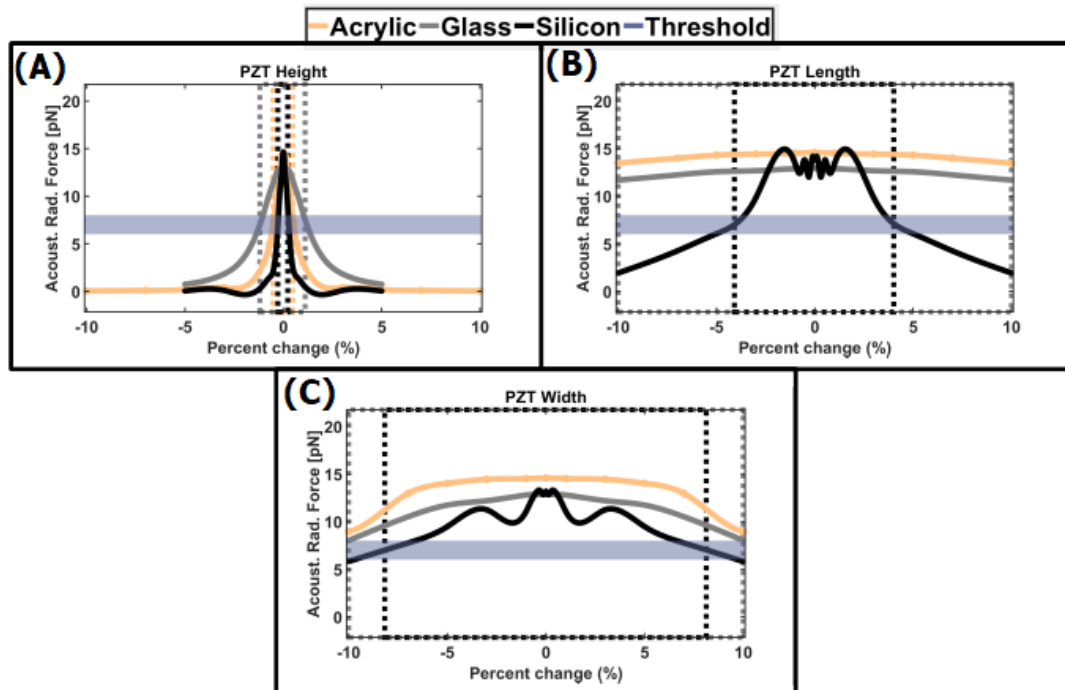


Figure 4.5 Effect of PZT dimensions on separation

4.1.1 Monte Carlo Approach on Combined Dimensional Deviations

Each geometric dimension effect on separation is evaluated one by one in the previous section; however, each fabrication step at the industrial level has a permissible limit called manufacturing tolerances. For instance, there are two different ways to produce acrylic plates, one of them is casting that has a tolerance of $\pm 10\%$ and extruded acrylic has a tolerance of $\pm 3\%$ in thickness direction [82]. Therefore, the combined effect of each dimension variation may affect the separation performance of the acoustophoresis chip even if a low tolerance value, $< \pm 1\%$ is achievable. At this point, assessing the combined effect of manufacturing tolerances on different material chips can reveal essential considerations on the material selection process.

Two different tolerances coming from the production of raw material and processing may occur in acoustofluidic chip fabrication. Dimensions are determined by the raw material itself (i.e., chip height, lid height.) or by machining the raw material. Table

4.2 shows the tolerances of each dimension gathered from manufacturers [82]–[90] while the blue background stands for the raw material tolerances, the machining tolerances are represented with the green background.

Table 4.2 Tolerances for geometric dimensions

($\pm\mu\text{m}$)	Channel Width	Channel Height	Chip Height	Lid Height	Chip Length	Chip Width	PZT Height	PZT Length	PZT Width
Acrylic	100	100	50	200	100	100	50	150	150
Glass	20	20	200	200	20	20	50	150	150
Silicon	20	20	50	200	20	20	50	150	150

In literature, a microchannel pattern is implemented on silicon or glass material by etching methods (i.e., photolithography, wet-etching) [3], [56]; however, these methods are not appropriate for mass-production lines. It is assumed that the microchannel pattern may be machined on the substrate with a thin diamond saw blade as a straight line, and trifurcated inlet and outlet part manufactured can be bonded at open sides. Figure 4.6 is a practical example of a hybrid chip produced at laboratories in Bilkent University and TOBB Economy and Technology University. It consists of the glass substrate as an acoustophoretic zone and two acrylic pieces as inlet and outlet sections. While Dicing Saw machines the microchannel (1 mm width – 250 μm depth) on a glass substrate (DISCO DAD3230 - 100 μm diamond blade thickness), computer numerical control (CNC) milling machine techniques are used to fabricate acrylic pieces. In conclusion, it is considered in simulations that silicon and glass chips are using a dicing saw to implement a microchannel while a micro-CNC milling machine patterns the acrylic chip.

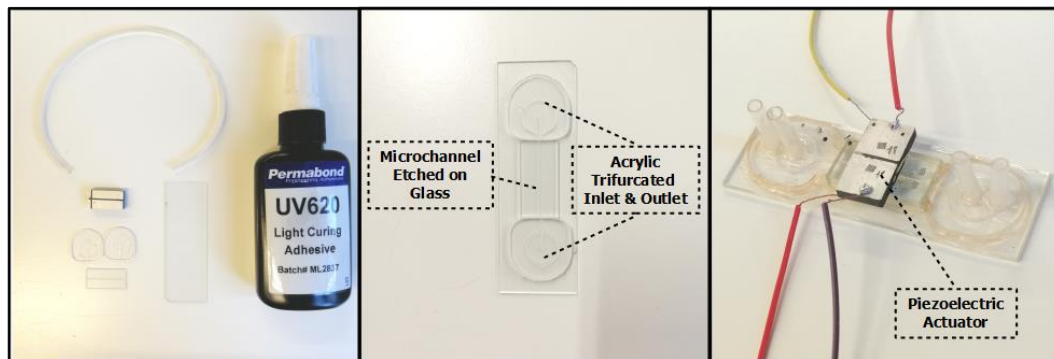


Figure 4.6 Glass-Acrylic Hybrid Chip

Monte Carlo is a computational algorithm based on repeated random sampling to solve vast ranges of problems, especially problems that have no analytical or numerical solutions or are challenging to solve. It has been used in finance, physics, and engineering areas, and there are numerous purposes and types of implementation for the Monte Carlo method. However, in our case, it is used to model the effect of uncertainty of tolerances and create a sensitivity analysis for the variations in geometric dimensions. A typical example to explain the Monte Carlo approach is approximating π 's value by generating uniformly distributed random numbers between zero and one. As shown in Figure 4.7, simple code generates numbers, and the ratio of the points inside the circle to the total number of points gives an approximated value of pi. When the generated numbers increase, the guess is getting closer to the real value of pi.

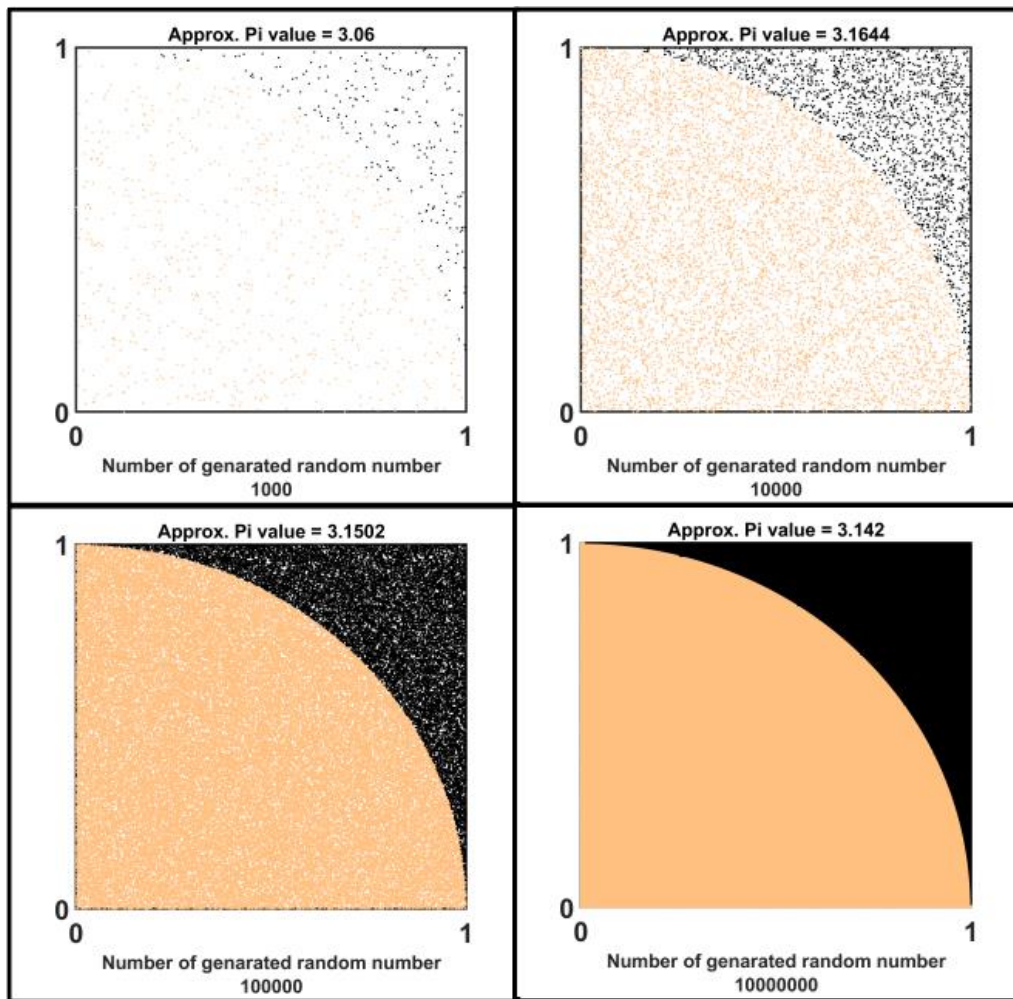


Figure 4.7 Approximation of pi values using randomly generated numbers

Uncertainties from manufacturing tolerances are implemented via the Monte Carlo approach on our simulation model discussed in previous sections. A normal distribution is selected to generate random tolerance values according to 3σ corresponds to the limit values for each dimension stated in Table 4.2. Bar plot is drawn for the generated values for acrylic channel width tolerance as shown in Figure 4.8.

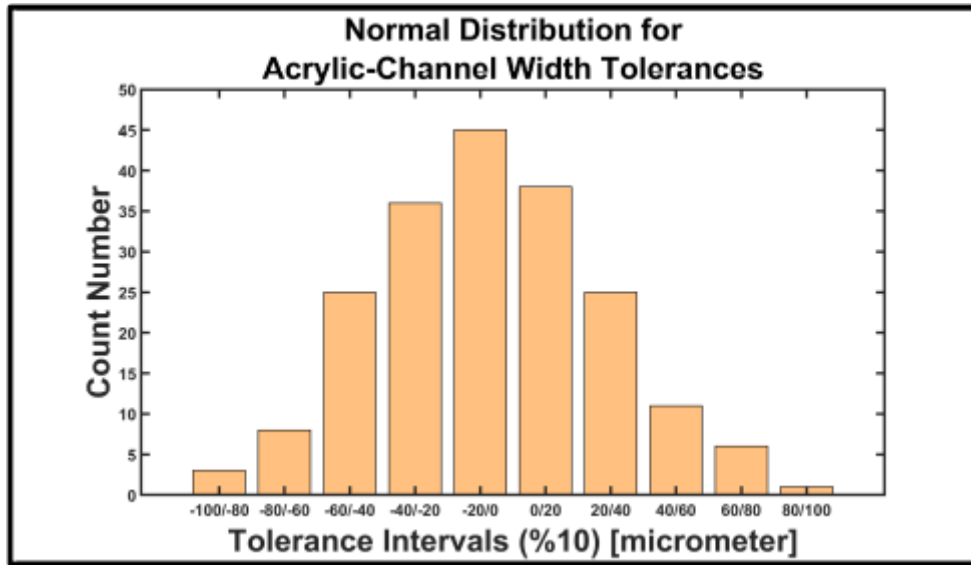


Figure 4.8 Normal distribution example for acrylic channel width case

Once the tolerances for each dimension are generated (Matrix: 200x9; the number of experiments and the number of dimensions, respectively.), two hundred simulations are solved with dimensions that have random tolerance information. Therefore, a sensitivity metric is created in order to compare each dimension's effect on separation. The sensitivity metric algorithm starts with assessing each experiment, whether separate particles or not, based on the mean threshold value. Then, each dimension value is averaged for successful experiments and failed experiments, and the sensitivity for any dimension can be calculated as:

$$\text{Sensitivity}_{\text{dimension}} = \frac{\mu_{\text{dimension}}^{\text{failed}} - \mu_{\text{dimension}}^{\text{successful}}}{|\pm T_{\text{dimension}}|} \times 100, \quad (4.1)$$

where μ is the mean values of dimensions for failed or successful events, T is the tolerance value stated in Table 4.2. Even if the sensitivity metric does not have physical meaning for manufacturing by itself; however, it can be useful for comparing geometry and material effects. Results converge the same pattern shown in Figure 4.9; thus, two hundred random generated tolerances are applied on all dimensions in each simulation for three materials.

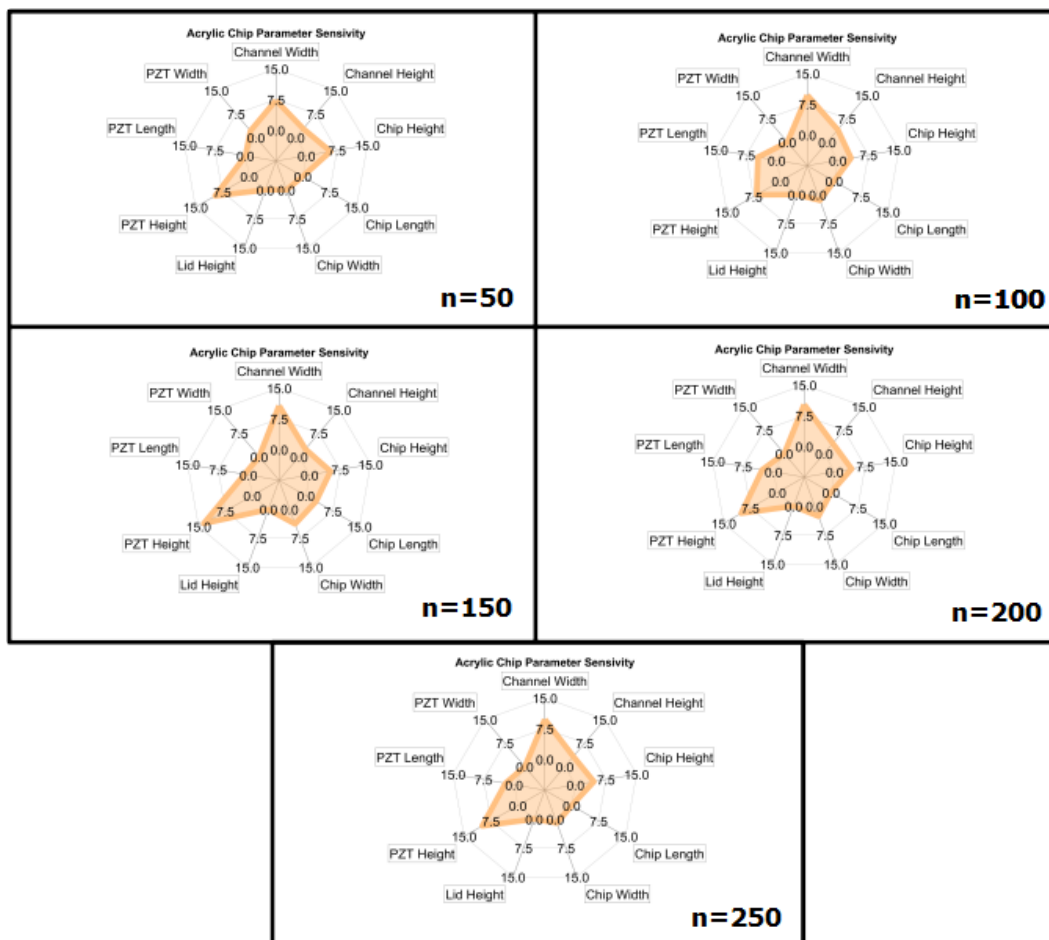


Figure 4.9 Results according to the number of experiments

An important consideration is that the silicon and glass chips are highly affected by a combined change of dimension parameters; this fact results in a few events that could continue to separate particles. For instance, Figure 4.10 shows that glass has 3/150 successful experiments, and silicon has 3/100 successful experiments. Therefore, the manufacturing tolerance for silicon and glass is decreased by ten times to gather meaningful results to compare each dimension effect.

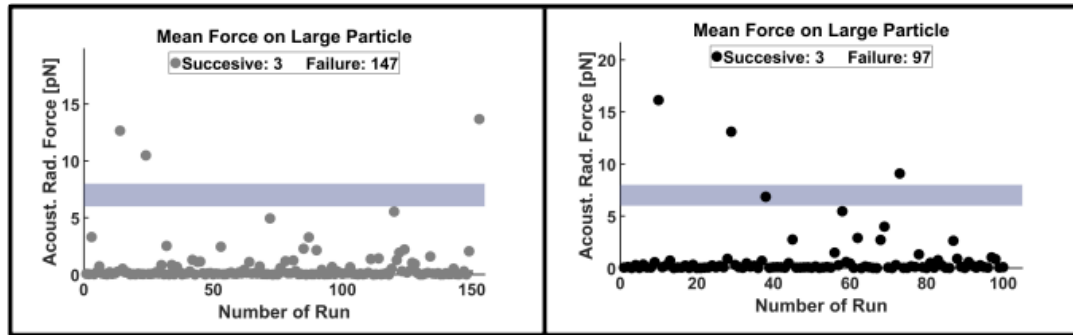


Figure 4.10 True tolerance results for silicon and glass chips

Once two hundred simulations are processed for each material in MATLAB, results including mean acoustic force and sensitivity metric are shown in Figure 4.11. While successful separation ratio over the total is counted 75/200 in the acrylic chip, the glass and silicon chip give 93/200, and 100/200 success rate with the decreased manufacturing tolerance limits as shown in Figure 4.11(A-C). There are two geometry parameters more responsive than the others, channel width and PZT height, that affect the acrylic chip's separation, as seen in Figure 4.11D. Indeed, Monte Carlo results are highly inconsistent with the results gathered in Section 4.1; for instance, lid height, chip length, and PZT width of the acrylic chip are nearly no impressions on separation in both cases. Heights of channel and chip, the width of the chip, and PZT length have a moderate impact on separation compared to the channel width and PZT height. In Figure 4.11E, considerable sensitivity is observed for channel width, chip height, and lid height of the glass chip. Chip width and height of PZT have a sensitivity value slightly less than lid height while the others have almost no impact. It can be seen in Figure 4.11F that the channel width of the silicon chip has the highest sensitivity compared to the variation of other parameters, even with the decreased values of tolerances used in silicon. Moreover, PZT length and lid height are around the value of 5, while heights of channel and chip are close to 2. In contrast, chip length, chip width, PZT height and PZT width have no significant effect on separation.

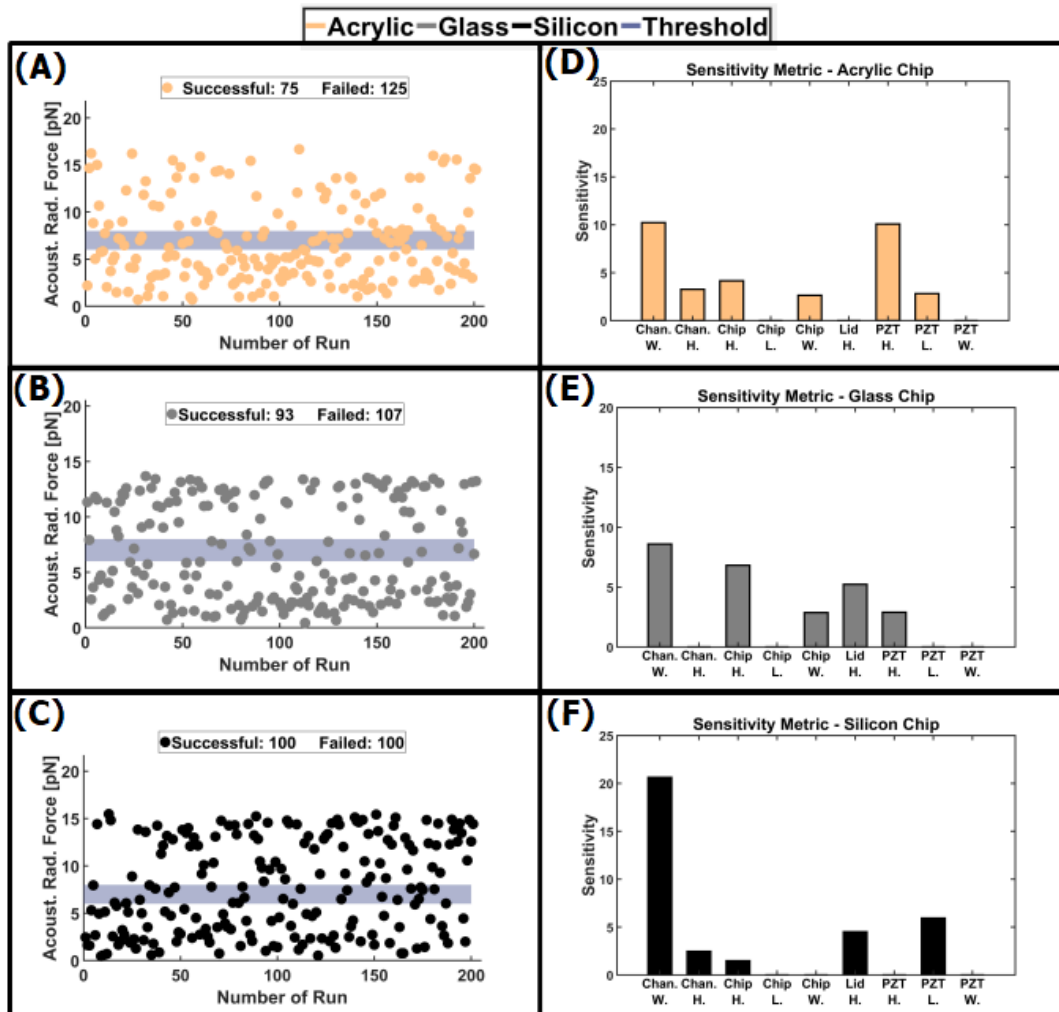


Figure 4.11 Mean acoustic radiation force and sensitivity results for three material

4.2 Effect of Assembly Error

In this section, the assembly errors that may occur in the fabrication process are investigated via numerical simulation method as explained in the previous sections. Possible five different assembly errors are assessed, which are caused by bonding processes of lid-substrate and PZT-substrate. Simulations start with the baseline scenario and 50 μm error step applied to the intended parameter until the error value reaches to 500 μm . Once simulations are completed, the mean acoustic radiation force on large particles is evaluated to show the intended parameter's effect on the separation process.

Figure 4.12 shows the effect of the lid bonding errors in x and y-direction. Acrylic is the least affected material against the errors which may occur during the bonding process; in contrast, the mean force in the glass chip dramatically decreases when placement errors occur in the y-direction. Silicon chip can tolerate one hundred micrometers shifts in both cases.

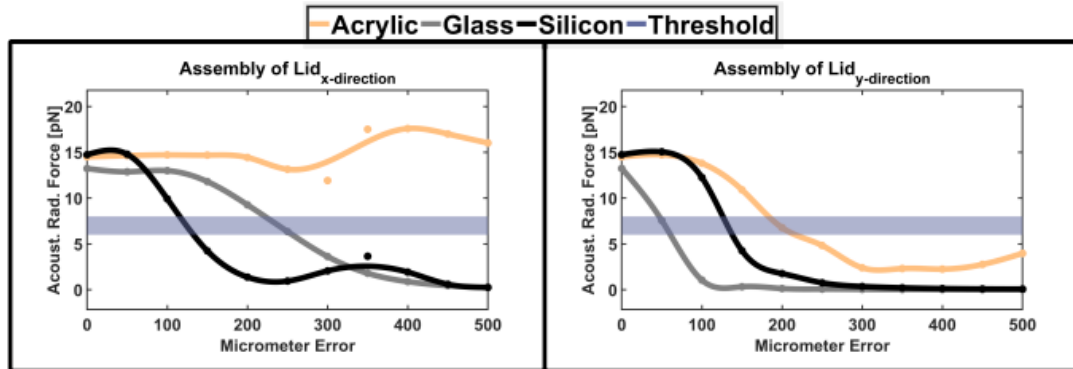


Figure 4.12 Lid-Substrate assembly errors

Graphs containing the results of the PZT assembly errors on the mean forces are presented in Figure 4.13. Silicon and acrylic chips shared a similar result for directional and rotational errors; the mean acoustic radiation force almost never fell below the threshold region for even high values of assembly errors. However, any change that disturbs the glass chip's symmetry results in a drop of the acoustic force that results in an unsuccessful separation. In particular, a dramatic sensitivity exists for glass chips when the PZT placement error in y-direction increases.

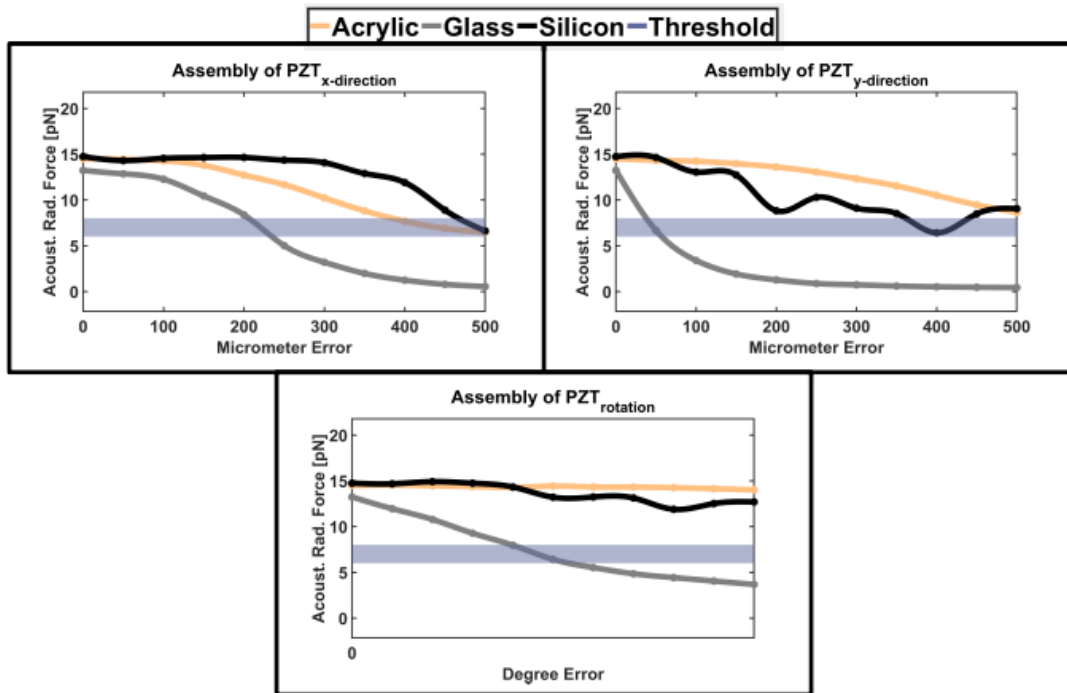


Figure 4.13 PZT-Substrate assembly errors

4.3 Variations in the Piezoelectric Actuator Placement

Reflecting the acoustic wave from the opposite wall in order to ensure the out-of-phase vibration of the walls results in a standing wave along the channel width. Most of the transverse resonators in literature asymmetrically place the actuator on the chip while the layered resonators use hard material as the reflector, which is placed opposite to the actuator wall [1]–[3]. The purpose of this section is to evaluate the separation performance of three different types of PZT placement configurations. The simulation tool, explained in previous sections, is used to identify the effect of actuator placement.

Figure 4.14 shows the symmetrical placement of the transducer's frequency response. Volume averaged force values that are calculated according to equation (2.22) are normalized with respect to the maximum value of the force components (w.r.t. 'x' or 'y' direction) for better visualization. Separation simulations run at or near the frequencies where acoustic force peaks are observed. Particle trajectory

results and three components of the pressure gradient (z-axis force components are very small) are shown in Figure 4.14. As shown in the bottom right portion of Figure 4.14, PZT is symmetrical place on the chip. This configuration resulted in a dominant pressure gradient along the x-direction (flow direction), which lead to no separation, and most of the particles got stuck in the inlet region at the resonant frequency ($\sim 705\text{kHz}$). As expected, non-resonant frequencies cannot achieve manipulation in any direction, even if at high voltage levels (150 V).

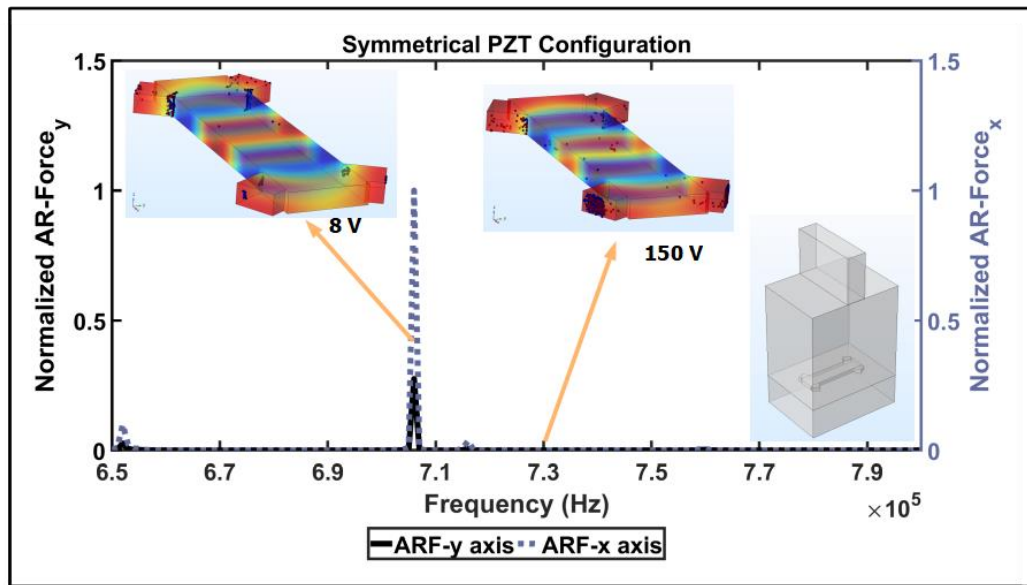


Figure 4.14 Symmetric assembly configuration of PZT

The frequency response of the asymmetrical configuration of the PZT actuator is shown in Figure 4.15. It can be seen that there is a frequency range between 690 kHz-730 kHz, which is resulting in high gradients along the x-direction; on the other hand, frequencies between 750 kHz and 800 kHz results in a dominant pressure gradient along the y-axis. According to the particle trajectory simulations shown in Figure 4.15, particles can be easily separated at resonant frequency ($\sim 765\text{kHz}$), resulting in high forces along the y-direction. The chip can also separate the particle at a frequency, $\sim 750\text{kHz}$, close to the resonant frequency of the y component with a high voltage level. However, particle manipulation in the y-direction is impossible for any frequency (resonant or non-resonant) in the region where x-component of acoustic force dominates.

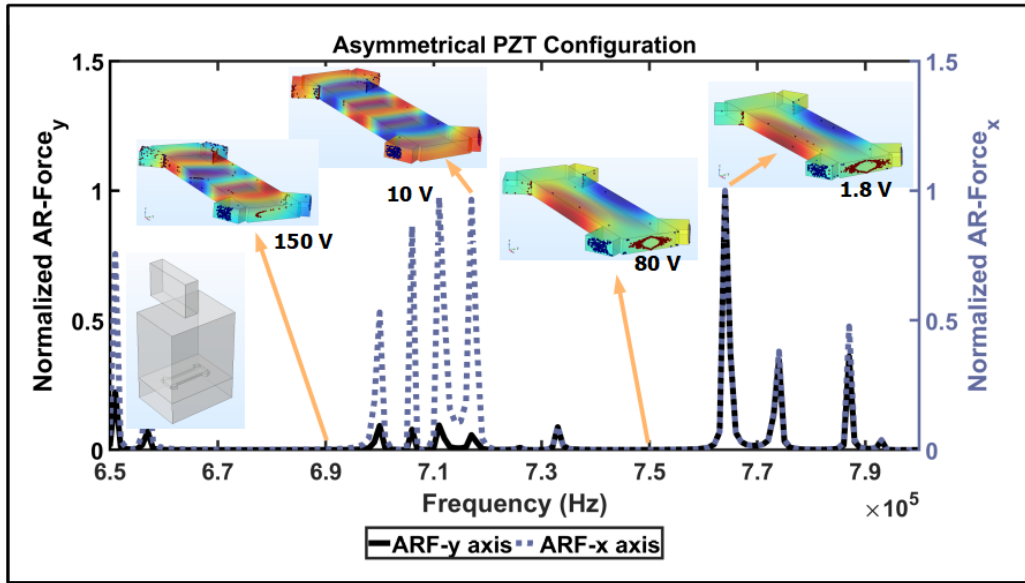


Figure 4.15 Asymmetric assembly configuration of PZT

Next, two identical PZTs are placed opposite each other and actuated out of phase, which means that one of the PZTs is contracting while the other PZT is expanding. Figure 4.16 presented the frequency response of the out-of-phase configuration of the PZTs. Out of phase actuation results in successful separation for a wide range of frequencies. Almost at all frequencies, the chip creates a pressure gradient along the y-axis, which results in successful separation. While the chip separates particles with low voltage at the resonant frequency around 760kHz, particles can also be separated at other frequencies with increased voltage levels. Figure 4.16 shows the separation at different frequencies and voltage levels.

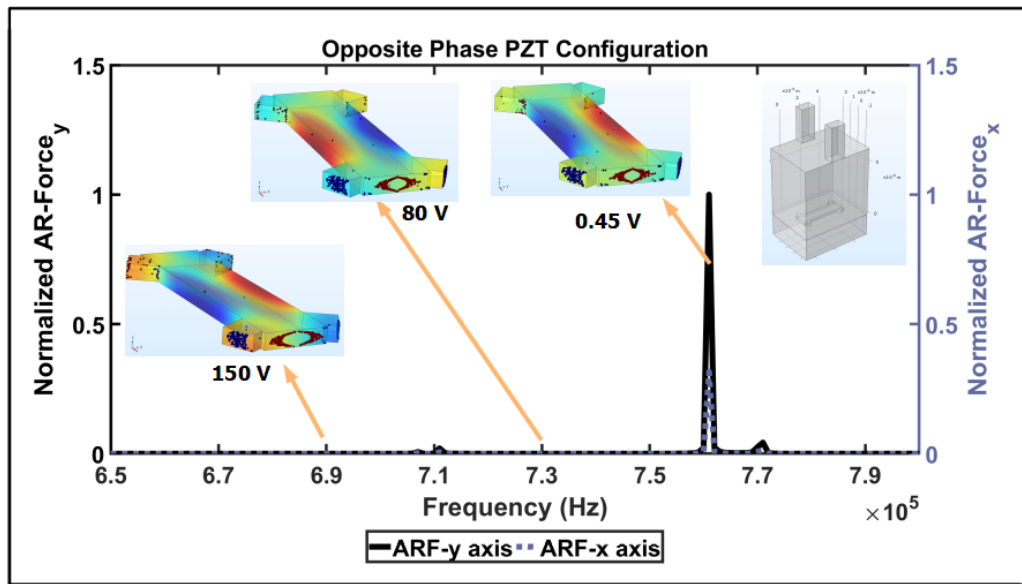


Figure 4.16 Out of phase excitation of two PZTs

4.4 Discussion of Results

The sensitivity increases while the elastic modulus of chip material increases. For instance, the channel width becomes a more important dimension for stiffer materials. Acrylic is more tolerant to dimension variations and assembly errors than the others. Another significant result from dimension variations is that the acrylic chip is independent of lid height. Channel width, chip dimensions, and PZT height are the dimensions that require more attention to be able to manufacture stable acoustofluidic devices. The opposite phase PZT actuation configuration gives a wide range of frequency that can separate particles; thus, it improves the tolerance against to the frequency shifting.

CHAPTER 5

EXPERIMENTAL STUDIES

So far, the effects of dimensional variations in different chip materials have been investigated, but the performance of different chip materials under nominal working conditions has not been investigated. In this chapter, an experimental comparison of three chips fabricated from silicon, glass, and acrylic will be performed according to their ability to concentrate 2 μm and 12 μm particles. Preparations and experiments are performed in Microfluidics & Lab-on-a-chip Research Group Laboratory of Bilkent University and Dynamics and Control Laboratory of TOBB University of Economics and Technology.

5.1.1 Fabrication of Chips

Silicon and glass are a member of the ceramic family while acrylic is polymer-based material. Thus, different techniques are required to shape those materials. While fast and simple tools such as 3D printing, laser engraving, CNC-machining can be used to manufacture polymer-based chips, etching methods are conventionally used for silicon and glass chip fabrication.

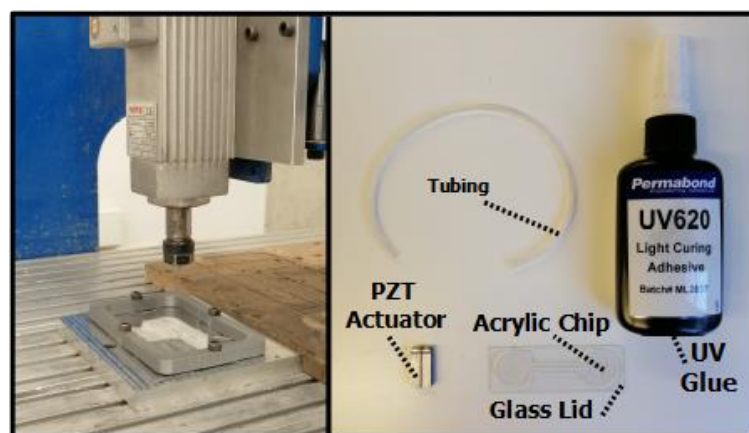


Figure 5.1 CNC Machining of acrylic chip and assembly parts

CNC-machining is selected to manufacture the acrylic acoustofluidic chip that is used in this thesis. Once the CAD model is drawn, the CAM code is generated with the HSM-Works add-on. Channel with a trifurcated design is engraved on 2.75 mm thickness acrylic with the benchtop CNC milling machine. Borosilicate glass is cut with a glasscutter such that it will enclose the entire bottom of the acrylic substrate. Glass lid is bonded to the acrylic substrate with the UV activated glue (Permabond 620). Custom manufactured PZT actuator, which is electroded in an out-of-phase configuration (Eksen İleri İmalat), is used for actuation and symmetrically bonded to the top of the substrate with cyanoacrylate-based glue (Pattex 2C Instant Glue). Standard medical tubing (PVC, 4mm outer diameter) is used for transportation of buffer and suspension and plugged into plastic tube holders (PE1000). Figure 5.1 shows the CNC machining of the acrylic plate and components that are used for assembly.

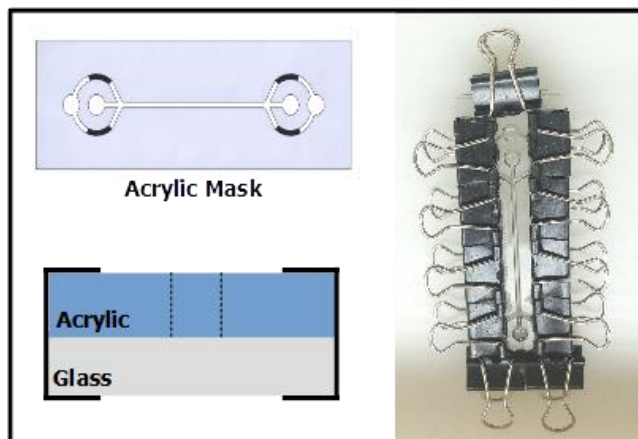


Figure 5.2 Acrylic mask for wet etching and its application

For the glass chip preparation, the wet etching method is chosen to engrave a microchannel pattern on the glass substrate. Hydrofluoric (HF) acid is used for etching. Patterned acrylic mask attached to the glass substrate, and 15M HF solution is dripped through pattern holes, as shown in Figure 5.2. After waiting for about 30 minutes, the HF is re-applied, and this process is repeated eight times. Etching of glass chip is performed in Nanocomposite and Ceramic Laboratory in TOBB ETU.

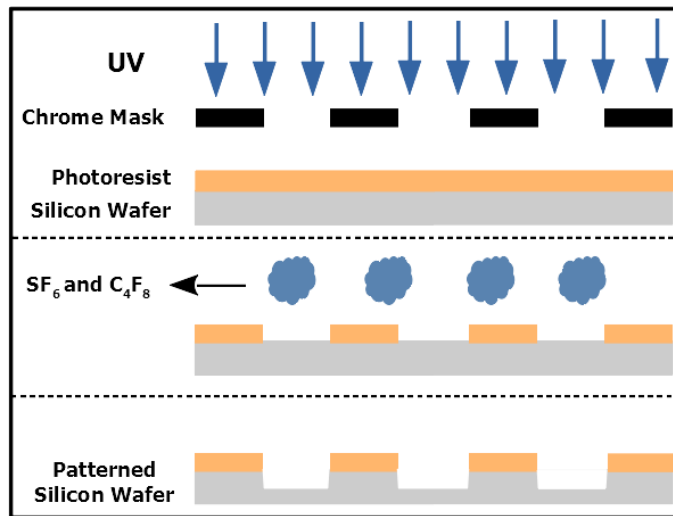


Figure 5.3 Flow of DRIE technique's steps

For the manufacturing of the silicon chip, a microchannel is engraved on a silicon wafer using a photolithography technique in the UNAM Facility at Bilkent University, and the procedure followed is shown in Figure 5.3. Chrome mask is printed according to a microchannel pattern, and the silicon wafer is covered with a positive photoresist (AZ-4562). After the positive photoresist is etched with UV light according to the chrome mask, a deep reactive ion etching (DRIE) [91] technique is used for engraving the microchannel on the silicon wafer. Tubing and bonding the PZT, the substrate, and the lid are the same procedure followed in the acrylic chip. Pictures of each acoustofluidic chip are shown in Figure 5.4.

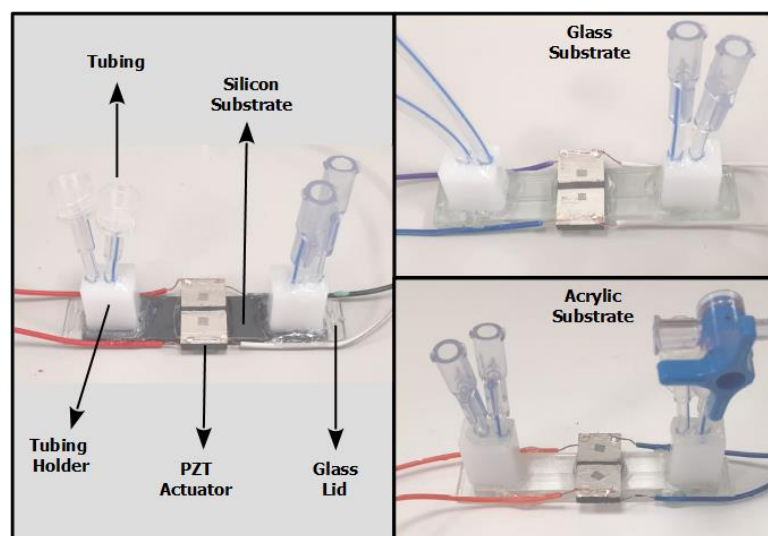


Figure 5.4 Acoustofluidic chips made of silicon, glass, and acrylic

5.1.2 Frequency Response Function (FRF) Measurements of the Chips

Once the acoustofluidic chips are fabricated, in order to assess the working frequency, the frequency response of each chip is gathered with a measurement setup that consists of a laser vibrometer (Polytec CLV-2534), signal amplifier (Falco Systems, DC -5 MHz High Voltage Amplifier, WMA-300), and digital oscilloscope (NI VirtualBench). Figure 5.5 shows setup equipment for chip vibration measurement.

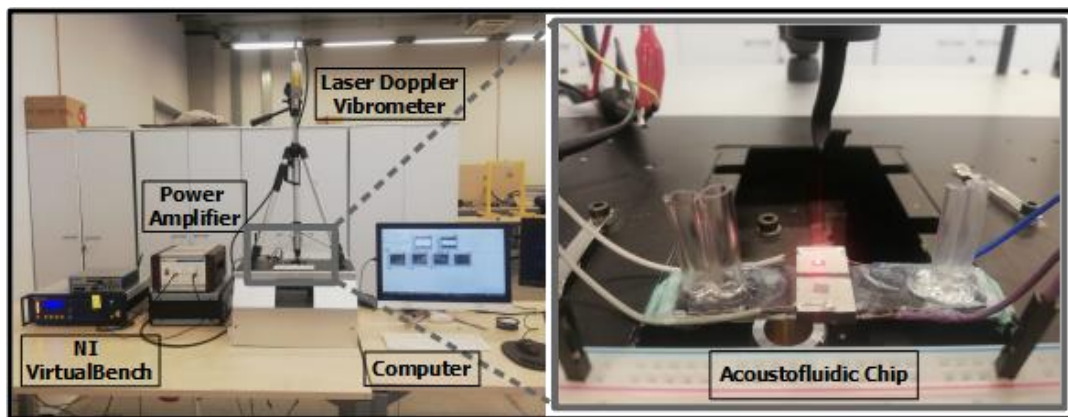


Figure 5.5 Vibration measurement setup

Vibration data are taken and transformed into the frequency domain using Fast Fourier Transform (FFT) while amplified band-limited white noise on the intended range of frequency is sent to the PZTs bonded on the acoustofluidic chip. The code that generates the FRFs is coded in LabView software (Student Edition). Figure 5.6 demonstrates the frequency response of all chips.

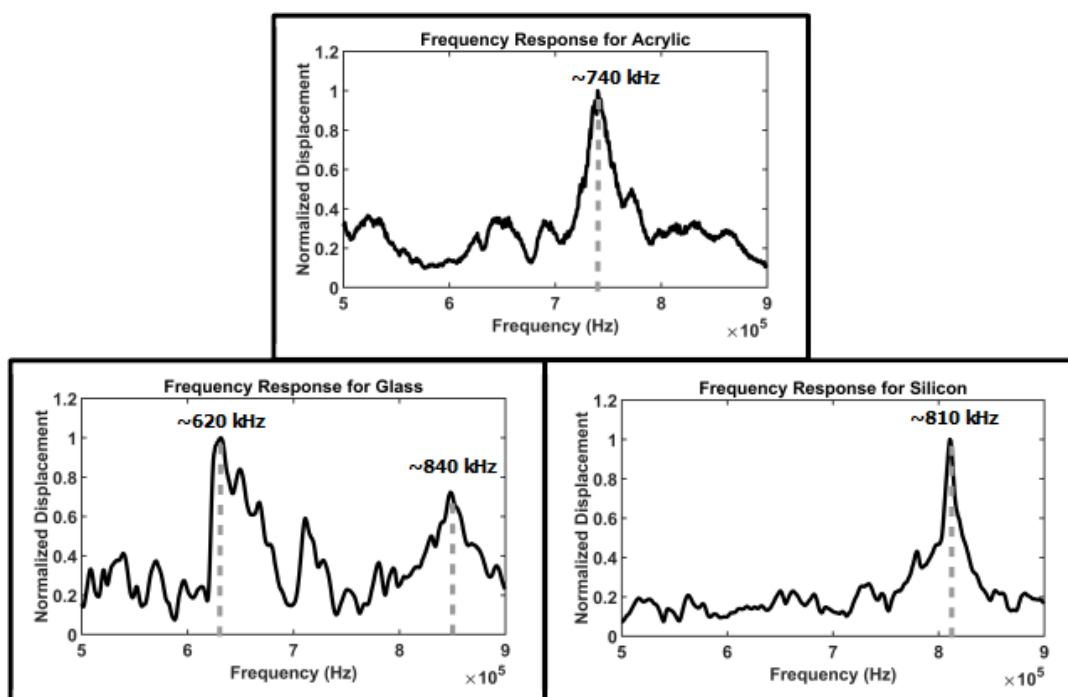


Figure 5.6 Frequency response of three chips

5.1.3 Experimental Procedure

Once the chips' operating frequencies are obtained from the frequency response measurements, the acoustofluidic chips are ready for microparticle focusing. The experimental setup is shown in Figure 5.7.

A voltage amplifier (Falco Systems, WMA-300) is used to amplify signals generated by the signal generator (GWINSTEK, SFG-2004). The amplified signal is fed to the actuator. An oscilloscope (Keysight Technologies, DSO-X 2012) is used to monitor the voltage level for signal amplitude adjustments. The thermal camera (FLIR A300) continuously records the chip's temperature and the piezoelectric actuators to protect over-heating, which may cause bubbles inside the channel.

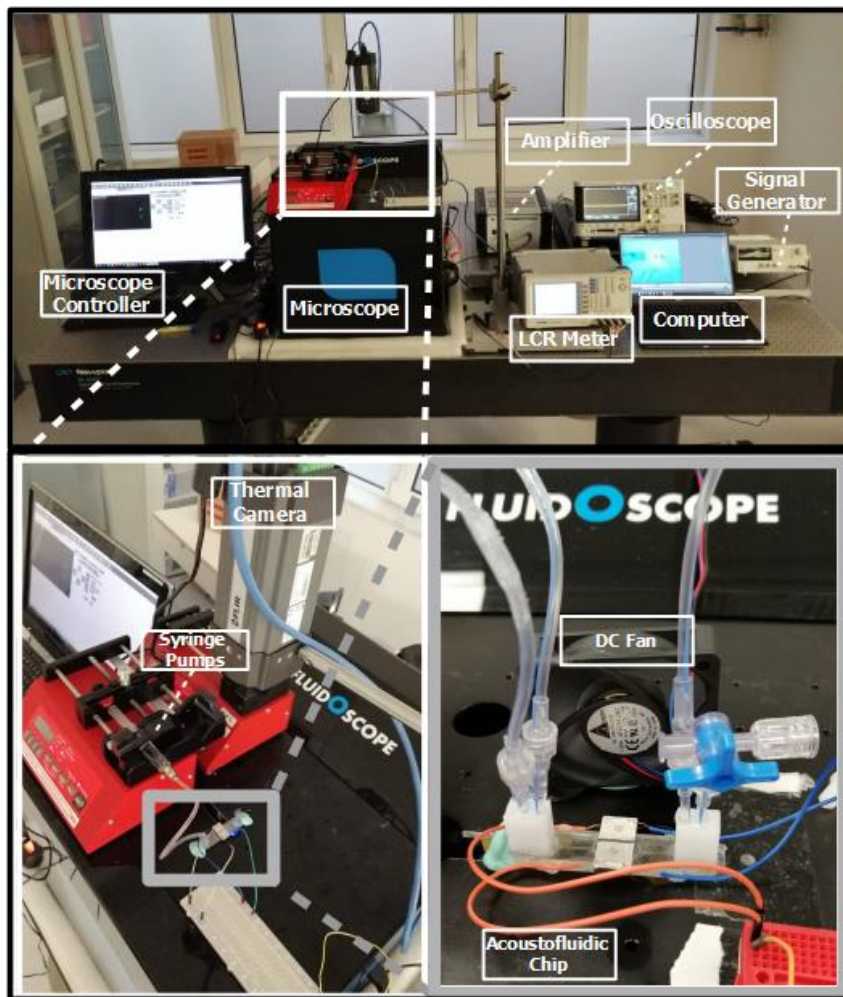


Figure 5.7 Experimental setup for particle focusing

Microchannel and particles are screened by 4x and 10x objectives under a fluorescent light microscope shown in Figure 5.8. The microscope is MIT-inv, AIV Labs, PSARON controlled by PSARON 2019 software. The PZT's impedance value around resonance frequencies is recorded by LCR Meter (GWINSTEK, LCR-8105G) to detect any shifts in the value of the resonance frequency.

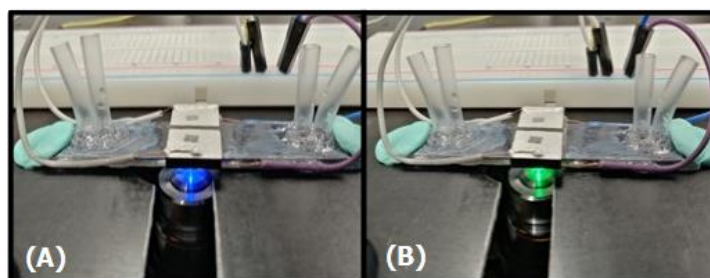


Figure 5.8 Inverted Microscope and fluorescein lights for (A) red and (B) green-dyed particles

Solutions for 2 μm (ThermoScientific, Fluoromax R0200 Red Particles) and 12 μm (ThermoScientific, Fluoromax 35-B Green Particles) are prepared such that concentration was in the range of around 10^8 particles/mL to avoid aggregation. Side inlets are closed in focusing experiments as shown in Figure 5.9 while two Syringe pumps (New Era Pump Systems-NE 300) plugged into outlet connections withdraw the particle solution from a reservoir that is connected to the main inlet. Total flow rates are 40 $\mu\text{L}/\text{min}$ and 10 $\mu\text{L}/\text{min}$ for 12 μm and 2 μm particle focusing, respectively.

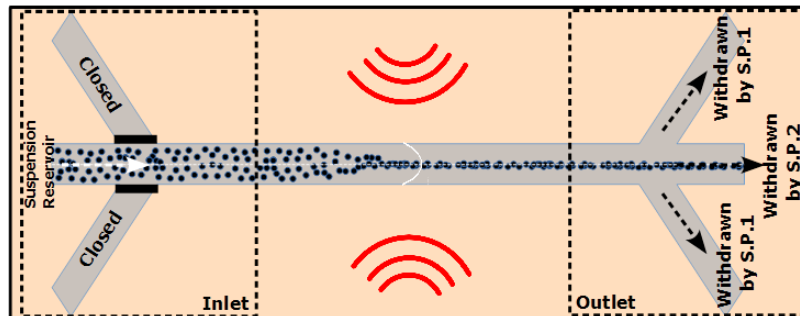


Figure 5.9 Flow design of focusing experiment (S.P. = Syringe Pump)

The experiment procedure is the same for two cases of 2 μm and 12 μm particles focusing. The PZT is turned on when the suspension fluid flows, and a steady flow regime is observed. The first data is recorded when the first visible motion of particles towards the channel's center is observed. The PZT actuator's voltage is increased with steps of five or ten volts until the focused width of the particles is no longer decreasing. At least 200 images are taken and recorded to be processed and stacked in PICOLAY Software, and temperature values are also recorded in each test.

5.2 Results

Images taken during the experiment are processed using the image stacking procedure for improved visualization and better focus width measurements. Figure 5.10 shows the results of three acoustofluidic chips at each voltage step. The acrylic chip starts to focus 12 μm particles at 40 Volts, which corresponds to a focusing width of nearly 540 μm . Focusing width decreases for each voltage increment, and it converges to 205 μm value at 75 Volts beyond which overheating occurs, and no more decrease in focus width is observed. On the other hand, the glass chip starts to focus particles at 15 Volts, which corresponds to nearly 630 μm focus width. The focus width gets narrower as the voltage increases until 50 Volts, which results in a focus width around 65 μm . The first data for silicon chip is taken at 15 Volts, around 750 μm . The focusing width dramatically decreases when the voltage level increases and converges its minimum value of 40 μm at 40 Volts. No critical changes are observed for the temperature of both chips.

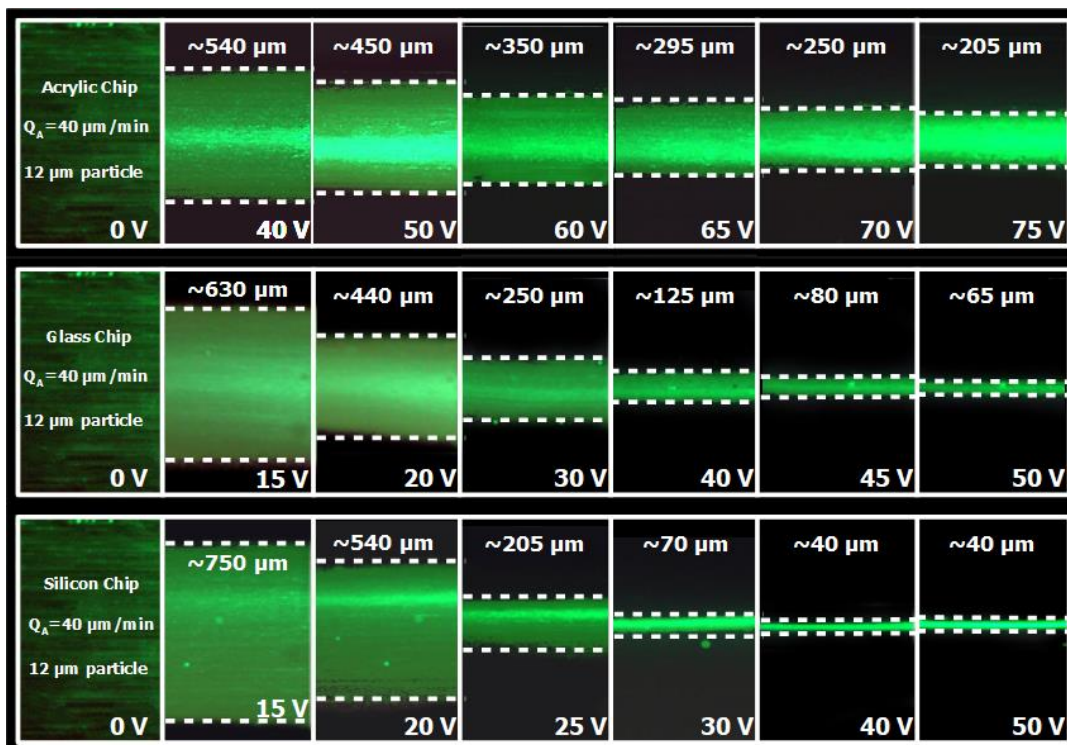


Figure 5.10 12 μm particle focusing results for three chips

Unlike the focusing of 12 μm particles, only two of three chips could achieve the task of focusing for 2 μm particles. Even though high voltage values are fed on actuators, acoustic streamings are started to dominate particle motions instead of the acoustic radiation force in the acrylic chip. Figure 5.11 displays the results of the silicon and glass chip performance on 2 μm particle focusing. As expected, the voltage required to start the focusing of 2 μm is higher than the voltage value for 12 μm . At 60 Volts, the glass chip's focusing width is around 170 μm while the silicon chip's focusing width is around 250 μm . Both chips focused particles on a narrower area as the voltage applied to the actuator increases. However, at 90 Volts, the silicon chip ends with a 30 μm focusing width, whereas the glass chip converges to 60 μm width.

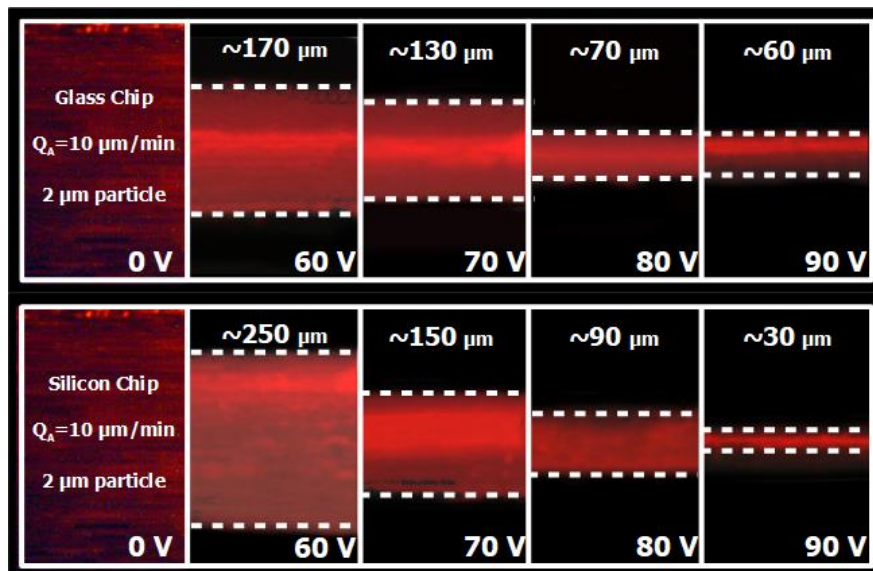


Figure 5.11 2 μm particle focusing results for two chips

5.3 Discussion of Results

The concentration of two different size particles is performed in three chips made of different substrate materials. Even though the acrylic chip can achieve the focusing of 12 μm particles, the focusing of 2 μm particles is not accomplished for this chip material. Silicon and glass give more efficient and narrower focusing results than the

acrylic chip. Although the silicon chip can reach its minimum focusing width for 12 μm particle at lower voltages, the glass chip performance is similar to the silicon chip. However, the glass chip could not achieve a value lower than 60 μm while the minimum silicon chip's focusing width of 2 μm particles is 30 μm at 90 Volts.

CHAPTER 6

CONCLUSIONS

In Chapter 3, a numerical simulation method coupled with electro-mechanic, structural, and acoustical domains is created to evaluate acoustofluidic chips in terms of their separation performances. Acoustophoretic and drag force components, fluid flow velocities, and each particle's trajectory are calculated and used to evaluate performance metrics. This methodology can further analyze acoustofluidic chips in terms of optimization or sensitivity analysis of all geometric components or operating parameters.

[Case 2](#) and [Case 6](#) indicate that narrower channel width corresponds to higher frequencies, which gives better separation performance (high purity and yield, low number of stuck particles) than the chips with wider widths. Furthermore, the number of stuck particles inside the channel increases while the channel width gets wider.

[Case 3](#) shows that separation is possible if out-of-phase excitation is applied to microchannel walls even though the excitation frequency is not arranged to fit half wavelength of the acoustic wave inside the channel. On the other hand, if the difference between half of the acoustic pressure wavelength and channel width increases, the required voltage to create sufficient acoustic pressure inside the channel becomes too high. Heating problems faced in experiments demonstrate that frequency selection should conform with the channel width (commonly applied in literature) even though the separation is theoretically possible at every frequency.

[Case 4](#) demonstrates that the chip with lower channel depth causes a challenge in separation due to the high fluid flow and particle velocities. Particles with high velocities inside the channel require more acoustic force to move, resulting in a high voltage value on the actuator. On the other hand, the high acoustic force causes particles to get stuck at the microchannel's inlet side. Case 4 also shows that if the

channel height gets deeper and closes to a value comparable with acoustic pressure wavelength, an acoustic pressure gradient occurs in the direction of height. While the channel height increases, the difference of particle velocities that flow at different heights increases. High-velocity gradient results in particles exiting through an unintended outlet.

[Case 5](#) shows that the purity and yield values improve when the ratio of the main flow to side flow increases until the high velocities of the flow deteriorate the separation. High velocities require more voltages on actuators for separation. Although the pushing particle close to the sidewall improves the separation performance, high acoustic force requirement due to high velocities causes more particles to get stuck on walls.

[Case 6](#) demonstrates that if particle diameters get closer to each other, separation is significantly affected. [Case 7](#) shows that an improvement can be obtained by narrowing the particle release position over the cross-section. The confined release method helps to separate particles with a high-efficiency. A similar approach is stated in literature [52], which states that pre-alignment of particles before the separation region improves the separation efficiency. Moreover, the size distribution of small and large particles affects the separation performance, as shown in Case 7. Particles having a size distribution resulted in a decreased separation performance in quarter-width and quarter-depth configurations. However, limiting the release region in both depth and width direction results in perfect separation even if particles have size distribution. These results show that the acoustophoretic chips may have high selectivity for separation with the right enhancements.

Chapter 4 uses the simulation method coupled with solid-acoustic-electrical domains and includes the flow, particle trajectory, and mean force calculations used to understand the effect of variations in chip dimensions, assembly errors, and PZT configurations for the separation of 5 μm and 15 μm particles from each other.

The most extraordinary change occurs in channel width variations of silicon and glass chips, while the chip separation is barely affected by PZT width and PZT length

in contrast to PZT height. Therefore, the channel width is a dimension on which more attention should be given to fabricate stable acoustofluidic devices.

Except for the variation on PZT height, acrylic chip gives better results than the glass, and silicon chips, as shown in Figure 4.3, Figure 4.4, and Figure 4.5. One of the significant benefits of using acrylic as the chip material is the independence of acrylic chip performance from the lid height. Other materials seem to be sensitive to the glass lid height. Lid height independent acrylic chips also show a similar characteristic in bonding errors between substrate and lid. Acrylic is the least affected material against the lid assembly errors.

Chip height results in Sections 4.1 and 4.1.1 indicate that the glass chip is more sensitive to chip height dimension variations than the others. The use of the same material for substrate and the lid components causes glass chips to be more sensitive to the chip height and the lid height. If the glass is selected as a substrate, more attention is required for the chip heights and channel width. Moreover, the glass chip reaction against the lid slipping is also considerable. Any attempt that destroys the glass chip's x-axis symmetry creates a dramatic change in terms of the acoustic radiation force.

In case of any shifted frequency, the asymmetrical configuration cannot separate particles in a wide range of frequency, and the frequency should be adjusted carefully and tuned to the correct group of the peak points that creates the acoustic force along the y-axis. However, the opposite phase configuration can theoretically separate particles in a wide frequency range requiring high voltage levels. (refer to Figure 4.15 and Figure 4.16)

In Chapter 5, an experimental investigation of different size particles' focusing is conducted for three chips made of acrylic, glass, and silicon. For 12 μm particle focusing, acrylic chip accomplishes at best a minimum focusing width of around 200 μm at 75 Volts while 40 Volts are sufficient to focus particles with a width of less than 150 μm in silicon and glass chips. Silicon chip shows slightly better performance than the glass chip and demonstrates a dramatic response with each

increment of voltage. It reaches its minimum value of the focus width of 40 μm , at 40 Volts, while the glass chip can achieve at most 65 μm the focus width at 50 Volts. On the other hand, a much more challenging task of 2 μm particle focusing indicates that acoustic streaming should be considered in the case of low acoustic radiation. Acoustic radiation force that the particles are exposed to decreases with the cube of particle diameter as the particles get smaller. Thus, the problem of acoustic streaming starts to dominate particle motion. Although acrylic is more tolerant to variations and errors, as shown in Chapter 4, a low Q (quality factor) material acrylic cannot produce sufficient force for smaller particles, such as a few microns and sub-micron. Therefore, acoustic streaming should be considered for low-Q devices; it should be remembered that acoustic streaming manipulates the particle trajectories for small diameter particles [6], [92], [93]. In contrast to acrylic, silicon and glass chips can concentrate the 2 μm particles on the channel's center. Silicon gives a narrower minimum focusing width than the glass at the same voltage level of 90 Volts.

REFERENCES

- [1] N. R. Harris *et al.*, “A silicon microfluidic ultrasonic separator,” *Sensors Actuators, B Chem.*, vol. 95, no. 1–3, pp. 425–434, 2003.
- [2] J. J. Hawkes, R. W. Barber, D. R. Emerson, and W. T. Coakley, “Continuous cell washing and mixing driven by an ultrasound standing wave within a microfluidic channel,” *Lab Chip*, vol. 4, no. 5, pp. 446–452, 2004.
- [3] A. Nilsson, F. Petersson, H. Jönsson, and T. Laurell, “Acoustic control of suspended particles in micro fluidic chips,” *Lab Chip*, vol. 4, no. 2, pp. 131–135, 2004.
- [4] A. Neild, S. Oberti, and J. Dual, “Design, modeling and characterization of microfluidic devices for ultrasonic manipulation,” *Sensors Actuators, B Chem.*, vol. 121, no. 2, pp. 452–461, 2007.
- [5] A. Lenshof *et al.*, “Efficient purification of CD4⁺ lymphocytes from peripheral blood progenitor cell products using affinity bead acoustophoresis,” *Cytom. Part A*, vol. 85, no. 11, pp. 933–941, 2014.
- [6] D. Van Assche *et al.*, “Gradient acoustic focusing of sub-micron particles for separation of bacteria from blood lysate,” *Sci. Rep.*, vol. 10, no. 1, pp. 1–13, 2020.
- [7] T. Laurell, S. Lee, J. Park, S. Ren, S. J. Lee, and S. Kim, “Acousto-microfluidics for screening of ssDNA aptamer,” *Sci. Rep.*, vol. 6, no. 1, pp. 1–9, 2016.
- [8] Y. Chen *et al.*, “High-throughput acoustic separation of platelets from whole blood,” *Lab Chip*, vol. 16, no. 18, pp. 3466–3472, 2016.
- [9] C. Grenvall, J. R. Folkenberg, P. Augustsson, and T. Laurell, “Label-free somatic cell cytometry in raw milk using acoustophoresis,” *Cytom. Part A*, vol. 81 A, no. 12, pp. 1076–1083, 2012.

- [10] C. Grenvall, P. Augustsson, J. R. Folkenberg, and T. Laurell, “Harmonic microchip acoustophoresis: A route to online raw milk sample precondition in protein and lipid content quality control,” *Anal. Chem.*, vol. 81, no. 15, pp. 6195–6200, 2009.
- [11] C. Lissandrello, R. Dubay, K. T. Kotz, and J. Fiering, “Purification of Lymphocytes by Acoustic Separation in Plastic Microchannels,” *SLAS Technol.*, vol. 23, no. 4, pp. 352–363, 2018.
- [12] A. Carrato *et al.*, “A Label Free Disposable Device for Rapid Isolation of Rare Tumor Cells from Blood by Ultrasounds,” *Micromachines*, vol. 9, no. 3, p. 129, 2018.
- [13] S. Karthick, P. N. Pradeep, P. Kanchana, and A. K. Sen, “Acoustic impedance-based size-independent isolation of circulating tumour cells from blood using acoustophoresis,” *Lab Chip*, vol. 18, no. 24, pp. 3802–3813, 2018.
- [14] C. Samarasekera, J. G. W. Sun, Z. Zheng, and J. T. W. Yeow, “Trapping, separating, and palpating microbead clusters in droplets and flows using capacitive micromachined ultrasonic transducers (CMUTs),” *Sensors Actuators, B Chem.*, vol. 276, no. March, pp. 481–488, 2018.
- [15] C. Magnusson, P. Augustsson, A. Lenshof, Y. Ceder, T. Laurell, and H. Lilja, “Clinical-Scale Cell-Surface-Marker Independent Acoustic Microfluidic Enrichment of Tumor Cells from Blood,” *Anal. Chem.*, vol. 89, no. 22, pp. 11954–11961, 2017.
- [16] T. Laurell, A. Lenshof, F. Garofalo, A. Urbansky, S. Scheduling, and P. Ohlsson, “Rapid and effective enrichment of mononuclear cells from blood using acoustophoresis,” *Sci. Rep.*, vol. 7, no. 1, pp. 1–9, 2017.
- [17] D. Densmore *et al.*, “Rapid prototyping and parametric optimization of plastic acoustofluidic devices for blood–bacteria separation,” *Biomed. Microdevices*, vol. 19, no. 3, 2017.

- [18] P. Ohlsson *et al.*, “Integrated Acoustic Separation, Enrichment, and Microchip Polymerase Chain Reaction Detection of Bacteria from Blood for Rapid Sepsis Diagnostics,” *Anal. Chem.*, vol. 88, no. 19, pp. 9403–9411, 2016.
- [19] B. Çetin, M. B. Özer, E. Çağatay, and S. Büyükoçak, “An integrated acoustic and dielectrophoretic particle manipulation in a microfluidic device for particle wash and separation fabricated by mechanical machining,” *Biomicrofluidics*, vol. 10, no. 1, 2016.
- [20] K. Goda *et al.*, “Acoustofluidic harvesting of microalgae on a single chip,” *Biomicrofluidics*, vol. 10, no. 3, p. 034119, 2016.
- [21] G. P. Gautam, R. Gurung, F. A. Fencel, and M. E. Piyasena, “Separation of sub-micron particles from micron particles using acoustic fluid relocation combined with acoustophoresis,” *Anal. Bioanal. Chem.*, vol. 410, no. 25, pp. 6561–6571, 2018.
- [22] J. J. Hawkes and W. T. Coakley, “A continuous flow ultrasonic cell-filtering method,” *Enzyme Microb. Technol.*, vol. 19, no. 1, pp. 57–62, 1996.
- [23] F. Petersson, L. Åberg, A. M. Swärd-Nilsson, and T. Laurell, “Free flow acoustophoresis: Microfluidic-based mode of particle and cell separation,” *Anal. Chem.*, vol. 79, no. 14, pp. 5117–5123, 2007.
- [24] O. Manneberg, B. Vanherberghen, B. Önfelt, and M. Wiklund, “Flow-free transport of cells in microchannels by frequency-modulated ultrasound,” *Lab Chip*, vol. 9, no. 6, pp. 833–837, 2009.
- [25] M. Nordin and T. Laurell, “Two-hundredfold volume concentration of dilute cell and particle suspensions using chip integrated multistage acoustophoresis,” *Lab Chip*, vol. 12, no. 22, pp. 4610–4616, 2012.
- [26] H. Wang *et al.*, “Microfluidic acoustophoretic force based low-concentration oil separation and detection from the environment,” *Lab Chip*, vol. 14, no. 5,

pp. 947–956, 2014.

- [27] B. Hammarström, M. Evander, J. Wahlström, and J. Nilsson, “Frequency tracking in acoustic trapping for improved performance stability and system surveillance,” *Lab Chip*, vol. 14, no. 5, pp. 1005–1013, 2014.
- [28] M. Antfolk, C. Magnusson, P. Augustsson, H. Lilja, and T. Laurell, “Acoustofluidic, Label-Free Separation and Simultaneous Concentration of Rare Tumor Cells from White Blood Cells,” *Anal. Chem.*, vol. 87, no. 18, pp. 9322–9328, 2015.
- [29] Torben Rees, “Ernst Chladni: physicist, musician and musical instrument maker,” 2009. [Online]. Available: <https://www.whipplemuseum.cam.ac.uk/explore-whipple-collections/acoustics/ernst-chladni-physicist-musician-and-musical-instrument-maker>. [Accessed: 19-Dec-2020].
- [30] I. R. L. UCLA Physics & Astronomy, “Kundt’s Tube Experiment.” [Online]. Available: <http://demoweb.physics.ucla.edu/content/100-kundts-tube>. [Accessed: 14-Dec-2020].
- [31] L. V King and P. R. S. L. A, “On the acoustic radiation pressure on spheres,” *Proc. R. Soc. London. Ser. A - Math. Phys. Sci.*, vol. 147, no. 861, pp. 212–240, 1934.
- [32] K. Yosioka and Y. Kawasima, “Acoustic radiation pressure on a compressible sphere,” *Acta Acust. united with Acust.*, vol. 5, no. 3, pp. 167–173, 1955.
- [33] B. Y. K. Sollner, “The mechanism of the formation of fogs by ultrasonic waves,” *Trans. Faraday Soc.*, vol. 36, pp. 1532–1536, 1936.
- [34] M. Settnes and H. Bruus, “Forces acting on a small particle in an acoustical field in a viscous fluid,” *Phys. Rev. E - Stat. Nonlinear, Soft Matter Phys.*, vol. 85, no. 1, pp. 1–12, 2012.
- [35] S. C. S. Lin, X. Mao, and T. J. Huang, “Surface acoustic wave (SAW)

- acoustophoresis: Now and beyond,” *Lab Chip*, vol. 12, no. 16, pp. 2766–2770, 2012.
- [36] L. Johansson, J. Enlund, S. Johansson, I. Katardjiev, M. Wiklund, and V. Yantchev, “Surface acoustic wave-induced precise particle manipulation in a trapezoidal glass microfluidic channel,” *J. Micromechanics Microengineering*, vol. 22, no. 2, 2012.
- [37] J. Shi, H. Huang, Z. Stratton, Y. Huang, and T. J. Huang, “Continuous particle separation in a microfluidic channel via standing surface acoustic waves (SSAW),” *Lab Chip*, vol. 9, no. 23, pp. 3354–3359, 2009.
- [38] K. Yasuda, S. I. Umemura, and K. Takeda, “Concentration and fractionation of small particles in liquid by ultrasound,” *Jpn. J. Appl. Phys.*, vol. 34, no. 5S, pp. 2715–2720, 1995.
- [39] Z. I. Mandralis and D. L. Feke, “Continuous suspension fractionation using acoustic and divided-flow fields,” *Chem. Eng. Sci.*, vol. 48, no. 23, pp. 3897–3905, 1993.
- [40] M. Groschl, “Ultrasonic Separation of Suspended Particles - Part I: Fundamentals,” *Acustica*, vol. 84, no. October 1997, pp. 432–447, 1998.
- [41] H. Bruus, A. H. J. Yang, R. Barnkob, H. T. Soh, J. D. Adams, and C. L. Ebbesen, “High-throughput, temperature-controlled microchannel acoustophoresis device made with rapid prototyping,” *J. Micromechanics Microengineering*, vol. 22, no. 7, p. 075017, 2012.
- [42] M. Dyson, B. Woodward, and J. B. Pond, “Flow of red blood cells stopped by ultrasound,” *Nature*, vol. 232, no. 5312, pp. 572–573, 1971.
- [43] N. V. Baker, “Segregation and sedimentation of red blood cells in ultrasonic standing waves,” *Nat. new Biol.*, vol. 239, pp. 398–399, 1972.
- [44] J. J. Hawkes *et al.*, “Single half-wavelength ultrasonic particle filter: Predictions of the transfer matrix multilayer resonator model and

- experimental filtration results,” *J. Acoust. Soc. Am.*, vol. 111, no. 3, pp. 1259–1266, 2002.
- [45] D. Carugo *et al.*, “A thin-reflector microfluidic resonator for continuous-flow concentration of microorganisms: A new approach to water quality analysis using acoustofluidics,” *Lab Chip*, vol. 14, no. 19, pp. 3830–3842, 2014.
- [46] H. Jönsson, C. Holm, A. Nilsson, F. Petersson, P. Johnsson, and T. Laurell, “Particle separation using ultrasound can radically reduce embolic load to brain after cardiac surgery,” *Ann. Thorac. Surg.*, vol. 78, no. 5, pp. 1572–1577, 2004.
- [47] J. Dykes, A. Lenshof, I. B. Åstrand-Grundström, T. Laurell, and S. Scheduling, “Efficient removal of platelets from peripheral blood progenitor cell products using a novel micro-chip based acoustophoretic platform,” *PLoS One*, vol. 6, no. 8, 2011.
- [48] A. Urbansky, A. Lenshof, J. Dykes, T. Laurell, and S. Scheduling, “Affinity-bead-mediated enrichment of CD8+ lymphocytes from peripheral blood progenitor cell products using acoustophoresis,” *Micromachines*, vol. 7, no. 6, pp. 1–13, 2016.
- [49] K. Järås *et al.*, “Acoustic Whole Blood Plasmapheresis Chip for Prostate Specific Antigen Microarray Diagnostics,” *Anal. Chem.*, vol. 81, no. 15, pp. 6030–6037, 2009.
- [50] A. A. Tajudin *et al.*, “Integrated acoustic immunoaffinity-capture (IAI) platform for detection of PSA from whole blood samples,” *Lab Chip*, vol. 13, no. 9, pp. 1790–1796, 2013.
- [51] A. H. J. Yang and H. T. Soh, “Acoustophoretic sorting of viable mammalian cells in a microfluidic device,” *Anal. Chem.*, vol. 84, no. 24, pp. 10756–10762, 2012.
- [52] P. Augustsson, C. Magnusson, M. Nordin, H. Lilja, and T. Laurell,

- “Microfluidic, label-free enrichment of prostate cancer cells in blood based on acoustophoresis,” *Anal. Chem.*, vol. 84, no. 18, pp. 7954–7962, 2012.
- [53] P. Ohlsson, K. Petersson, P. Augustsson, and T. Laurell, “Acoustic impedance matched buffers enable separation of bacteria from blood cells at high cell concentrations,” *Sci. Rep.*, vol. 8, no. 1, pp. 1–11, 2018.
- [54] A. Mueller, A. Lever, T. V. Nguyen, J. Comolli, and J. Fiering, “Continuous acoustic separation in a thermoplastic microchannel,” *J. Micromechanics Microengineering*, vol. 23, no. 12, 2013.
- [55] P. Dow, K. Kotz, S. Gruszka, J. Holder, and J. Fiering, “Acoustic separation in plastic microfluidics for rapid detection of bacteria in blood using engineered bacteriophage,” *Lab Chip*, vol. 18, no. 6, pp. 923–932, 2018.
- [56] M. Evander, A. Lenshof, T. Laurell, and J. Nilsson, “Acoustophoresis in wet-etched glass chips,” *Anal. Chem.*, vol. 80, no. 13, pp. 5178–5185, 2008.
- [57] Z. Wu *et al.*, “The acoustofluidic focusing and separation of rare tumor cells using transparent lithium niobate transducers,” *Lab Chip*, vol. 19, no. 23, pp. 3922–3930, 2019.
- [58] P. B. Muller *et al.*, “Ultrasound-induced acoustophoretic motion of microparticles in three dimensions,” *Phys. Rev. E - Stat. Nonlinear, Soft Matter Phys.*, vol. 88, no. 2, pp. 1–12, 2013.
- [59] P. B. Muller and H. Bruus, “Theoretical study of time-dependent, ultrasound-induced acoustic streaming in microchannels,” *Phys. Rev. E - Stat. Nonlinear, Soft Matter Phys.*, vol. 92, no. 6, pp. 1–13, 2015.
- [60] P. B. Muller and H. Bruus, “Numerical study of thermoviscous effects in ultrasound-induced acoustic streaming in microchannels,” *Phys. Rev. E - Stat. Nonlinear, Soft Matter Phys.*, vol. 90, no. 4, pp. 1–12, 2014.
- [61] F. Garofalo, “Quantifying Acoustophoretic Separation of Microparticle Populations by Mean-and-Covariance Dynamics for Gaussians in Mixture

Models,” pp. 1–15, 2018.

- [62] V. Vitali, T. Yang, and P. Minzioni, “Separation efficiency maximization in acoustofluidic systems: Study of the sample launch-position,” *RSC Adv.*, vol. 8, no. 68, pp. 38955–38964, 2018.
- [63] F. Garofalo, T. Laurell, and H. Bruus, “Performance Study of Acoustophoretic Microfluidic Silicon-Glass Devices by Characterization of Material- and Geometry-Dependent Frequency Spectra,” *Phys. Rev. Appl.*, vol. 7, no. 5, pp. 1–16, 2017.
- [64] R. P. Moiseyenko and H. Bruus, “Whole-System Ultrasound Resonances as the Basis for Acoustophoresis in All-Polymer Microfluidic Devices,” *Phys. Rev. Appl.*, vol. 11, no. 1, p. 1, 2019.
- [65] P. Hahn, O. Schwab, and J. Dual, “Modeling and optimization of acoustofluidic micro-devices,” *Lab Chip*, vol. 14, no. 20, pp. 3937–3948, 2014.
- [66] S. Büyükkoçak, M. B. Özer, and B. Çetin, “Numerical modeling of ultrasonic particle manipulation for microfluidic applications,” *Microfluid. Nanofluidics*, vol. 17, no. 6, pp. 1025–1037, 2014.
- [67] M. A. Şahin, B. Çetin, and M. B. Özer, “Investigation of effect of design and operating parameters on acoustophoretic particle separation via 3D device-level simulations,” *Microfluid. Nanofluidics*, vol. 24, no. 1, 2020.
- [68] Y. Tong *et al.*, “Additive manufacturing of three-dimensional (3D) microfluidic-based microelectromechanical systems (MEMS) for acoustofluidic applications,” *Lab Chip*, vol. 18, no. 14, pp. 2087–2098, 2018.
- [69] J. Dual, P. Hahn, I. Leibacher, D. Möller, and T. Schwarz, “Acoustofluidics 6: Experimental characterization of ultrasonic particle manipulation devices,” *Lab Chip*, vol. 12, no. 5, pp. 852–862, 2012.
- [70] D. M. Kalb, R. J. Olson, H. M. Sosik, T. A. Woods, and S. W. Graves,

- “Resonance control of acoustic focusing systems through an environmental reference table and impedance spectroscopy,” *PLoS One*, vol. 13, no. 11, pp. 1–20, 2018.
- [71] V. Vitali, G. Core, F. Garofalo, T. Laurell, and A. Lenshof, “Differential impedance spectra analysis reveals optimal actuation frequency in bulk mode acoustophoresis,” *Sci. Rep.*, vol. 9, no. 1, pp. 1–10, 2019.
- [72] A. Wilcox, T. Burger, M. E. Piyasena, S. W. Graves, G. P. Gautam, and M. J. Cumbo, “Simple and inexpensive micromachined aluminum microfluidic devices for acoustic focusing of particles and cells,” *Anal. Bioanal. Chem.*, vol. 410, no. 14, pp. 3385–3394, 2018.
- [73] H. Bruus, “Acoustofluidics 7: The acoustic radiation force on small particles,” *Lab Chip*, vol. 12, no. 6, pp. 1014–1021, 2012.
- [74] T. Baasch and J. Dual, “Acoustofluidic particle dynamics: Beyond the Rayleigh limit,” *J. Acoust. Soc. Am.*, vol. 143, no. 1, pp. 509–519, 2018.
- [75] H. Bruus, “Acoustofluidics 1: Governing equations in microfluidics,” *Lab Chip*, vol. 11, no. 22, pp. 3742–3751, 2011.
- [76] H. Bruus, “Acoustofluidics 2: Perturbation theory and ultrasound resonance modes,” *Lab Chip*, vol. 12, no. 1, pp. 20–28, 2012.
- [77] J. Friend and L. Y. Yeo, “Microscale acoustofluidics: Microfluidics driven via acoustics and ultrasonics,” *Rev. Mod. Phys.*, vol. 83, no. 2, pp. 647–704, 2011.
- [78] J. Dual and T. Schwarz, “Acoustofluidics 3: Continuum mechanics for ultrasonic particle manipulation,” *Lab Chip*, vol. 12, no. 2, pp. 244–252, 2012.
- [79] M. Settnes and H. Bruus, “Forces acting on a small particle in an acoustical field in a viscous fluid,” *Phys. Rev. E - Stat. Nonlinear, Soft Matter Phys.*, vol. 85, no. 1, 2012.
- [80] Gorkov LP, “On the forces acting on a small particle in an acoustic field in

an ideal fluid,” *Dokl Akad Nauk SSSR* 6773–776, 1962.

- [81] P. Augustsson, R. Barnkob, S. T. Wereley, H. Bruus, and T. Laurell, “Automated and temperature-controlled micro-PIV measurements enabling long-term-stable microchannel acoustophoresis characterization,” *Lab Chip*, vol. 11, no. 24, pp. 4152–4164, 2011.
- [82] “Acrylic tolerances.” [Online]. Available: <https://www.cutmyplastic.co.uk>. [Accessed: 01-Dec-2020].
- [83] “Silicon Wafer Tolerance.” [Online]. Available: <https://waferpro.com/silicon-wafers/>. [Accessed: 14-Dec-2020].
- [84] “Cutting Tolerances.” [Online]. Available: <https://www.protocase.com/resources/tolerances/profile-cutting.php#tolerances>. [Accessed: 14-Dec-2020].
- [85] “Laser Cutting for Plastics.” [Online]. Available: http://www.support.induflex.dk/Plast_Laserskaering_acryl.aspx?Lang=en-GB. [Accessed: 14-Dec-2020].
- [86] “DMG NTX Turn & Mill.” [Online]. Available: <https://en.dmgmori.com/products/machines/turning/turn-mill/ntx/ntx-1000>. [Accessed: 14-Dec-2020].
- [87] “Schott Borofloat Glass Tolerances.” [Online]. Available: <https://www.uqgoptics.com/wp-content/uploads/2019/07/Schott-Borofloat-33.pdf>. [Accessed: 14-Dec-2020].
- [88] “Piezoelectric Tolerances - 1.” [Online]. Available: <https://www.ceramtec.com/standard-shapes-and-sizes/plates/>. [Accessed: 14-Dec-2020].
- [89] “Piezoelectric Tolerances - 2.” [Online]. Available: [http://www.trspiezo.com/Portals/0/Ceramic Standard Shapes and Tolerances.pdf](http://www.trspiezo.com/Portals/0/Ceramic%20Standard%20Shapes%20and%20Tolerances.pdf). [Accessed: 14-Dec-2020].

- [90] “DISCO Dicing Saw DAD3230.” [Online]. Available: <https://www.disco.co.jp/eg/products/dicer/dad3230.html>.
- [91] S. Franssila, *Introduction to Microfabrication*, Second Edi. Wiley, 2013.
- [92] W. N. Bodé, L. Jiang, T. Laurell, and H. Bruus, “Microparticle acoustophoresis in aluminum-based acoustofluidic devices with PDMS covers,” *Micromachines*, vol. 11, no. 3, pp. 1–15, 2020.
- [93] M. Antfolk, P. B. Muller, P. Augustsson, H. Bruus, and T. Laurell, “Focusing of sub-micrometer particles and bacteria enabled by two-dimensional acoustophoresis,” *Lab Chip*, vol. 14, no. 15, pp. 2791–2799, 2014.